Isotopically selective detection of rubidium in krypton

ISOTOPICALLY SELECTIVE DETECTION OF RUBIDIUM IN KRYPTON

PROEFSCHRIFT

ter verkrijging van de graad van doctor aan de Technische Universiteit Eindhoven, op gezag van de Rector Magnificus, prof. dr. J.H. van Lint, voor een commissie aangewezen door het College van Dekanen in het openbaar te verdedigen op dinsdag 8 december 1992 om 16.00 uur

door

ALEXANDER MICHAEL VAN DER SPEK

geboren te Apeldoorn

Dit proefschrift is goedgekeurd door
de promotoren
prof. dr. ir. H.L. Hagedoorn
en
prof. dr. F.J. de Hoog

WIE ZICH WAAGT IN HET ONBEKENDE MOET ER VREDE MEE HEBBEN, DAT HIJ REIST ZONDER GEZELLEN.

André Gide (1869 - 1951)

SCOPE OF THIS STUDY

This thesis deals with three different but strongly interrelated subjects. The subjects were chosen to help solve some of the questions related to the very expensive production process of radio-isotopes for medical imaging. The production of ^{81}Rb in high pressure krypton gastargets in particular has been a driving force behind this work.

A double resonance method was developed to selectively detect separate rubidium isotopes with high sensitivity in high pressure krypton gas. This double resonance technique circumvents the problem of pressure broadening by combining the high resolving power of microwave spectroscopy with the sensitivity offered by laser induced fluorescence.

The double resonance method, however, is complicated enough to warrant research into a simple, self-calibrating way of measuring absolute values of the density of a particular rubidium isotope. Absolute density measurements can then be used to check the double resonance results.

In order to easily simulate the production process of rubidium isotopes in a krypton gastarget, a rubidium source is called for that is both stable under atmospheric conditions and capable of producing rubidium densities on the order of 10^{13} m^{-3} in a reproducible way. Such a source was based upon a gold-rubidium compound.

TABLE OF CONTENTS

ISOTOPICALLY SELECTIVE DETECTION OF RUBIDIUM IN KRYPTON

1.0. Abstract

Gas targets filled with extremely valuable enriched gases have become the only way to produce some of the short lived radio-isotopes used in medical imaging. The production process in such a gas target is poorly understood due to a lack of experimental data. The available knowledge is used to calculate the production rate of several rubidium isotopes in a gas target filled with ordinary krypton. Although the resulting atom densities are small, it is argued that detection of the isotopes separately is possible by applying a modified laser induced fluorescence technique. Basically the laser is used to excite a strong optical transition common to all rubidium isotopes, whereas a microwave transition of the hyperfine splitted ground states is used to identify the particular isotope. Saturating the strong optical transition serves to maximize the sensitivity. At the same time it will create a non-thermal distribution of rubidium atoms over their ground states. This imbalance can be partially restored by precisely tuned and hence characteristic microwave radiation. In this way the otherwise perturbing effects of pressure broadening are overcome. This introductory chapter concludes with an overview of this thesis.

1.1. Context of this work

New ways of detecting atoms have always helped to bring down the limit of detection. Over ten years ago the record in sensitivity was set where it still stands today: The minimum number of detectable atoms is one [1]. The laser has proven to be a most important tool in attaining this limit and even today only a few other techniques come close. The ultimate in sensitivity, however, is bought at the expense of a loss in resolution. Two techniques pioneered in the late 1970's are unable to selectively detect isotopes at the one atom level. *Resonance Ionization Spectroscopy* (RIS) derives its single atom sensitivity from the charge multiplication in a proportional counter following the selective ionisation of a single atom by a pulsed laser [2][3]. Both the use of a pulsed, hence relatively broad, laser and the use of a gas filled counter are prohibitive for attaining high resolving powers. *Saturated Optical Non Resonant Emission Spectroscopy* (SONRES) suffers the same drawback [4][5]. High background pressures are essential in order to ensure a long interaction time between laser beam and atoms to be detected. Unfortunately the resulting pressure broadening, being homogeneous, cannot be suppressed by velocity selective sub-Doppler spectroscopy. In ordinary analytic chemistry, these drawbacks are totally unimportant. Since isotopes show the same chemical behaviour the ability to discriminate between isotopes of one element is not needed. However in radiochemistry and in radiopharmacology the ability to discriminate between isotopes of specific elements is essential. Multichannel gamma-spectrometers offer enough resolving power to discriminate between most isotopes, their ultimate sensitivity is, however, always less than the sensitivity obtainable in optical

detection. Nevertheless gamma-spectrometers are the instruments of choice when it comes to calibration of activities. It is only at the production level that the lack of sensitivity of gamma-spectrometers becomes manifest. Production rates of most radio-nuclides are too small to allow for on line detection with gamma-spectrometers. Current practice favours the use of radio-isotopes with short half lives implying that for a given specific activity only a small number of particles is needed. Unfortunately it is also at the production level where the greatest potential rewards are to be gained. Production of modern radionuclides (e.g. ^{81m}Kr, ^{123}I) calls for gas targets loaded with extremely valuable enriched gases in order to ensure a low radionuclidic impurity level. For example, in $^{81}Rb/^{81m}Kr$ generators as produced with the Eindhoven AVF cyclotron. the radionuclidic purity is specified to be better than 1 ppm [6]. This low impurity level can only be maintained by using target gases enriched in ^{82}Kr. Although not all of the details of the production of ^{81}Rb via the (p,2n) reaction on ^{82}Kr in a gas target are known, extensive research [7][8][9] has brought up some limitations of the current production techniques. Notably we have:

1 the scattering of protons in the high pressure target gas causes a non-negligible increase in beam width from say 10 mm (FWHM) at the entrance of the target chamber to say 30 mm, 500 mm down stream of the proton beam [7][8];

2 the non-linear production-rate dependence, probably due to a local decrease of the target-gas density, on the beam current, impairing the use of high beam currents in order to reduce the production time [7][9];

3 the energy loss of protons (5 MeV / bar.m) [10] in the high pressure target gas causing, because of a significant smaller production rate at the end of the target chamber, a yield reduction [9] at energies below the optimum energy.

Further optimization of the production has proven to be difficult, partly due to lack of experimental data. Only through simulation and experiment enough insight may be gained to justify a more or less elaborate modification of the current production set-up. But for this, the gathering of experimental data, the essential tool, a detection scheme was lacking. It is the purpose of this thesis to show that one detection scheme, a variation of the SONRES method, which we will henceforth call *Optical Microwave Double Resonance Spectroscopy* (OMDRS) has the potential to detect selectively with excellent spatial and time resolution the intermediate ^{81}Rb and other isotopes in an on-line production set-up. The remainder of this chapter is devoted to calculating the constraints posed upon the OMDRS method by the characteristics of ^{81}Rb production in a gas target.

1.2. Production of ^{81}Rb and other rubidium nuclides

For a number of reasons, optical detection of rubidium neutral atoms during irradiation is not viable. A large fraction of rubidium atoms will be ionized by

the high energy proton beam. Furthermore, the gas target is heated appreciably by the decelerating protons. Heat conduction alone is not enough to remove the total dissipated power (at 30 μA and 30 MeV, 900 W is dissipated). Thus a convective flow will be established by which the gas is cooled and which carries away the rubidium nuclides. In a stainless steel target vessel the wall acts as a very efficient rubidium 'sink'. This may be anticipated from the bond energy of rubidium ions and neutrals on tungsten; 1.9 and 2.6 eV [11][12] respectively. These energies are so high (equivalent temperatures are 22000 K and 30000 K) that thermal desorption at temperatures below, say 1000 K is negligible: Carried away by convective currents, a rubidium atom or ion will never return to the gas phase once it collides with the target wall. Switching off the beam, however, results in a very rapid pressure drop in the target [10]. The pressure, which may have risen by a factor of two during irradiation falls very steeply (within one second) to a value which is 10% higher than the original value. The conclusion that the convective currents stop equally rapid seems justified. This all the more shows the need for a reliable estimate of transport processes in the target.

1.2.1. *Estimation of the importance of transport processes*

The equation of continuity for rubidium radionuclide 'j' is in dimensionless coordinates:

$$\frac{\partial x_j}{\partial \tau} + (\underline{v} , \text{grad } x_j) = Sc^{-1} \Delta x_j - \int_{E_0}^{E} \Pi_j(e)\, de - \Lambda_j x_j - K_i x_j y_i \qquad (1)$$

where x_j is the fraction rubidium radionuclides 'j', in the gasphase relative to the krypton gas density N, $\tau = t\mu / \rho d^2$ is a dimensionless time, $\underline{v} = d\rho/\mu \, \underline{v}'$ is a dimensioless velocity, Sc is the Schmidt number ($Sc = \mu / \rho D$), $\Pi_j(e) = Y_j(e)\, i\, (\lambda_j)^{-1}\, (\mu / \rho d^2)^{-1}\, (NV)^{-1}$ is a production term, Λ_j is a dimensionless decay constant $(\mu / \rho d^2)^{-1} \lambda_j$ and K_i is a dimensionless reaction constant $(\mu / \rho\, d^2)^{-1}\, k_i\, (N/L)^2\, (T/T^o)^2\, (p^o)^2$ describing the reaction of rubidium with residual impurities.V is the production volume, T the absolute temperature, L is Loschmidt's number, $T^o = 273.15$ K. $p^o = 101325$ Pa. The remaining symbols are explained in Table 1, which also lists numerical values, units and references. Substitution of these values in Eq. 1 gives:

$$\frac{\partial x_j}{\partial \tau} + (\underline{v} , \text{grad } x_j) = 2.1\ 10^{-4} \Delta x_j + 4.2\ 10^{-11} - 9.9\ 10^{-3}\, x_j - 9.6\ 10^{2}\, x_j \qquad (2)$$

Thus it is clear that diffusion can be neglected when compared with the decay of rubidium by radiation or reaction. This is a direct consequence of the high target gas pressure used (1 bar). At lower pressures diffusion may

Table 1 Constants for determining various transport mechanisms

Name	Symbol	Value	Unit	Reference	Note
Mass density Kr	ρ	3.744	kg m^{-3}	[13]	at 1 bar
Dynamic viscosity Kr	μ	$3.96\ 10^{-5}$	$kgm^{-1}s^{-1}$	[14]	a)
Decay constant	λ	$4.2\ 10^{-5}$	s^{-1}	[7]	for ^{81}Rb
Diffusion constant	D	$1.3\ 10^{-5}$	m^2s^{-1}	[15]	^{85}Rb in 1 bar Ar
Reaction constant	k_j	0.3938	$Pa^{-2}s^{-1}$	[3]	b)
Isotope yield	Y_j	10	GBq C^{-1} MeV^{-1}	[7][9]	
Beam current	i	10	µA		for 1 hour = EOB - BOB
Energy loss	E_o-E	5	MeV	[10]	at 5 MeV bar^{-1} m^{-1}
Relative abundance	N_j/N	1			pure ^{82}Kr
Relative impurity concentration	y_i	$1\ 10^{-9}$			
Target vessel diameter	d	$5\ 10^{-2}$	m		1 m long

a) This value is estimated from critical point data for krypton as compiled by O.A. Hougen and N. Watson [16] and by K. A, Kobe and R.E. Lynn [17]

b) This value was measured for Cs in Ar with traces of O_2 present, thus for Rb in Kr it serves as an estimate only.

become the main loss process. Also it follows from Eq. 2 that convective transport, if present, comes next to chemical reactions in effectiveness of removing rubidium atoms from a chosen detection volume. It should be clear that the values in Table 1, as far as they could be chosen freely, represent a worst case approach. In practice it may, for example, be possible to reduce the impurity level below the 1 ppb of Table 1 with a corresponding reduction in loss rate.

1.2.2. Calculation of rubidium isotope densities in a target

Since the convective term in Eq. 1 and Eq. 2 is not known, the equations cannot be solved. In principle the convective term follows from the coupled problem of heat transport by the krypton gas. A different approach is proposed, however. It is assumed that the irradiation time is very short compared to the characteristic time constants of the decay processes. No convective currents will be built up by such a short pulse and the relative density distribution of rubidium following the pulse can be described by:

$$\frac{\partial x_j}{\partial \tau} - Sc^{-1} \Delta x_j + \Lambda_j x_j + K_i x_j y_i = 0 \qquad (3)$$

where dimensionless coordinates have been used, Eq. 3 is, in contrast to Eq. 1 and Eq. 2 homogeneous. The inhomogeneous term was transferred to the starting condition:

$$x_j = \Pi_j (E_o - E) \frac{1-\exp(-\Lambda_j \Delta)}{\Lambda_j}; \tau = 0, \quad x_j = 0; r = 1/2, \quad x_j = 0; z = 0 \text{ or } z = L/d \qquad (4)$$

where Δ, the dimensioless pulse width equals (EOB - BOB) μ / ρd^2. Eq. 3 can be solved easily using a procedure first suggested by Danckwerts [18]. The solution is:

$$x_j (r, z, \tau) = X_j (r, z, \tau) \exp(- (\Lambda_j + K_i y_i) \tau) \qquad (5)$$

where $X_j (r, z, \tau)$ is the solution to equation Eq. 3 but with both Λ_j and K_i set to zero. Although the Green function for this diffusion problem is known [19], and the solution can thus be written down immediately, the result is complicated and not easily amendable to the goal set for this paragraph. Therefore one last approximation is made: the diffusion term in Eq. 3 is neglected. This is allowed for high target gas pressures, but not for target gas pressures of a few hundred millibars or lower. The difficult problem in Eq. 1 from which we started has now become very simple. The solution is:

$$x_j (r, z, \tau) = \Pi_j (r, z, \tau) (E_o - E) \frac{1-\exp(-\Lambda_j \Delta)}{\Lambda_j} (\exp(- (\Lambda_j + K_i y_i) \tau) \qquad (6)$$

This solution was used in calculating Table 2, where the relative and

Table 2 Relative and absolute densities of several Rb isotopes a)

Isotope j	Yield b) GBq C^{-1} MeV^{-1}	$T_{1/2}$	$x_j(0,0,0)$	$n_j(0,0,0)$ $[m^{-3}]$	$n_j(0,0,3\ s)$ $[m^{-3}]$	fraction $n_j / \Sigma n_j$ [%]
^{79}Rb	10	22.9 m	$9.43\ 10^{-15}$	$2.53\ 10^{11}$	$1.37\ 10^{6}$	0.513
^{81}Rb	10	4.58 h	$1.13\ 10^{-13}$	$3.04\ 10^{12}$	$1.64\ 10^{7}$	6.165
^{81m}Rb	60	30.3 m	$7.49\ 10^{-14}$	$2.01\ 10^{12}$	$1.08\ 10^{7}$	4.073
^{82m}Rb	9	6.2 h	$1.38\ 10^{-13}$	$3.71\ 10^{12}$	$2.00\ 10^{7}$	7.517
^{83}Rb	0.1	86.2 d	$5.11\ 10^{-13}$	$1.37\ 10^{13}$	$7.41\ 10^{7}$	27.81
^{84}Rb	0.5	32.9 d	$9.78\ 10^{-13}$	$2.63\ 10^{13}$	$1.42\ 10^{8}$	53.28
^{84m}Rb	50	20.4 m	$4.69\ 10^{-16}$	$1.26\ 10^{10}$	$5.84\ 10^{4}$	0.021
^{86}Rb	0.01	18.7 d	$1.11\ 10^{-14}$	$2.98\ 10^{11}$	$1.61\ 10^{6}$	0.603
				---------- +	---------- +	-------- +
				$4.93\ 10^{13}$	$2.66\ 10^{8}$	100

a) The beam current is 10 µA, the irradiation time is 0.1 s and the target volume is 2 l filled with 1 bar natural Kr at 273.15 K, taking into account a 1 ppb O_2 impurity.

b) A mean value was used over an energy interval of 5 MeV.

absolute densities of several rubidium isotopes have been compiled for the parameters shown.

It is clear that the densities of rubidium isotopes produced by a 10 μA, 0.1s pulse are extremely low. Furthermore the densities decrease rapidly. After only 3s the number of atoms available for detection in a detection volume of say 10^{-9} m^3 (1 mm^3) has dropped below 1. Nevertheless neither the number densities produced nor the available time for detection impair the possibility of detection by some method utilizing laser induced fluorescence [20][21]. Also, densities lower by as much as a factor of 100 have been detected successfully [22].

1.3. Line spectra of rubidium isotopes

The ability to discriminate between rubidium isotopes rests upon the minor differences between them. These differences are small, of physical nature and of nuclear origin. Most important is the difference in nuclear spin because the nuclear spin couples with the electronic spin to produce an observable, large and characteristic hyperfine structure splitting of the electronic ground state. Hyperfine splittings of 29 isotopes of rubidium are known or may be calculated from published hyperfine constants A ($5^2S_{1/2}$) [23][24]. Some of the hyperfine splittings have been measured with a precision of 1 part in 10^9 or better [25][26][27][28][29]. The reason for the need and existence of such extreme precision is that atomic clocks based upon gas filled rubidium absorption cells surpass even the cesium beam atomic clock in short term frequency stability.

Figure 1 represents the ground state hyperfine splittings of the rubidium isotopes which may be produced by (p,xn) reactions on Kr in its natural isotopic abundance. Only one isotope (^{78}Rb) has nuclear spin zero, hence no hyperfine splitting. The remaining isotopes show a wide variation ranging from 232.8 MHz (^{80}Rb) up to 11586.5 MHz for the high spin ^{81m}Rb (I = 9/2). Also the smallest difference in hyperfine splittings can be found from Figure 1: HFS(^{83}Rb) - HFS(^{84}Rb) = 102 MHz. Every optical detection technique with the capability to discriminate between rubidium isotopes uses these large and characteristic hyperfine splittings. The method proposed in this thesis is no exception. There is, however, one serious complication. The hyperfine splitting may be masked completely by spectral line broadening. Pressure broadening is the most important among intrinsic broadening mechanisms. Since the rubidium isotopes are produced in a krypton gas target with a filling pressure of 1 bar (or more), the hyperfine splitting becomes unobservable.

Figure 2 bears this out. The photon cross section spectrum of Figure 2 was calculated using standard formulae only [30][31]. For small enough optical densities, the shape of the spectrum in Figure 2 equals an observed fluorescence or absorption spectrum for a mixture of rubidium isotopes. The relative fraction of isotopes was taken from Table 2. The line profile function,

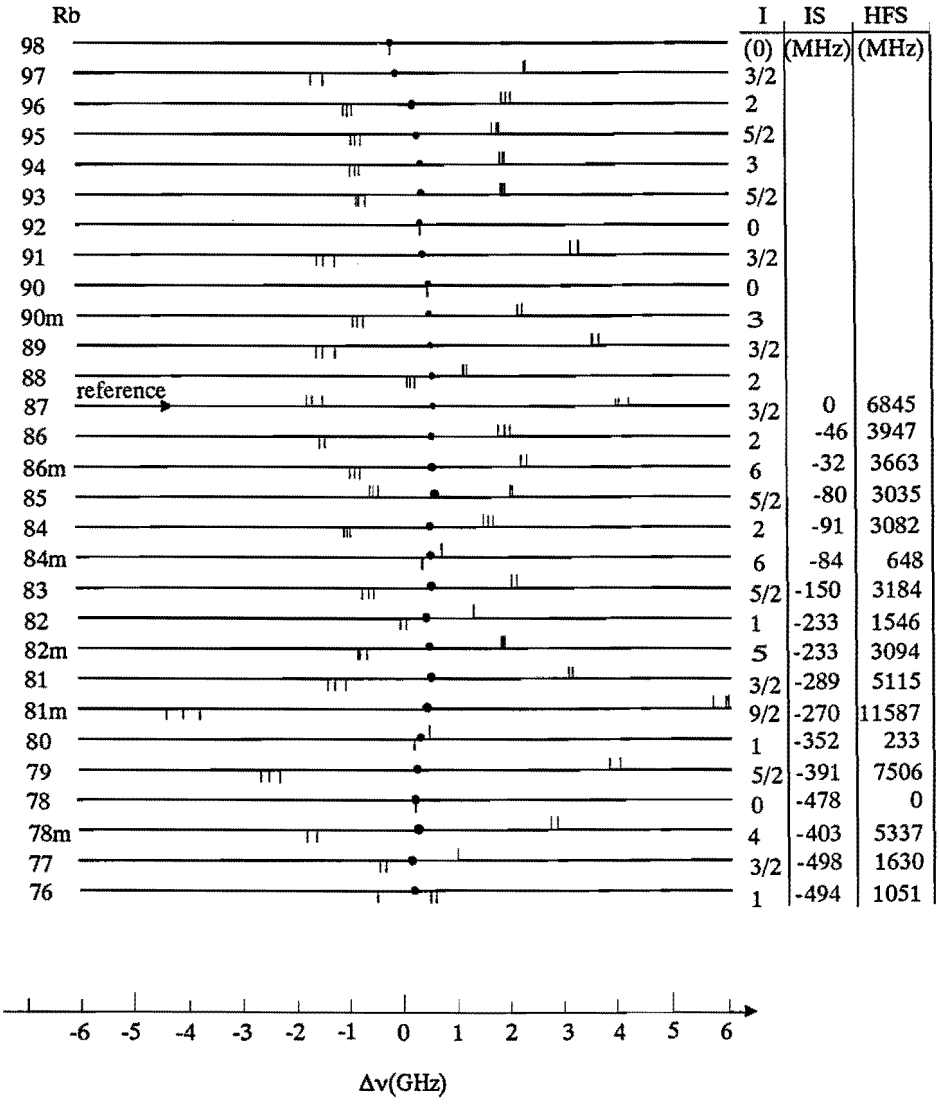

Figure 1 Hyperfine structure of rubidium isotopes.

Hyperfine components of the optical D_2 line for several rubidium isotopes (the sign indicates polarization of the particular component). The ground state hyperfine splitting, the isotope shift and the nuclear spin are given in a column to the right of each row. An entry denotes the possibility of producing this isotope by a (p,xn) reaction on naturally abundant krypton with an initial proton beam energy of 30 MeV. This figure is adapted from Thibault [23]. Wherever possible, more accurate, recent data were used to update the values in this figure.

however, was a Voigt integral (approximated by a procedure given by Gautschi [32][33] which is a convolution of the Gaussian Doppler profile and the Lorentzian pressure profile. It is clear that the pressure broadening rate (14.2 MHz/mbar [34][35]) is much too high to allow for the detection of several isotopes separately. Moreover, pressure broadening is a homogeneous broadening mechanism, thus it cannot be suppressed by velocity selective sub-Doppler spectroscopic techniques [36].

1.4. Experimental requirement; high resolving power combined with extreme sensitivity

The past two paragraphs were written to allow a further specification of constraints to be imposed upon an experiment:

a The experiment must be sensitive to 1 rubidium atom per cubic millimetre.

b The experiment must be insensitive to 10^{15} krypton atoms per cubic millimetre.

c The experiment must have a resolving power of 10^{7}.

d The resolving power must not be dependent on the krypton gas pressure.

These requirements can be met by combining the extreme sensitivity offered by *Laser Induced Fluorescence* (LIF) with the resolving power common to micro-wave spectroscopy. Both the required sensitivity (a + b) and the resolving powers called for (c + d) have been demonstrated in separate experiments. The challenge is to demonstrate the combination. In doing so the operating rubidium vapour cell frequency standards are merged with and extended to an adaptation of *Saturated Optical Non Resonant Emission Spectroscopy.*

Without going into detail it may be shown that such a combination is promising. By inspection of Table 3 it becomes clear that the optical resonance lines carry 99% of the total strength for transitions originating from the 5 $^{2}S_{1/2}$ ground level, these strong lines, however, are easily perturbed as is shown by the rate of pressure broadening. In contrast the pressure broadening of the microwave transition between the hyperfine splitted ground levels is almost negligible. A physical interpretation of the large differences obviously present can be given in terms of the wave function of the rubidium valence electron. For example the 5 $^{2}S_{1/2}$ ground level wave function is spherically symmetric and this symmetry is not easily disturbed. Moreover, since the line strength of the microwave transition between the hyperfine structure components of the ground level of rubidium does not depend on the radial part of the valence electron wave function a small pressure broadening rate might be expected. The principle of *Optical Microwave Double Resonance Spectroscopy* must now become clear. The strong resonance lines are, irrespective of their width, ideally suited to hyperfine optical

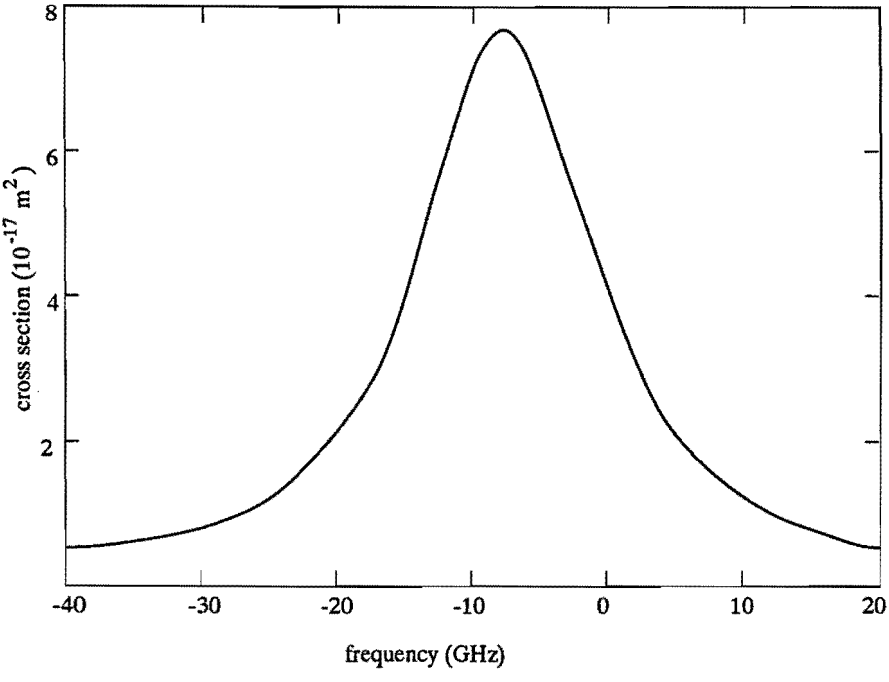

Figure 2 Calculated pressure broadened optical (D_2) line profile for a mixture of rubidium isotopes.

The isotope abundance was taken from Table 2 and corresponds to the expected abundance of isotopes in a 1 bar gas target loaded with naturally abundant krypton after irradiation with protons of 30 MeV energy for 0.1 second at 10 μA current. Separate isotope lines are masked completely by the 14.2 GHz pressure broadening.

pumping. The resulting non-thermal population difference in the hyperfine splitted ground states leads to a strongly reduced absorption for the resonance lines unless the hyperfine splitted ground states are coupled by microwave radiation tuned to the correct frequency. Thus the presence of a particular rubidium isotope is indicated by the microwave frequency where the optical absorption (or fluorescence) peaks. The amount of a particular rubidium isotope may be calculated from the peak area.

1.5. This thesis

In order to evaluate the potential of OMDRS for on-line detection of rubidium isotopes in krypton gas targets an experimental set-up has been designed, built and operated. Realistic evaluation calls for a set-up able to mimic as closely as possible the conditions inside a production set-up. Complete evaluation is not possible without a thorough understanding based upon theory and simulation. This thesis addresses both aspects intermingled with each other.

Chapter 2 describes, in detail, the experimental set-up. Modular design principles allow for easy modification of the set-up in order to continue to make realistic experiments possible. Sample results from both model calculations and experiments are included so that a complete picture may be gained.

Chapter 3 deals with low-level fluorescence detection and extremely low rubidium vapour pressures. The importance of the subject is clear in the present context.

Chapter 4 stands apart because the experimental equipment differs substantially from that covered in the other two chapters. Here Particle Induced X-ray Emission [37] is used to measure the vapour pressure of rubidium in equilibrium with an AuRb alloy. Such an alloy serves as an easy to use, calibrated source of low density vapour. Chapters 3 and 4 are complementary in experimental technique but comparable in desired results. Thus they serve to strengthen each other when the subject under investigation is interchanged.

It has become clear during the course of this project that the applicability of OMDRS is not limited to on-line detection of rubidium isotopes. For one thing, a gas target loaded with 1 bar krypton in its natural isotopic abundance is instrumental in producing rubidium isotopes off the line of nuclear stability, and the production rate is at least comparable to and in some cases much higher than the production rates offered by e.g. the ISOLDE facility at CERN [38]. Thus it may for example be possible to refine our knowledge of alkali isotopes by producing them in a rare gas target. Also, current interests in atomic physics and hyperfine interactions tend to centre around subtle, previously unobservable, line shape changes due to saturation [39], inhomogeneities [40], spin exchange [41] or wall collisions [42]. Some of these effects may be studied by the present experimental set-up while others will require a minor modification.

Table 3 Optical characteristics of rubidium

Transition	Oscillator strength	Lifetime	Doppler width	Natural width	Pressure broadening rate
	f [%]	τ [s]	$\Delta\nu_D$ [Hz]	$\Delta\nu_N$ [Hz]	$\Delta\nu/\Delta p$ [Hz/mbar]
$5^2P_{1/2} - 5^2S_{1/2}$ (D_1)	32 [43]	$28.5\ 10^{-9}$ [43]	$507\ 10^6$	$5.6\ 10^6$	$16.0\ 10^6$ a) [34]
$5^2P_{3/2} - 5^2S_{1/2}$ (D_2)	67 [43]	$26.5\ 10^{-9}$ [43]	$516\ 10^6$	$6.0\ 10^6$	$14.2\ 10^6$ a) [34]
$5^2S_{1/2}$ (F'=>F) (^{85}Rb)	-	$> 10^{10}$	$4\ 10^3$	-	0.47 b)
$5^2S_{1/2}$ (F'=>F) (^{87}Rb)	-	$> 10^{10}$	$9\ 10^3$	-	0.475 b)

a) At 320 K

b) For Rb in Ar

REFERENCES

[1] A.L. Robinson: *Science* (1978) **199**, 1191-1193.

[2] G.S. Hurst, M.H. Nayfeh and J.P. Young: *Phys.Rev. A* (1977) **15**, 2283-2292.

[3] G.S. Hurst, M.G. Payne, S.D. Kramer and J.P. Young: *Rev.Mod.Phys.* (1979) **51**, 767-819.

[4] J.A. Gelbwachs, C.F. Klein and J.E. Wessel: *Appl. Phys. Lett.* (1977) **30**, 489-491.

[5] J.A. Gelbwachs, C.F. Klein and J.E. Wessel: *IEEE J. Q.E.* (1978) **14**, 121-125.

[6] "Product guide," CYGNE B.V., Eindhoven, The Netherlands.

[7] J.J.L. Mulders: "An experimental investigation of proton-induced phenomena in krypton," *Ph.D. Thesis*, Eindhoven University of Technology, Eindhoven, The Netherlands (1985).

[8] J.J.L. Mulders and L.W.G. Steenhuysen: *Int.J.Appl.Radiot.Isot.* (1985) **36**, 833-841.

[9] J.J.L. Mulders: *Int.J.Appl.Radiot.Isot.* (1984) **35**, 475-480.

[10] A.G.M. Janssen: CYGNE B.V. and Eindhoven University of Technology, Eindhoven, The Netherlands Private Communication.

[11] F.L. Hughes and H. Lewinstein: *Phys. Rev.* (1959) **113**, 1029-1035.

[12] F.L. Hughes: *Phys. Rev.* (1959) **113**, 1036-1038.

[13] H.D. Baehr *et al.*: *Praktische Physik (Kohlrausch)*, Teubner, Stuttgart (1986).

[14] R.B. Bird, W.E. Stewart and E.N. Lightfoot: *Transport phenomena*, John Wiley, New York (1960).

[15] J. Vanier, J.F. Simard and J.S. Boulanger: *Phys. Rev. A* (1974) **9**, 1031-1040.

[16] O.A. Hougen and N. Watson: *Chemical Process Principles III*, John Wiley, New York (1947) 843.

[17] K.A. Kobe and R.E. Lynn: *Chem. Rev.* (1952) **52**, 117-236.

[18] P.V. Danckwerts: *Trans. Faraday Soc.* (1951) **47**, 1014-1023.

[19] H.S. Carslaw and J.C. Jaeger: *Conduction of heat in solids*, Clarendon Press, Oxford (1986).

[20] F.C.M. Coolen and H.L. Hagedoorn: *J. Opt. Soc. Am.* (1975) **65**, 952.

[21] F.C.M. Coolen: "Fluorescence studies on 20Na an excited neon

atoms in proton-induced plasmas," *Ph.D. Thesis*, Eindhoven University of Technology, Eindhoven (1976).

[22] W.M. Fairbank, T.W. Haensch and A.L. Schawlow: *J. Opt. Soc. Am.* (1975) **65**, 199.

[23] C. Thibault *et al.*: *Phys. Rev. C* (1981) **23**, 2720-2729.

[24] H.T. Duong *et al.*: *J. Physique* (1986) **47**, 1903-1908.

[25] G.H. Fuller: *J. Phys. Chem. Ref. Data* (1976) **5**, 835-1092.

[26] L.Essen, R.G. Hope and D. Sutcliffe: *Nature* (1961) **189**, 298.

[27] S. Penselin, T. Moran and V.W. Cohen: *Phys. Rev* (1962) **127**, 524-528.

[28] P.L. Bender, E.C. Beaty and A.R. Chi: *Phys. Rev. Lett.* (1958) **1**, 311-313.

[29] E. Arimondo, M. Inguscia and P. Violino: *Rev. Mod. Phys.* (1977) **47**, 31-71.

[30] A.M. van der Spek, J.J.L. Mulders and L.W.G. Steenhuysen: *J. Opt. Soc. Am.* (1988) **35**, 1478-1483.

[31] A.C.G. Mitchell and M.W. Zemansky: *Resonance radiation and excited atoms*, Cambridge UP, Cambridge (1971).

[32] W. Gautschi: *Comm. ACM* (1969) **12**, 635.

[33] W. Gautschi: *SIAM J. Numer. Anal* (1979) **7**, 187-198.

[34] Ch. Ottinger, R. Scheps, G.W. York and A. Gallagher: *Phys. Rev. A* (1975) **11**, 1815-1828.

[35] N.J. Kaliteevski, M. Risko and M.P. Chaika: *Opt. Spectr.* (1976) **41**, 293.

[36] W. Demtroeder: *Laser Spectroscopy*, Springer Verlag, Berlin (1981).

[37] S.A.E. Johansson and T.B. Johansson: *Nucl. Instr. Meth.* (1976) **137**, 473-516.

[38] H.L. Ravn, S. Sundell and L. Westgaard: *Nucl. Instr. Meth.* (1975) **123**, 131-144.

[39] R. Walkup, A. Spielfiedel, W.D. Phillips and D.E. Pritchard: *Phys. Rev. A* (1981) **23**, 1869-1873.

[40] J.C. Camparo: *Phys. Rev. A* (1989) **39**, 69-77.

[41] R.J. Knize: *Phys. Rev. A* (1989) **40**, 6219-6222.

[42] M. Tanaka *et al.*: *Phys. Rev. A* (1990) **41**, 1496-1504.

[43] A.A. Radzig and B.M. Smirnov: *Reference data on atoms, molecules and ions*, Springer Verlag, Berlin (1985).

DETECTION OF RUBIDIUM ISOTOPES BY OPTICAL MICROWAVE DOUBLE RESONANCE SPECTROSCOPY

2.0. Abstract

A method is described for the selective detection of rubidium isotopes in high pressure buffer gases. The method is a combination of laser induced fluorescence to obtain high sensitivity and microwave spectroscopy to obtain high resolving powers. An experimental apparatus was developed and calibrated in order to demonstrate the feasibility of the method. Calibration results include measurements of all the critical parts of the experiment. Results indicate that small amounts of rubidium isotopes in krypton can be detected upto pressures of about 20 mbar. At higher pressures, experimental verification of the feasibility of the method could not be obtained. This was shown to be due to total loss of rubidium atoms by chemical reaction with residual impurities in the krypton gas.

2.1. Introduction

Single atom sensitivity is the ultimate goal of all apparatus oriented research in analytical chemistry. In all but a few exceptions high sensitivity is bought at the expense of a, sometimes considerable, loss in resolution. The challenge, thus, is to push down the limits of sensitivity while at the same time resolution must be retained. In laser-spectroscopy a vast amount of literature is concerned with either the extreme sensitivities attainable or the high resolution offered by the laser's small bandwith [1][2][3]. The combination of extreme sensitivity and high resolution is rare and not easily adapted to the more common analytical techniques. A review of trace analysis techniques is offered by Winefordner et.al. [4]. This work concerns the detection of single (rubidium) isotopes in high pressure rare-gas buffers.

Single atom detection, first demonstrated in 1978 [5] opened up a new field of research [6]. Basically the two conceptually different techniques [7][8] have both relied upon saturation of a strong optical transition which could be resonantly excited by a (pulsed) laser. Further detection of selectively excited atoms differed: In Saturated Optical Non Resonant Emission Spectroscopy (SONRES) [7] fluorescence photons from a collisionally coupled level are detected thus enabling a very good discrimination against scattered laser photons. In Resonance Ionisation Spectroscopy (RIS) [8], a second laser beam ionized the selectivily excited atoms and detection was completed by counting the photo-electrons in a proportional counter. Whereas SONRES has been applied to a common analytical technique like flame spectroscopy, in RIS the material to be analysed has to be brought into a proportional counter.

We have constructed a double-resonance apparatus enabling the selective detection of single (rubidium) isotopes. Isotope selectivity is accomplished by combining the high resolving powers offered by microwave

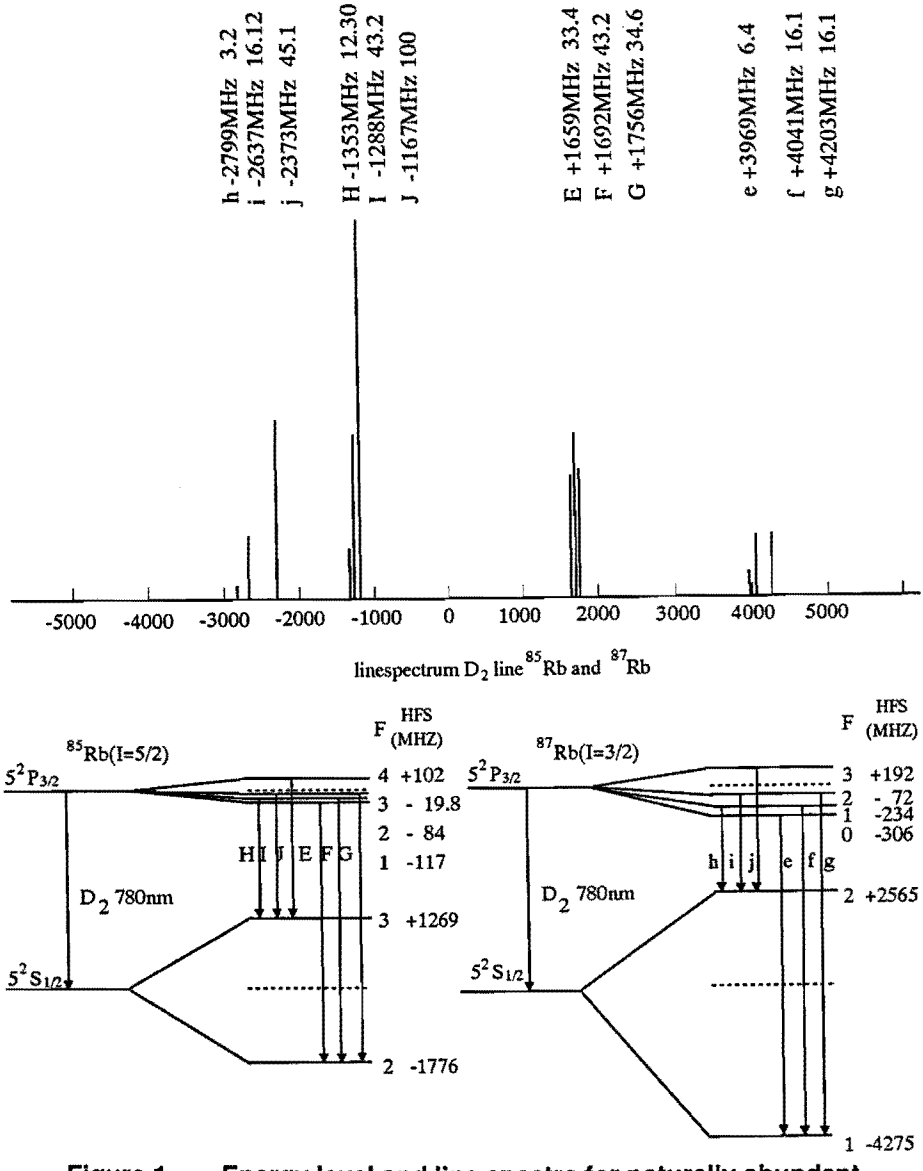

Figure 1 Energy level and line spectra for naturally abundant rubidium

Energy levels and line spectra for naturally abundant rubidium. Data were taken mainly from the review by Arimondo, Inguscia and Violino [9]. Recently much more accurate data of Barwood, Gill and Rowley [10] became available through the use of highly stabilized diode lasers.

spectroscopy with the extreme sensitivity offered by Laser Induced Fluorescence. Several applications of isotope selective one atom detection are in e.g. radioactive dating (Sr/Rb) [11], gas target studies for isotope production [12] and more fundamentally the study of nuclei off line of stability by hyperfine spectroscopy [13].

The double-resonance experiment to be considered in this paper is concerned with the detection of (non-)resonant fluorescence photons as a function of microwave frequency tuned to the hyperfine ground state splitting.

The level schemes of the two naturally abundant rubidium isotopes are shown in Figure 1. The large hyperfine ground state splitting is characteristic for a specific isotope. At low pressures the splitting is clearly resolved and the pressure of a specific isotope is signalled by the recording of two peaks separated by the isotopes ground state hyperfine splitting. At high pressures however, the hyperfine splitting is completely masked by pressure broadening. The key idea is that notwithstanding the large homogenous broadening caused by the buffer gas, hyperfine optical pumping will still occur if the laser power is high enough. A significant polarisation of the atomic ensemble can thus be obtained provided that relaxation is absent. The relaxation rate can be increased by several orders of magnitude by using microwave radiation tuned to the hyperfine ground state splitting. This transition, being of a magnetic dipole type is hardly affected by the buffer gas. Thus, whith the laser tuned to the D_2 line. optical pumping decreases the fluorescence rate from the resonant (D_2) and non-resonant (D_1) collisionally coupled levels, microwave induced relaxation increases the fluorescence rate. This chapter presents both the double-resonance apparatus and the experiments carried out. Besides demonstrating one atom sensitivity some attention has been paid to the observed line profiles and to the inelastic fine structure changing collisional process:

$$Rb^*(5^2P_{3/2}) + X = Rb^*(5^2P_{1/2}) + X \qquad (1)$$

where X is a rare gas perturber. Rate equations are used exclusively in the analysis of the experiments, since they are easy to use and more than adequate for our purpose. In the analysis we rely heavily on a body of literature needed to calculate the coefficients in the rate equations [14].

Summarizing: in this chapter we decribe the design, operation and calibration of a double resonance apparatus for isotope selective detection. In section 2.2 the experimental signals are detailed and estimated. This enabled the specification of a set of design goals, which have influenced the apparatus design. In section 2.3 the experimental set-up is described in considerable detail. This description is linked with the calibration to be described in section 2.4. Calibration is essential and serves as an indication that the set of design goals have been met. Section 2.5 gives some results of several experiments together with their interpretation, here the treatment is descriptive and less detailed. Concluding remarks are offered in section 2.6. This chapter is aimed

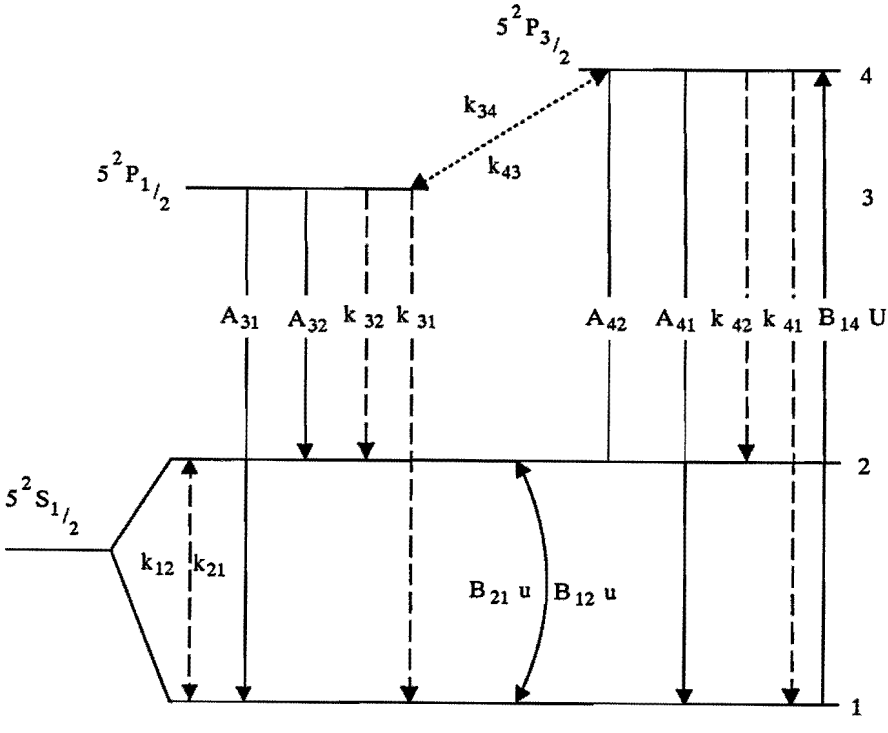

Figure 2 Four level energy scheme illustrating optical microwave double resonance spectroscopy

Simplified, four level, energy scheme of rubidium illustrating optical microwave double resonance spectroscopy. Various decay channels are denoted either by their Einstein coefficients A_{ij} or by their collision rates k_{ij}. The driven transitions are indicated by their Einstein coefficients B_{ij} multiplied by the radiation density U for laser excitation or u for microwave excitation.

at giving as complete an overview of the experiment as possible.

2.2. Signal estimation and design requirements

The double-resonance apparatus to be described in this paper had to be designed very carefully. A modular design philosophy was adhered to in order to facilitate improvements and overhauls. Attention has to be paid to five different parts: the vacuum system, the microwave equipment, the optical detection system, the optical pumping laser and last but not least: data acquisition. The importance of these parts will soon become clear. For the moment let us assume that we have a mixture of (rubidium) alkali atoms and a rare gas buffer enclosed in a cell. The mixture is irradiated by a near-infrared laser beam and by microwave radiation. The experiment can be schematically depicted as is done in Figure 2. Hyperfine optical pumping from the lower ground level transfers atoms to the upper "transparent" level. Intermediate in this process are the collisionally coupled excited $^2P_{1/2}$ and $^2P_{3/2}$ states. We may obtain a measure of the number of alkali atoms present by measuring the fluorescence from these shortlived states. Fluorescence, however will only occur if the ground state polarisation is reduced by resonantly tuned microwaves. The major experimental problems are directly connected with the expressions for the fluorescence count rates from the shortlived $^2P_{1/2}$ and $^2P_{3/2}$ states

respectively I and D, with:

$$D = \eta_D \, i \, \sigma \, n \, \frac{1-P}{2} V \qquad (2)$$

$$I = \eta_I \, i \, \sigma \, n \, \frac{1-P}{2} V \, NQv\tau \qquad (3)$$

Here the detection efficiency η differs for the direct fluorescence D and the collisionally induced fluorescence I.

The remaining symbols are explained in Table 1 where some representative numbers have been collected as well. Through the (1-P)/2 factor hyperfine optical pumping is accounted for. This of course, depends upon the laser beam intensity, the relaxation rate of the hyperfine ground state non-thermal population distribution and the microwave frequency and field strength. For our purpose here it suffices that this factor is between 0 and 1 and very small values i.e. smaller than, say 0.01 are unlikely to occur. Eq. 2 and Eq. 3 clearly show the origin of the experimental problems to be expected: Both the lifetime τ and the collision cross section Q are very small; τ = 25 ns Q = 1 barn. Thus, obtaining a measurable indirect fluorescence count rate requires an effort towards maximizing the detection volume and the detection efficiency η. The buffer gas density N

Table 1 Characteristics of double resonance experiment

Quantity	Symbol	Formula	Unit	Value	Remarks
Photon detection efficiency	η	$= \varepsilon \frac{\Omega}{4\pi} T$		$2\ 10^{-4}$	
PMT quantum efficiency	ε			0.01	S20 cathode
Solid angle efficiency	$\frac{\Omega}{4\pi}$	$= \frac{1}{16} \frac{1}{(f/\#)^2} \left[\frac{M}{M+1}\right]^2$		$4\ 10^{-2}$	
Optic's stop number	f/#			0.5	
Optic's linear magnification	M			0.5	
Transmission	T			0.5	
Photon flux	i	$= I \frac{\lambda}{hc}$	$m^{-2}s^{-1}$	$4\ 10^{20}$	
Beam intensity	I		$\mu W\ mm^{-2}$	100	
Rubidium atom density	n		m^{-3}	$1\ 10^{16}$	At 300 K
Krypton atom density	N		m^{-3}	$2.68\ 10^{25}$	At 1 bar
Detection volume	V		m^3	$1\ 10^{-7}$	
Photon cross section	σ		m^2	$1\ 10^{-15}$	D_2 line
Collision cross section	Q		m^2	$1\ 10^{-23}$	Rb - Kr
Rayleigh cross section	σ_R		m^2	$1\ 10^{-33}$	
Excited state lifetime	τ		ns	25	
Realtive velocity	v_r	$= \sqrt{v_{Rb}^2 + v_{Kr}^2}$	$m\ s^{-1}$	386	
Ground state polarization	P	$= \frac{n_2 - n_1}{n_2 + n_1}$		0.8	

is limited in practice since at pressures larger than a few bar complexities not accounted for in Eq. 2 and Eq. 3 are no longer negligible. Furthermore efficient suppression of direct fluorescence and other sources of background radiation is obligatory. In principle direct fluorescence may be used to evaluate the alkali number density n. At high buffer gas pressures, however, direct fluorescence becomes unseparable from Rayleigh scattered photons and stray light. Thus at low pressures (< 100 mbar) only, may direct fluorescence be used, provided the (linear) polarization of the laser beam is aligned with the optical detection axis. In the latter case most Rayleigh scattered photons will not be received by the optical detection system and a corresponding reduction of background is feasible. We derive a figure of merit by tentatively requiring an indirect fluorescence count rate of 1 kcps. The product of densities times photon detection efficiency $\eta_{||}nN$ must measure:

$$\eta_{||}\, n\, N > 10^{34}\ m^{-6} \qquad (4)$$

for the set of parameters as given in Table 1. In a conventional apparatus with a detection efficiency of 10^{-4} and a buffer gas density of $10^{25}\ m^{-3}$ this means an alkali atom density in excess of $10^{13}\ m^{-3}$. Thus 10^{6} atoms in a detection volume of $10^{-7}\ m^{-3}$ should be detectable easily. This estimate explicitly excludes the case of saturation. Although under saturation much larger countrates may be realized.The inclusion of saturation is postponed until paragraph 2.5 where a rate equation analysis is presented. The figure of merit of Eq. 4 is thus to be regarded as a worst case number. This worst case approach has been concomitant in the design calculations for obvious reasons. If we require the same minimum 1 kcps countrate for the direct fluorescence, it is seen that the minimum alkali atom density must be $10^{10}\ m^{-3}$ corresponding to 10^{3} atoms in the detection volume. Here, too saturation is not accounted for. We stress the importance of this point since these simple calculations already show that although very low densities of alkali atoms are easily detected, one atom sensitivity is well out of reach.

2.3. Experimental set-up

2.3.1. Overview

The heart of the apparatus Figure 3 is a glass (DURAN 8330) discharge tube axially aligned with a short piece of double-tapered microwave air line. The rubidium source is a small evacuated ampoule containing pure metallic rubidium (Merck 12314). The ampoule is broken under vacuum by heating it with Kanthal wire. The rubidium vapour pressure in the discharge tube may then be controlled by heating the broken ampoule to the desired temperature. At room temperature the rubidium atom density $n = 10^{16}\ m^{-3}$. The discharge tube is disassembled by pulling it out of the anode end. Two viton 'O'-rings insulate the discharge, when present, from a

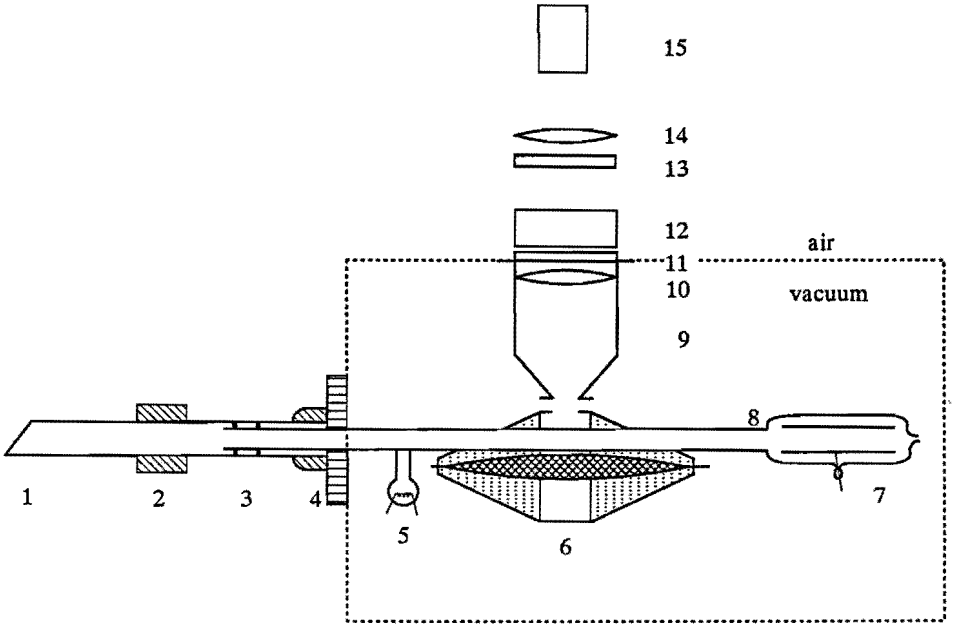

Figure 3 Experimental set-up

Overview of the experimental set-up. This drawing is not to scale. The numbers denote the components as follows; 1: Brewster window, 2: Fernico anode, 3: Viton 'discharge seal', 4: 35 mm copper gasketed vacuum flange, 5: rubidium source and Kanthal wire, 6: tapered air-line, 7: Oxidized tantalum kathode, 8: discharge tube (Duran 8330, 6 mm o.d.), 9: stray light shield, 10: positive lens (f = 100 mm), 11: transparant vacuum seal, 12: interference filter, 13: cut-off or neutral density filter, 14: positive lens (f = 50 mm), 15: S20 photomultiplier (ITT FW 1130).

stainless steel vacuum vessel.

The anode end is connected to a large (250 mm) Conflat, instrument feedthrough carrying flange by a standard 35 mm flange. In particular, the large flange is equipped with an UHV gas inlet valve connected to a krypton pressure cylinder. The discharge tube is filled through the open, cathode end when the vacuum vessel is brought to the required operating pressure. Either a continuous or a pulsating discharge may be drawn between the Fernico anode and the oxidized tantalum cathode. Low pressure discharges in krypton operate at some 250 V at currents between 5 and 100 mA. These discharges may be used to simulate a decaying proton induced plasma in krypton [15]. The doubly-tapered air-line was machined from gold-plated oxygen free copper. The inner conductor is supported by two cone shaped PTFE pieces. SMA type (Suhner) coaxial conductors and semi-rigid (Microcoax UT 141A) coaxial cable are used to transport microwave power from the vacuum feed through to the taper and back to an atmospheric 50 Ω (matched) load resistor. The frequency response of the taper and connections was kept as flat as possible, and the impedance of the device was matched to the microwave oscillator and auxiliary equipment. This ensures a multi-isotope detection capability or even a multi-element detection capability of the microwave part of this double resonance apparatus [16]. Since no spatial resolution is required from the optical detection system, a simple photometric design suffices. The design does, however, favour a large scattering volume over a large acceptance solid angle for two reasons: Narrow band interference filters require small acceptance angles and secondly it may be shown that fluorescence countrates vary inversely proportional to the acceptance angle [17]. The interference filters used for wavelength selection and background suppression are housed in a filter assembly similar to the design used by Manders et. al. [18].

2.3.2. *Diode laser and auxiliary equipment*

The linearly polarized laser beam from a single mode diode laser (SHARP LT022 MC) enters the discharge tube through the Brewster window at the anode end. The diode laser,see Figure 4, is mounted in a separate evacuated housing. Both the laser's injection current and the laser's operating temperature are stabilized and under computer control. Much of the practice of operating diode lasers for atomic physics was reviewed recently by Wieman and Hollberg [19], here we shall briefly describe our system. The wavelength of the diode laser is tuned in resonance with the desired transition and may be locked to this transition by direct modulation of the injection current [20]. Both the residual bandwidth (approximately 150 MHz/mW under free running conditions) and the induced offset from exact resonance (< 5 MHz) are negligible compared to the Doppler width (500 MHz) or the rubidium D_2 line components.

Frequency and wavelength monitoring of the diode laser is done by a combination of a high resolution travelling Michelson interferometer [21]

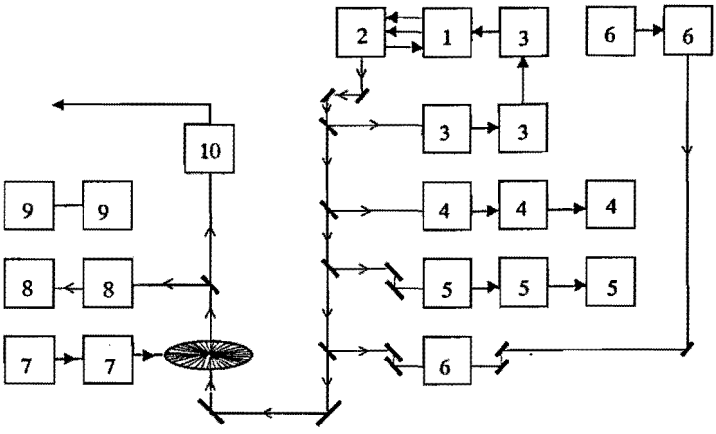

Figure 4 Diode laser and auxiliary equipment

Diode laser and auxiliary equipment are numbered as follows; 1: Diode laser control electronics, 2: Diode laser in evacuated housing, 3: rubidium reference cell, photometric amplifier and frequency lock loop, 4: short etalon (FSR = 3 GHz), photometric amplifier and true RMS meter, 5: long etalon (FSR = 150 MHz) photometric amplifier and voltmeter, 6: wave meter and reference laser, 7: rotatable beam splitter and its stepper motor drive, 8: power monitor, 9: power meter or scanning slit, 10: shutter.

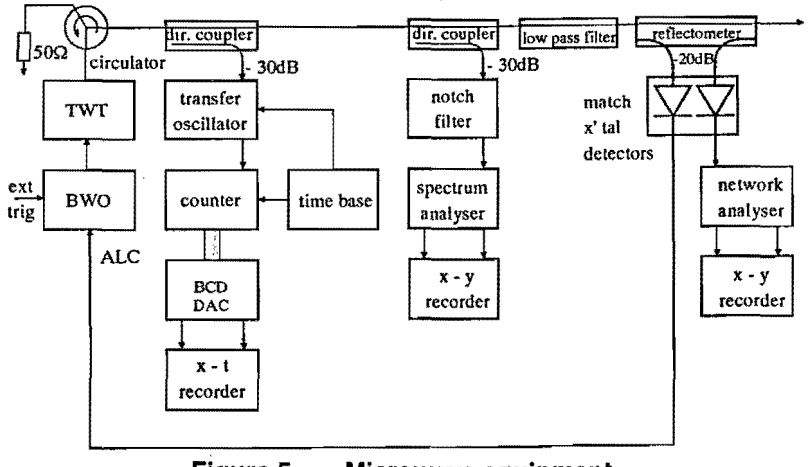

Figure 5 Microwave equipment

The master oscillator is either a Backward Wave Oscillator (BWO) or a sythesized, YIG tuned, solid state oscillator under IEEE bus control. The Travelling Wave Tube (TWT) served as a power amplifier. In some experiments the TWT was moved closer to the experiment in order to compensate for cable losses.

("wavemeter") and two etalons. The short etalon (Free Spectral Range FSR = 2.5 GHz) was designed for bandwidth compression by using it as an external cavity [22]. The type of experiments to be described in this article do not make use of this option since at 3 mW the free running bandwidth is already sufficiently small. Thus the short etalon is used for monitoring purposes only. The long etalon (FSR = 150 MHz) is used as a relative frequency scale only. Intensity of the laser beam is controlled by a stepper motor actuated rotatable beam splitter with variable transmission. Beam powers are measured with a large area photodiode (BPW34) interfaced through a 1k potentio meter, an instrumentation pre-amplifier and a programmable gain amplifier (BurrBrown PGA 100) to a 12 bit ADC. Input offset currents of the instrumentation amplifier (Burr Brown INA 101) are nullified with the potentio meter. The photodiode is calibrated against a commercially available powermeter (Newport NRC 835). Alternatively the stepper motor driven translation stage which houses the beam power meter may be equipped with a scanning slit laser beam profiler [23]. Integration of beam power over time is occasionally necessary and is most easily performed by digitizing (ORTEC 439) the photo-current of a photodiode (BPW34) which is illuminated by a part of the laser beam splitted off from the mainbeam.The resulting pulse train can then be counted using a scaler. Finally the laser beam is turned on and off with a mechanical beam shutter actuated by a small turntable motor (Lenco) which serves as an electronically operated spring.

2.3.3. *Microwave equipment*

The microwave (master) oscillator consists of a BWO tube (HP 8690 sweep oscillator +HP 8692A RF plug in) in series with a TWT amplifier (HP 491C) for the 2-4GHz band. Output power (1 W maximum) of the BWO-TWT combination may be leveled by direct control of the BWO grid using the internal ALC option. Over the small sweep widths (< 10 MHz) in use this leveling is, however, seldom necessary. Frequency monitoring of the RF output is accomplished with a down converter-counter combination (HP 2590 A tranfer oscillator, HP 5245L counter, HP 5253B plug-in) giving 1 Hz resolution with the counter's gate time set to 10 s. The spectrum- and network-analyzers present in Figure 5 (Hp 8551B + 852A and HP 1416A + 140A respectively) are used for checking and calibration only.

2.3.4. *Detection optics*

When resolution is determined by a narrow band laser, interference filters may provide both ample background suppression and large optical detection efficiencies. All filters used in this experiment were obtained from Schott. The filters are mounted in a filter assembly which has been described in detail by Manders et al. [18].

Some improvements are noteworthy e.g. the micro-switches used for indexing and identification have been dropped in favour of contactless reflective object sensors. Also a new type of fabric was used with a higher

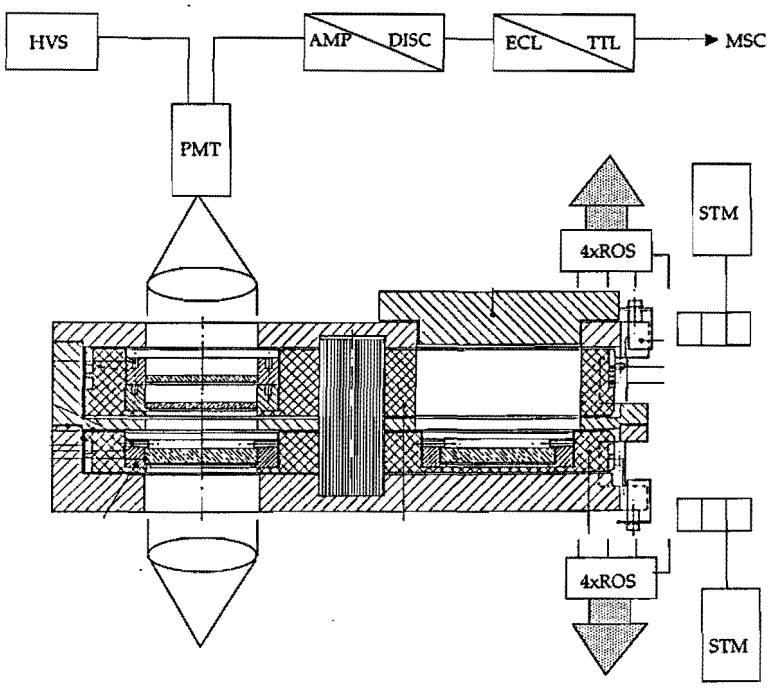

Figure 6 Detection optics

The filter assembly is adapted from Manders et. al. [18], with minor improvements by Boom and the present authors. The filter wheels are driven by STepper Motors (STM), while the position of the filter wheel is sensed by Reflective Object Sensors (ROS). The PhotoMultiplier Tube (PMT) has a S20 photocathode. The High Voltage Supply (HVS) is set at -1450 V. An ECL/TTL converter is used to adapt the pulse levels from the AMPlifier/DISCriminator to standard levels.

pile and a specific orientation of the nap. This allowed us to somewhat loosen the bolts used to compress the fabric whilst maintaining optical hermeticity. All in all the constraints set upon the pull-in rate and starting torque of the stepper motor could be relaxed considerably, resulting in a much more reliable operation. A disadvantage of the present fabric is that the orientation of the nap forces a one way rotation upon the automated exchange procedure. Compared to the improvement in reliability this disadvantage was more than compensated for.Three types of filters were used extensively. Three cavity, custom made interference filters (peak transmission 0.50, 3 nm full width at half maximum (FWHM) at 780.0 nm and at 794.6 nm) allowed the separation of direct (D_2-line) fluorescence and indirect, collisionally coupled (D_1-line) fluorescence. Background suppression of visible light could be increased by adding long-pass filters (RG 780, RG 9), to the interference filters. In some cases neutral density filters had to be added to reduce the count rate to a level where deadtime corrections could be carried out safely. Fluorescence is collected by a single lens (f = 100 mm, 50 mm diameter) located at a distance of 100 mm from the scattering volume, thus the light is sent in a roughly parallel beam through the interference filters to a second lens which focuses the fluorescence light on the photocathode of a selected red-sensitive ITT FW 130 S20 photomultiplier with an exceptionally low dark countrate (1 cps) at 20 C. This tube, taken from an old Raman spectrometer, is known to suffer from excessive light generation. Therefore the anode-cathode voltage was set to the lowest value possible, just above the point where the signal- to darkcount ratio levels off. This voltage (1450 V) is just high enough to match the 50 μV input sensitivity of the amplifier-discriminator (EG & G, 1120) which converts the photomultiplier pulses into fast (30 ns) ECL pulses. Finally the ECL pulses are stretched and converted to TTL pulses which are accumulated in the time channels of a multiscaler interfaced to the measurement computer.

2.3.5. *Vacuum equipment*

The stainless steel (SS 321) vacuum vessel is pumped by a 300 l/s, LN_2 baffled diffusion pump (Balzers, DF 100) operating with Santovac 5 oil. During high-vacuum outgassing and baking a 100 l/s ion pump (Riber PI 100) is used, whereas the diffusion pump is used mainly for rapid removal of the rare gas. Inorder to restrict the background pressure to the lowest possible value Conflat seals were used throughout with a few noteable exceptions. Both the viton seals and the PTFE parts of the microwave transmission lines restrict the baking temperature to 100 °C maximum.

Baking is done by recirculating hot air from four industrial hot air guns (3 kW each) in a double walled and isolated hood [24]. Six thermocouples record the temperatures of the vaccum vessel at different sites. The computer controls the temperature of the vessel by setting the duty cycle of the air guns. A complete high-vacuum bake typically takes over 20 hours, where most of the time is required by a controlled cool down. At all times the

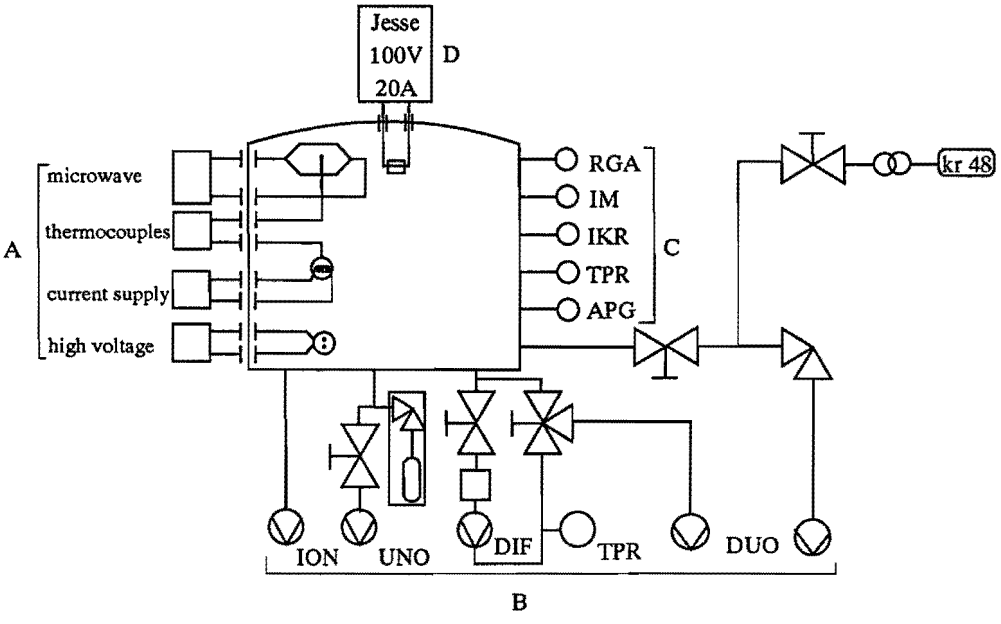

Figure 7 Vacuum equipment

Four sections are indicated: An experimental section A, a pump section B, a pressure monitoring station C an a bake-out section D. The gas filling equipment is an inlet valve, a pressure regulator and a storage bottle. The abbreviations are as follows: ION: 100 l/s getter pump, UNO: 12 m^3/h single stage roughing pump, DIF 300 l/s LN_2 baffled diffusion pump, TPR Pirani vacuum gauge, DUO: 8 m^3/h double stage roughing pump, APG absolute pressure gauge, IKR Penning vacuum gauge, IM ionisation (hot cathode) vacuum gauge, RGA residual gas analyzer.

Table 2 Typical (background) signals

Source	Signal with D_1 line filter [cps]	Signal with D_2 line filter [cps]
PM dark count a)	< 3	< 3
Fluorescent room lighting	60	60
Stray light from laser b)	25	10 000
Direct fluorescence	500	> 2 000 000 c)

a) at -20 C; -1450 V

b) 100 µW, 780 nm, non-resonant

c) 780.027 nm, high frequency hyperfine component of ^{85}Rb

temperature differences over the vessel and the temperature between hot air and vessel were kept below 5 ^{o}C. After baking for 8 hours at 100 ^{o}C the vessel reached an ultimate pressure of 1.2 10^{-8} torr as measured with a Bayard-Alpert gauge (Leybold IMG 20). Due to the restricted baking temperature the target background pressure is well out of reach. Therefore an alternative cleaning method based upon ion bombardment of the vessel wall through a gas discharge is being developed [25][26]. At the time of this writing this gas discharge cleaning is unoperative. The four high pressure xenon infrared lamps mounted in the vessel have been used as internal bake out heaters [27]. Notwithstanding the large temperature gradients introduced by the lamps, internal baking was found to be quick and easy. Their use is, however prohibited by the temperature sensitive microwave components.

2.3.6. Data acquisition.

As will be detailed later the experiment computer not only accumulates the data gathered by an array of interfaces, it also performs preliminary checks upon the consistency and reproducibility of the data. Thus one is able to evaluate the state of the experiment by inspection of a menu of key values, error conditions, status checks, moment analysis and the like. Moreover, as the experiment requires frequent microwave frequency changes, and the somewhat less frequent exchange of filters, automation is to be preferred in this respect too. The experiment computer was developed at the Department of Physics, Eindhoven University of Technology [28][29][30]. It is based upon the Motorola M68000 microprocessor and its successors. It is programmed in PEP (Program Editor and Processor), an interpreter based language closely related to SATHE. Parallel processing of seperate modules for data gathering, data reduction and output control greatly facilitate the time consuming stages of debugging and operational testing of the measurement program. The experiment computer is connected to the experiment through the modular PHYDAS interface bus [30]. This bus will accomodate a wealth of different interfaces all adhering to the PHYBUS protocol [30]. Where appropriate, specifications of scalers, preset-scalers, multi-scalers, DAC's, ADC's, stepper-motordrivers, IO-registers and the like will be given later.

2.4. Calibration of the experiment

2.4.1. Measuring routine

Our primary aim is to measure rubidium densities n. Both direct and indirect fluorescent signals D and I respectively are proportional to n as is shown by Eq. 2 and Eq. 3. Ideally, both may be used to serve our goal. In practice, however, indirect fluorescence is much weaker than direct fluorescence, but background suppression is much more efficient at this non-resonant wavelength. Clearly then, some trade-off between signal strength and background suppression will favour direct fluorescence at low buffer gas densities N, whereas at high buffer gas densities, indirect fluorescence detection becomes possible. The main sources of background for our

Table 3 Experimental combinations used for signal diagnosis and extracted signals

Filter	RF	Laser	Signal Signal = Indirect flu. + Direct flu. + Rayleigh scattering + Stray Light	Real signal
Direct fluorescence D_2 line	f	λ_k (k = 1..M)	$D^f(\lambda_k) = \eta^D{}_I n_3 A_3 + \eta^D{}_D n_4 A_4 + R + B$	$D_k{}^f = D^f(\lambda_k) - D^f(\lambda_M)$
	f_k (k = 1..M)	λ_o	$D^\lambda(f_k) = \eta^D{}_I n_3 A_3 + \eta^D{}_D n_4 A_4 + R + B$	$D_k{}^\lambda = D^\lambda(f_k) - D^\lambda(f_M)$
Indirect fluorescence D_1 line	f	λ_k (k - 1..M)	$I^f(\lambda_k) = \eta^I{}_I n_3 A_3 + \eta^I{}_D n_4 A_4 + R + B$	$I_k{}^f = I^f(\lambda_k) - I^f(\lambda_M)$
	f_k (k = 1..M)	λ_o	$I^\lambda(f_k) = \eta^I{}_I n_3 A_3 + \eta I_D n_4 A_4 + R + B$	$I_k{}^\lambda = I^\lambda(f_k) - I^\lambda(f_M)$

In this table n_3 and n_4 are the instantanous excited atom densities in the $5^2P_{1/2}$ and the $5^2P_{3/2}$ levels respectively. A_3 and A_4 are the decay rates of these levels. Fluorescence quenching is neglected.

apparatus are: light from the surroundings, stray light from the laser beam and, if indirect fluorescence is to be detected, direct fluorescence. Table 2 gives an impression of the background signal strengths.

In order to correct for the various background contributions all measurements are performed with a multiscaler. Either the diode laser wavelength or the microwave oscillator frequency are ramped synchronously with the triggering of the multi-scaler. During a laser wavelength scan the microwave frequency is offset from its very precise, resonant value. Reversely during a microwave sweep the laser wavelength is tuned to the optimum value for hyperfine pumping. The measured line profiles contain both the wanted and the unwanted information. By manipulating these profiles we can devise a background eliminating procedure. Additionally, since line profiles can be calculated rather precisely, they serve as a check upon the validity of the data. Table 3 lists all the possible combinations and the signals extracted in each case. In Table 3 provision is made for the multi-scaler time channel number k through a subscript. The superscripted variables are the microwave frequency f and the laser wavelength λ. Rayleigh scattering and straylight are treated separately for reasons to be explained shortly. A superscript D/I used in connection with the detection efficiency η (D/I) indicates an emission wavelength outside the passband of the respective interference filter. Since at all times the experimental conditions are such that complete detuning occurs well before the last time channel k = M, we obviously may correct the signals for background contributions by subtracting the contents of this channel from all other channels. In practice, a somewhat more difficult correction is applied whereby a regression line through low index channels (k = 0,1) and high index channels not only corrects for background but for power variations of the laser or backward wave oscillator as well. The Rayleigh scattering term in Table 3 may be expressed as:

$$R = \chi\eta i\sigma_R VN \tag{5}$$

where σ_R is the Rayleigh scattering cross section. The Rayleigh cross section is typically eighteen orders of magnitude smaller than the resonant photon cross-section. The factor χ takes account of the angular dependance of Rayleigh scattering with respect to the laser polarization axis. Rayleigh scattering is useful in our apparatus, since it provides a means to calibrate the density measurement. From Eq. 5, Eq. 2 and Eq. 3 the ratio of integrated (in)direct fluorescence to Rayleigh scattered photons follows as:

$$\left[\frac{\int D\,df}{R}\right]_{ideal} = \frac{\sigma}{\chi\sigma_R}\frac{n}{N}\int\left[\frac{1-P}{2}\right]df \tag{6}$$

$$\left[\frac{\int I\,df}{R}\right]_{ideal} = \frac{\sigma}{\chi\sigma_R} n\,Qv_r\tau\int\left[\frac{1-P}{2}\right]df \tag{7}$$

Table 4 Calculated quantities from experimental signals

Quantity	Symbol	Expression	Theory
Collision cross section	$Q(^2P_{1/2} - {}^2P_{3/2})$	$\frac{I}{D} = \left[\frac{I_k^f}{D_k^f}\right]_{N=N^0} - \left[\frac{I_k^f}{D_k^f}\right]_{N=0}$	$\frac{I}{D} = \frac{\eta_I}{\eta_D} N v r \tau\, Q(^2P_{1/2} - {}^2P_{3/2})$
Rubidium density	n	$\frac{\sum_k D_k^\lambda}{D^\lambda(f_M)} = \frac{\sum_k D^\lambda(f_k) - D^\lambda(f_M)}{D^\lambda(f_M)}$	$\frac{\int D\, df}{R} = \frac{\sigma}{\sigma_R}\frac{n}{N}\int\frac{1-P}{2}\, df$
Rubidium density	n	$\frac{\sum_k I_k^\lambda}{I^\lambda(f_M)} = \frac{\sum_k I_k - I^\lambda(f_M)}{I^\lambda(f_M)}$	$\frac{\int I\, df}{R} = \frac{\sigma}{\sigma_R}\frac{n}{N}\int\frac{1-P}{2}\, df$
Optical line profile	L(v)	$L_D^k = \frac{D_k^f}{N\sum_k D_k^f}$; $L_I^k = \frac{I_k^f}{N\sum_k I_k^f}$	
Microwave line profile	F(f)	$F_D^k = \frac{D_k^\lambda}{N\sum_k D_k^\lambda}$; $F_I^k = \frac{I_k^\lambda}{N\sum_k I_k^\lambda}$	

Experimentally we have:

$$\left[\frac{\int D\,df}{R}\right]_{exp.} = \frac{\sum_k D_k^{\lambda}}{D^{\lambda}(f_M) - (D^{\lambda}(f_M))_{N=0}} \qquad (8)$$

$$\left[\frac{\int I\,df}{R}\right]_{exp.} = \frac{\sum_k I_k^{\lambda}}{I^{\lambda}(f_M) - (I^{\lambda}(f_M))_{N=0}} \qquad (9)$$

where the second term in the denominator corrects for scattered straylight. By inspection of Eq. 6 and Eq. 7 it becomes clear that the rubidium density n can be given an absolute value provided that σ, σ_R, the angle factor χ and $\int(1 - P)/2\,df$, the normalized peak area can be calculated, all other factors being known, the fine-structure changing collision cross section Q in particular.

2.4.2. Filling pressure and gas purity.

The vacuum vessel is filled through an UHV gas dosing valve (Balzers UDV135). The filling pressure is measured with a factory calibrated piezo-resistive sensor (Balzers APR 010, calibrated at 395 mbar) and read from a display (Balzers APG 010). The combination of valve and sensor allows the pressure to be set to within 1 mbar of the desired value. Corresponding densities are calculated from the ideal gas law, where the temperature is room temperature read from a mercury bulb thermometer. Much more important than the pressure of the filling gas is its purity. The purity of the filling gas itself and residual impurities of the vacuum vessel determine the relaxation rate of the (hyperfine optically pumped) ground state densities of rubidium. Neglecting spin exchange, the relaxation rate is given by both theory and experiment as:

$$\gamma_i = \frac{D_i^0}{\Lambda_{11}^2}\frac{p^0}{p_i} + N^0\sigma_i v_r \frac{p_i}{p^0} \qquad (10)$$

where Λ_{11} is the fundamental mode diffusion length, p_i the pressure of gas i, σ_i the groundstate depolarization cross section, D_i^0 the diffusion constant of rubidium in gas i, p^0 is the reference pressure (p^0 = 101325 Pa), N^0 is Loschmidt's number, v_r is the mean relative velocity. Clearly at some pressure p_{Kr} the relaxation rate becomes minimal. At any other filling pressure the impurity relaxation rate must be negligible to the krypton gas contribution to the relaxation rate at this minimum.

Table 5 Impurities and ground state depolarization cross sections

Name	Formula	Cross section [m^2]	Impurity level [vpm] a)	Partial pressure [mbar] b) Calculated	Reference
Krypton	Kr	$7.3\ 10^{-25}$	n.a.	n.a.	[31]
Helium	He	$3.3\ 10^{-29}$	-	29923	[31]
Neon	Ne	$3.3\ 10^{-28}$	-	6183	[31]
Argon	Ar	$1.1\ 10^{-26}$	< 5.0	2395	[31]
Xenon	Xe	$1.3\ 10^{-23}$	< 6.0	2.8	[31]
Hydrogen	H_2	$3.0\ 10^{-28}$	< 2.0	23623	[32]
Nitrogen	N_2	$5.7\ 10^{-27}$	< 5.0	4070	[32]
Oxygen	O_2		< 0.5		
Water	H_2O		< 2.0		
Tetra Fluor Methane	CF_4		< 0.1		
Sulfur Hexa Fluoride	SF_6		< 0.1		
Carbon monoxide	CO	$1\ 10^{-26}$		2320	[33]
Carbon dioxide	CO_2				
Hydro carbons	C_xH_y		< 0.1		
Methane	CH_4	$8.0\ 10^{-28}$		23200	[32]
Ethane	C_2H_6	$3.8\ 10^{-27}$		6268	[32]
Ethene	C_2H_4	$1.3\ 10^{-26}$		1785	[32]
Cyclo-Hexane	C_6H_{12}	$4.5\ 10^{-26}$		730	[33]
Benzene	C_5H_5	$7\ 10^{-23}$		0.44	[33]
Dimethyl Ether		$3\ 10^{-22}$			[33]
Ammonia	NH_4	$8\ 10^{-22}$		0.02	[33]

a) [vpm]: parts per million by volume; impurities are taken from factory specification.

b) calculated from Eq. 11, with p_{Kr} set to 45 mbar.

$$\frac{p_i}{p_{Kr}} << \frac{\sigma_{Kr}}{\sigma_i}\frac{(v_r)_{Kr}}{(v_r)_i} \qquad (11)$$

A summary of known depolarization cross sections for some of the more common impurities has been compiled in Table 5.

With the notable exception of water and other polar molecules the table is rather complete. It is to meet this ommission that a second, much less defendable criterion has been set for the total impurity pressure:

$$\sum_i p_i << \frac{\sigma_{Kr}(v_r)_{Kr}}{\max_i(\sigma_i(v_r)_i)} p_{Kr}^{min} \qquad (12)$$

This still leaves an undeterminacy, since the maximum of the product of orientation cross-section and relative velocity is not really known. Moreover the total impurity pressure consists of two parts; a fixed amount is due to the impurities in the filling gas (a fraction F of 2.10^{-5} of the filling pressure in our case) and secondly an amount due to desorption from the vessel wall which increases linearly with time at a rate of $dp/dt = 1.75\ 10^{-9}$ mbar/s. In practice, since there is no easy way to further reduce the level of impurities in the filling gas we set a limit on the time an experiment may require. This hold time T is:

$$T << \frac{F\, p_{Kr}^{min}}{\left(\frac{dp}{dt}\right)} \qquad (13)$$

Thus an experiment of several hours can be carried out without risking an overly heavy contribution to the depolarization cross section due to impurity gases.

2.4.3. *Rubidium density and optical absorption*

The density of rubidium atoms in the long discharge tube in Figure 3 may be strongly non- uniform due to diffusion of rubidium atoms in the buffer gas and due to reaction of rubidium with impurity gases. Therefore we calculate the rubidium density from a one dimensional reaction-diffusion model. If we define the mole fraction rubidium x as:

$$x = \frac{n}{n+N} \sim \frac{n}{N} \qquad (14)$$

where n is the number of moles rubidium and N the number of moles krypton, then x is subject to the following boundary value problem:

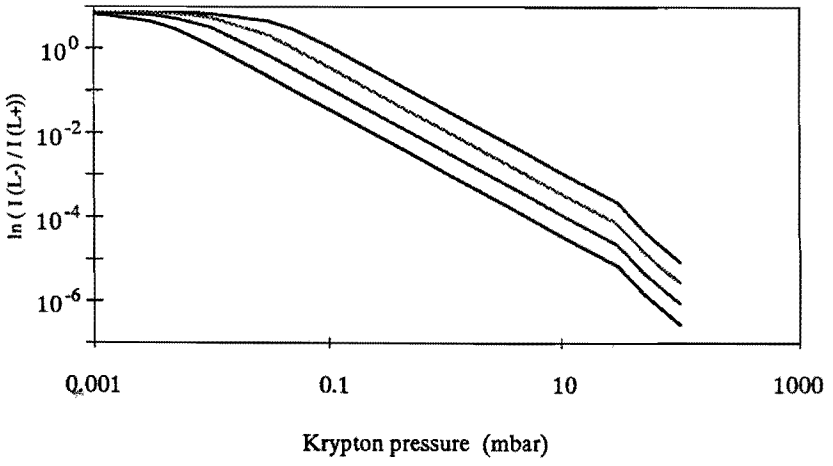

Figure 8 Absorption of a laser beam as a function of krypton pressure

The absorption of a resonantly tuned laser beam is plotted in this graph as a function of the krypton pressure. Four curves corresponding with four values of the impurity concentration y (1, 10, 100 and 1000 ppb) are shown, demonstrating the enormous impact of even a very small impurity level.

Table 6 Impedance characteristics of two pieces of air-line

Frequency	3035 MHz		6894 MHz	
	Real part [Ω]	Imaginary part [Ω]	Real part [Ω]	Imaginary part [Ω]
Air-line piece				
Ideal	50.000	0.000	50.000	0.000
'Closed'	54.844	9.574	54.768	-13.068
'Symmetric'	48.793	16.424	52.408	-8.199

$$\frac{\partial x}{\partial t} = D\frac{\partial^2 x}{\partial z^2} + \frac{D}{1 - x_0}\left[\frac{\partial x}{\partial z}\right]_{z=0}\frac{\partial x}{\partial z} - kz \qquad (15)$$

with boundary conditions:

$$z = 0\ x = x_0;\ z = \infty\ x = 0 \qquad (16)$$

This equation, with reaction constant k = 0, was solved by Arnold [34]. both Eq. 15 and Arnold's solution differ from the usual diffusion equation as they allow for the displacement of the buffer gas by rubidium atoms. Since the rubidium density is always extremely small in our case, the correction φ to the more common solution of the normal diffusion equation is very small indeed:

$$x = x_0\frac{1 - \mathrm{erf}\left[\frac{z}{\sqrt{4Dt}} - \varphi\right]}{1 - \mathrm{erf}\,\varphi} - x_0\,\mathrm{erfc}\left[\frac{z}{\sqrt{4Dt}}\right] \qquad (17)$$

This solution holds for k = 0. If k differs from zero the solution is obtained by a procedure given by Danckwerts [35]. In the limit where t goes to infinity, it follows that:

$$x = x_0\exp\left[-\frac{z}{\zeta}\right] \qquad (18)$$

with:

$$\zeta = \sqrt{\frac{D}{k}} = \sqrt{\frac{D^0 p^0}{\beta y}}\,p^{-3/2}, \qquad (19)$$

where the implicit dependance of the diffusion and the reaction on krypton pressure p was made explicit. This was done by writing $D = D^0p^0/p$ and $k = \beta p^2 y$. Here y is the impurity concentration, β is the (chemical) reaction constant, $p^0 = 101325$ Pa and D^0 is the normalized diffusion constant. Using this exponentially decaying rubidium density in Beer's law gives for the absorption of a resonant laser beam in a tube of length $(L^+ + L^-)$ and with a rubidium particle concentration n_0 at the origin:

$$-\ln\left[\frac{I(L^+)}{I(L^-)}\right] = \sigma_0 n_0 \zeta\left[2 - \exp\left[-\frac{L^+}{\zeta}\right] - \exp\left[-\frac{L^-}{\zeta}\right]\right]. \qquad (20)$$

Here it is assumed that the rubidium source is located at the origin, whereas the entrance and exit windows are located at L^- and L^+ respectively.

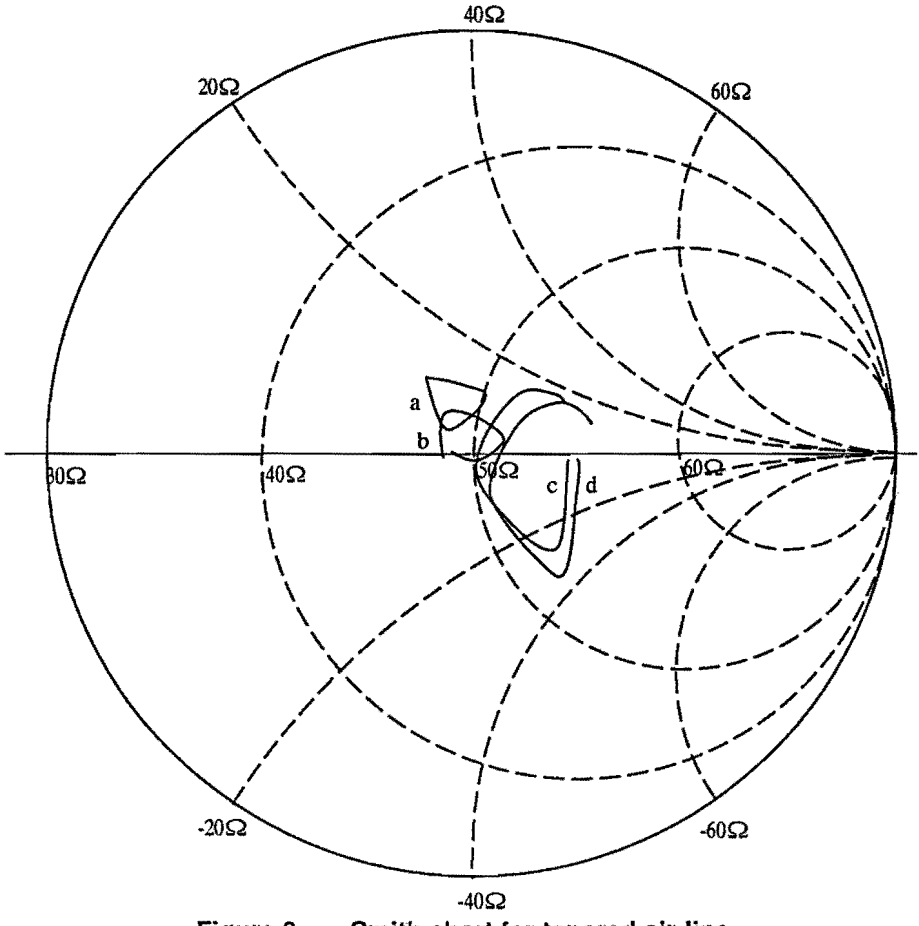

Figure 9 Smith chart for tapered air-line

The Smith chart is a polar display of complex impedance with the grid-lines arranged in a peculiar way so that impedance transformations can be carried out by rotating a point around the mid point. An ideal piece of microwave instrumentation will have a frequency independent complex impedance of (50 Ω, 0 Ω) corresponding with a point in the middle of the Smith chart. The curves drawn show the variation of the complex impedance of the air-line pieces with frequency. Each of the two (symmetrical and closed) samples of air-line was measured in a 100 MHz interval around 3035 MHz and 6894 MHz. Thus the ground state hyperfine splittings of both ^{85}Rb and ^{87}Rb are covered by these plots.The curves are annotated as follows: a: Symmetric sample at 3035 MHz, b: Closed sample at 3935 MHz, c: Symmetric sample at 6894 MHz, d: Closed sample at 6894 MHz.

Since ζ is a function of the krypton gas pressure the absorption may be expressed as a function of the krypton pressure. A decrease in absorbtion with increasing krypton pressure is found mainly due to the high reaction rate of rubidium with impurity gases. This is illustrated in Figure 8. At krypton pressures above 50 mbar (=5000 Pa) the decrease of the photon cross section σ_o due to pressure broadening of the resonance line must be taken into account. This was done by calculating the maximum value of a pressure broadened line as:

$$\sigma_{max} = \sigma_o \exp(a^2) \operatorname{erfc}(a) \qquad (21)$$

where a is the damping ratio defined later in Eq. 25. It can be shown [41] that, for large a (a > 2) the correction factor in Eq. 21 approximates $\pi^{-1/2}a^{-1}$. A value for the diffusion constant D^o was taken from [36], this value was measured for ^{85}Rb in Ar. The value for the reaction constant is probably a little too high because we took the value for the reaction of Cs with traces O_2 from [6]. Figure 8 shows that absorption of a resonant laser beam strongly decreases with increasing krypton pressure. In this figure the impurity concentration is kept constant at 1 ppb.

2.4.4. *Transmission line characteristics*

Ideally a reflection-less and loss-less transmission line is required for swept frequency double-resonance spectroscopy. Only then the flow of microwave power through the detection center is constant, and the fluorescence signal will not vary with position of detection center in the transmission line. Since most of the transmission line is of well defined commercial quality, most attention was paid to the doubly-tapered air-line. We measured impedance, return loss and (voltage) Standing Wave Ratio (SWR) of the airline on an automatic vector-network analyzer (HP8510A, HP8511A, HP8341B). Both narrow-band and broad-band measurements were carried out on two essentially similar pieces of air-line; one symmetric in all respects the other as 'closed' as possible.
Results of the impedance measurements are given in Figure 9 and Table 6 respectively. The impedance measurements were done in a 100 MHz band around the ground state hyperfine splitting of ^{85}Rb and ^{87}Rb respectively (3035 MHz and 6894 MHz). Frequency dependent impedances are observed in both cases for both pieces of air-line. The observed deviations from ideality, however, are not essential. The broad band return loss and SWR measurements, presented in Figure 10 confirm this result. We may conclude that both pieces of air-line suit our purposes well enough. Moreover as the difference of maximum microwave power and minimum power ('knot') relative to the incident power P_{in} is:

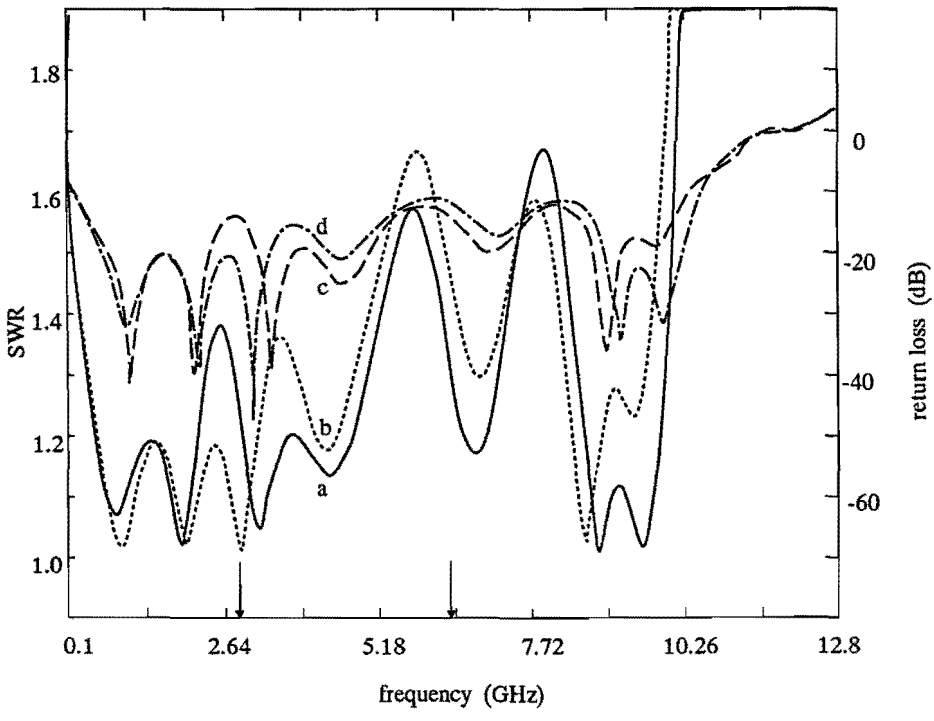

Figure 10 Reflection loss and standing wave ratio for air-line

Broadband reflection loss (dB) and voltage Standing Wave Ratio (SWR) of the two samples of tapered air-line. The curves marked a and c belong to the closed sample, while the curves marked b and d belong to the symmetrical sample. The microwave hperfine transition frequencies for ^{85}Rb and ^{87}Rb are indicated by markers. The curves marked a and b belong to the SWR scale on the left, whereas the curves marked c and d belong to the return loss scale on the right. A slight frequency shift between the two sets of curves was introduced for reasons of clarity.

$$\frac{P_{max} - P_{min}}{P_{in}} = \frac{\Delta P}{P_{in}} = 2\left[\frac{SWR^2 - 1}{SWR^2 + 1}\right] \qquad (22)$$

Although this quantity may take values up to 0.97 (for SWR = 1.7) it is relatively insensitive to small frequency deviations, unless the resonant frequency is located near a sharp minimum of the SWR curve in Figure 10. Moreover, the spacing between points with maximum and minimum power is equal to half the wavelength. Thus, unless the detection volume happens to be coincident with a knot, the distribution of microwave power over the detection volume may be taken to be constant.

2.4.5. *Optical detection efficiency*

Strictly speaking the detection efficiency is a function of position in the detection volume. In this work, however, we assume that the variation of detection efficiency with position is small, and that the detection efficiency is zero outside the detection volume. Hence we may write:

$$\eta(\lambda) = \varepsilon(\lambda) \prod_i T_i(\lambda) \frac{1}{16} \frac{1}{(f/\#)^2} \left[\frac{M}{M+1}\right]^2 \qquad (23)$$

where ε is the wavelength dependant quantum efficiency of the photomultiplier, T_i is the transmission of component 'i', which is a strong function of wavelength if 'i' happens to be a filter. The remaining part of the expression is the geometric efficiency; f/# is the lenses numerical aperture (f-number, or stop number) and M the linear magnification. Except for the filter transmission all factors in the expression of Eq. 23 are common to every measurement. Hence in taking ratio's of experimental signals all factors cancel out and the ratio of two filter transmissions remains. We calibrated the transmission of the optical components using an (uncalibrated) tungsten ribbonlamp, an 0,25 m Ebert monochromator (Jarrell-Ash) with 100 µm slits, a (GaAs photocathode) photomultiplier (RCA C31034) and a photon counter (EGG 1120). Typical transmission curves for several components are given in Figure 11.
All curves were obtained under conditions of near normal incidence. Any deviation from normal incidence causes an effective broadening of interference filter peak half-width. Such deviations are caused by e.g. non-negligible dimensions of the detection volume. Since in our case the detection volume has a length of 10 mm, we chose the length of the image of the tungsten ribbon spatially accepted by the monochromator 10 mm as well. Thus the measured transmission curve matches the transmission of the actual detection system.

While measuring direct fluorescence the counting rate may exceed the range of linear response of the detection system even if a neutral density filter is used to attenuate the photon flux. In order to correct for this dead time effect

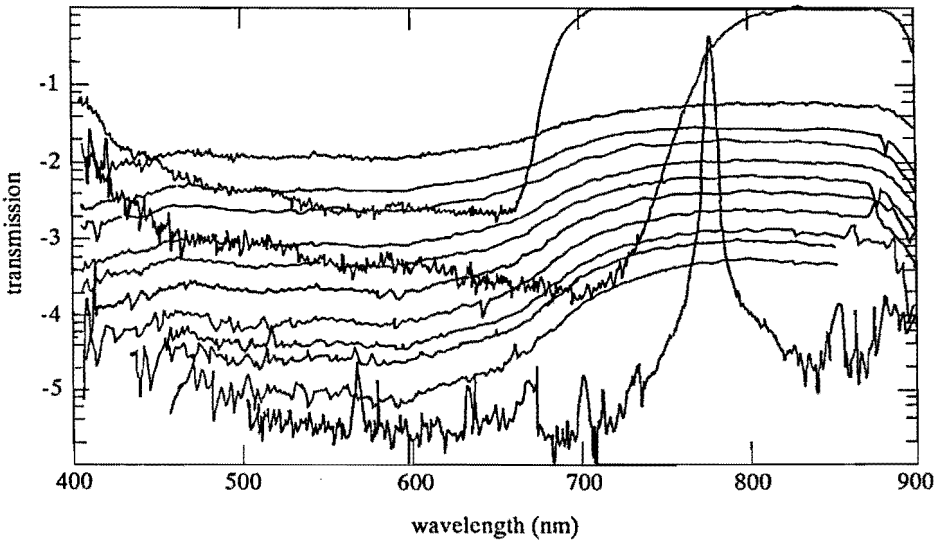

Figure 11 Transmission of optical filters

Measured transimission of 10 neutral density filters, two long pass filters and one three cavity interference filter. Typical transmission at 546 nm is specified, but note the increase in transmission at wavelengths larger than 650 nm.

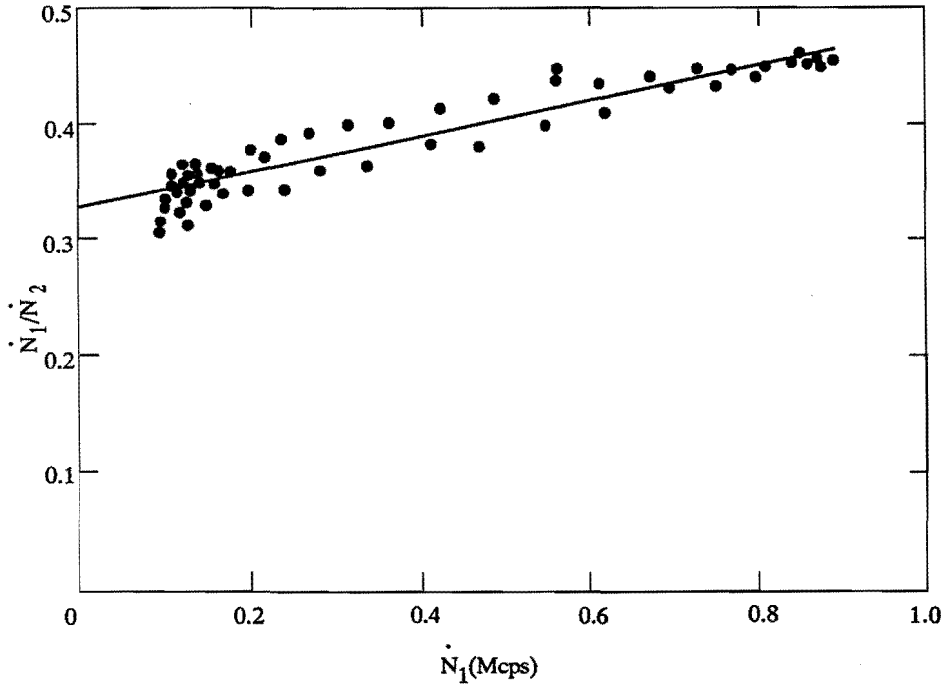

Figure 12 Dead time of photon counting set-up

The approximately linear relation between the ratio of count rates of two series and the count rate of the first series, allows a determination of the dead time of the set-up by a simple model based upon correction of effective measuring time. The dead time can than be found from the slope of the fitted straight line as 198 ns.

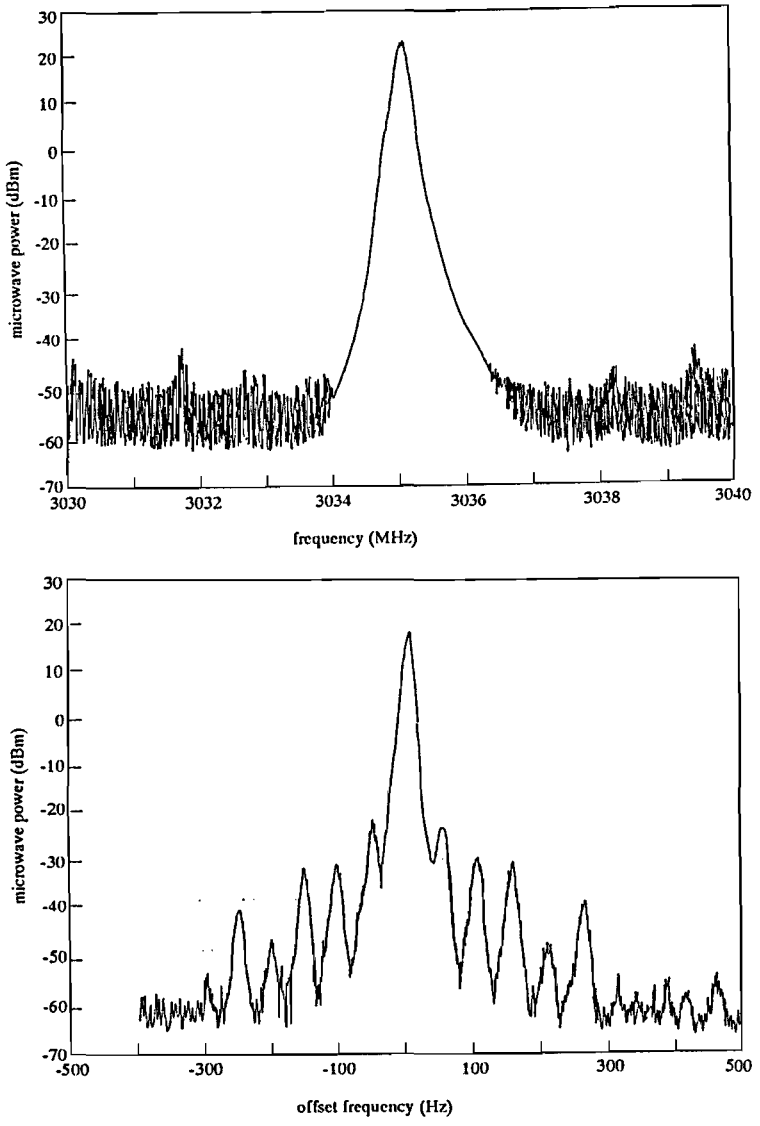

Figure 13 Spectral analysis of the microwave master oscillator and the microwave amplifier

The upper plot shows the line shape of the BWO oscillator and TWT amplifier combination. The vertical axis is calibrated in dBm units. This is an absolute calibration; by convention 0 dBm equals 1 mW. The width of the peak indicates that this oscillator is hardly suited for the detection of double resonance signals, which have a width which is about 30 times smaller. The lower plot shows the line shape of a highly stabilized klystron as amplified by the TWT. Clearly the TWT preserves the line shape of the master oscillator.

we measured the dead time by taking the ratio q(k) of two experimental line profiles $M_1(k)$ and $M_2(k)$ (where k is the channel index). (This procedure is due to Kerstel [37].) The ratio of the true signals $N_1(k)$ and $N_2(k)$ is a constant q^o independant of k and equal to the transmission of the neutral density filter inserted after measuring $N_1(k)$. A simple model, based upon correction of effective measuring time, then relates N_1 to M_1 and N_2 to M_2. If τ is the dead time of the detection system, q can be shown to be linearly dependent on $M_1(k)$:

$$q(k) = q^o + \tau (1 - q^o) M_1(k) \qquad (24)$$

This relation is illustrated in Figure 12. A least-squares adjustment to this data gives the deadtime of our detection setup as τ = 198 ns.

The appearance of slight hysteresis in Figure 12 indicates frequency drift of the diode laser. Numerical simulation shows that small drifts of the order of 1% of the Doppler width at room temperature can be spotted by the appearance of hysteresis loops. Every systematic and channel number dependant error may be detected this way, hence deadtime measurements are routinely carried out at regular intervals. The absence of hysteresis indicates the absence of drift, trigger errors, synchronisation errors and the like and serves to strengthen the reliability of the data obtained. Note that Figure 12 shows that a linear relationship between q(k) and $M_1(k)$ holds up to at least 1 MHz counting speed. Thus deadtime corrections on the order of 20% may, in any case, be carried out safely!

2.4.6. *Spectral analysis of the microwave oscillator*

Due to the absence of pressure broadening effects, the width of the hyperfine groundstate transition is extremely small. It may range from the Doppler value of several tens of kilo Hertz down to a Dicke narrowed value of several tens of Hertz . Therefore the spectral width of the microwave oscillator should not exceed a few Hertz. This condition is all but fulfilled as is shown by Figure 13.

Here a spectral analysis of the BWO + TWT combination in sweep mode is presented. In measuring this profile the spectrum analyzer (HP 8566B) and the BWO were synchroneously triggered, but were sweeping at different rates. Thus a stationary display is obtained where the spike on the low frequency side of the main peak indicates cross talk between the (internal) trigger pulse generator and the the BWO's helix. This spike is not at microwave frequencies, so in double resonance experiments it will disappear. Although the spectral profile of the microwave oscillator is at least 40 kHz wide (FWHM) absolute density measurements are still possible if the shape is known or assumed to be gaussian. In that case the peak area can be calculated and used in the calculation of the integrated polarisation (see 2.4.1).

Table 7 Saturation intensities for a pressure broadened two level system a)

a^{-2}	a	p [mbar]	I_S b) [mW/mm^2]	a exp(a^2) erfc(a)
0.25	2.000	69.0	37.6	0.511
0.20	2.236	77.2	41.4	0.519
0.15	2.580	89.2	46.9	0.529
0.10	3.160	124.6	56.3	0.539
0.05	4.472	154.9	78.0	0.551
0.01	10	346.8	171	0.561
0	∞	∞	∞	0.564
∞	0	0	9.61	

a) At a temperature corresponding to 500 MHz Doppler width (approximately room temperature).

b) $$I_S = \frac{hc}{\lambda}\frac{1}{\sigma_0 \tau}\, a \frac{1}{a \exp(a^2)\, \mathrm{erfc}\, a}$$

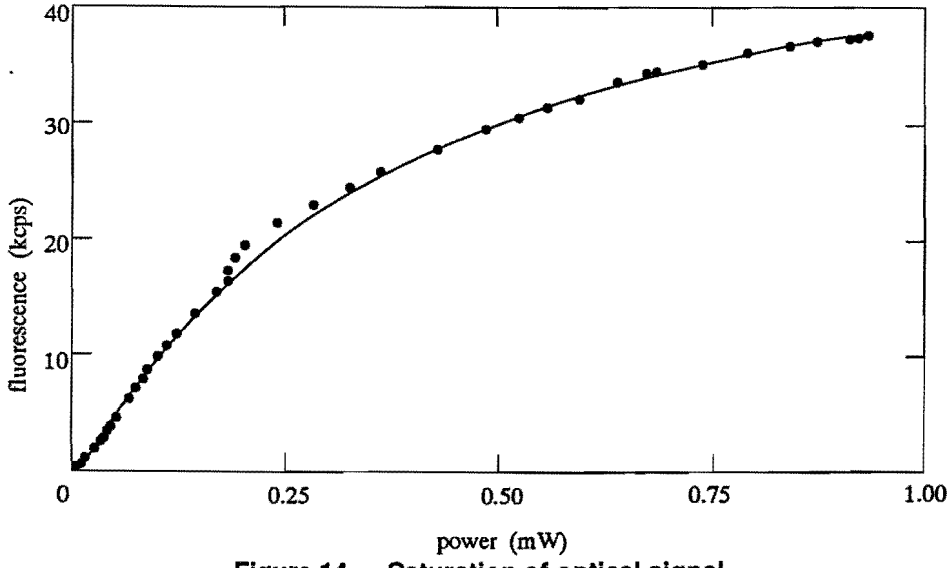

Figure 14 Saturation of optical signal

In vacuum, saturation was measured as a less than linear increase of the fluorescence count rate with increasing beam power. The flattening of this curve shows that hyperfine optical pumping occurs at beam powers above 0.1 mW. This is much lower than the saturating beam power in a two level system. At low buffer gas pressures, hyperfine optical pumping will occur at even lower power levels. This is due to reduced diffusional relaxation.

Next in importance to width comes stability. Efficiency considerations dictate the sweep width used to be as small as possible, say ten times the largest width encountered. Thus 400 kHz sweeps should be typical. In practice however, 1 MHz sweeps must be used. The stability of the BWO is affected by several influences not easily accounted for. Therefore we measured the stability of the whole microwave set-up with a gated counter. Moreover, as was explained in 2.4. the experiment itself may serve to indicate frequency drifts.

2.4.7. *Diode laser: power and spectral stability*

Because the primary function of the diode laser is to create a non-thermal population of the hyperfine splitted groundstates, we evaluated its beam properties in terms of saturation of the fluorescence signal. A necessary condition to carry out such an evaluation is that the frequency of the laser beam remains linked to the (pressure-shifted) absorption line. At pressures below 10 mbar this can be accomplished by locking the wavelength to an evacuated reference cell containing pure metallic rubidium. For our locking scheme this results in a stability better than 1 MHz and an offset from exact resonance less than 5 MHz. At pressures above 10 mbar the pressure shift becomes too large and we have to rely on the intrinsic stability of the diode laser which can be calculated from the known curve and mode structure of our diode laser. Figure 14 summarizes this. For a pressure broadened two-level system the saturation parameter S_0 is:

$$S_0 = \frac{i}{i_s} = \sigma_0 i\tau \exp(a^2)\,(1 - \mathrm{erf}\, a) \qquad (25)$$

Here σ_0 is the cross section at the top of a Doppler broadened absorption line, i the photon flux, τ the upper state lifetime, i_s the saturating photon flux, and a the (natural) damping ratio [38] which is the ratio of pressure width $\Delta\nu_P$ plus natural width $\Delta\nu_N$ to Doppler width $\Delta\nu_D$ times a normalization factor.

$$a = \frac{\Delta\nu_P + \Delta\nu_N}{\Delta\nu_D}\sqrt{\ln 2} \qquad (26)$$

By inspection of Table 7 it becomes clear that saturating intensities I_s may become very large indeed.

In a three level system, however, saturation due to hyperfine optical pumping may occur at intensities well below the intensities calculated above. A rate equation model gives for the saturating photon flux;

$$i_s = \frac{g_2}{g_1}\,\frac{R}{\sigma_0\tau \exp(a^2)\,\mathrm{erfc}\, a}\,\frac{1}{A} \qquad (27)$$

where R is the total relaxation rate of the (upper) overpopulated ground level,

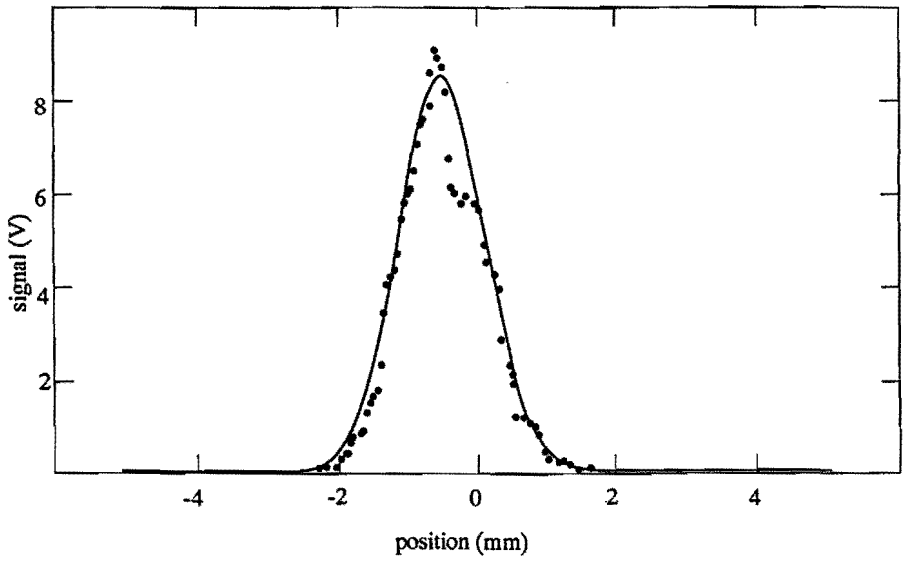

Figure 15 Beam profile (horizontal) of diode laser

A scanning slit is an easy to use beam profiler. For laser beams that are nearly gaussian, the transmission throught the slit at each position can be calculated. The solid line shows a least squares fit of the data to this calculated transmission, yielding a waist radius of 0.75 mm.

g_2 and g_1 are the statistical weights of the upper and lower ground level respectively and A is the sum of reciprocal decay frequencies due to spontaneous emission. Here saturation is defined as being the case whenever the photon flux exceeds a value needed to double the thermal population ratio of the ground levels. This thermal ratio of course equals the ratio of statistical weigths Referring to Figure 2 for explanation of the notation, we may express the experimental signal for direct fluorescence D as:

$$D = \eta\, n\, V \frac{S_0 A_{41}}{1 + \frac{g_2}{g_1}\left[1 + \frac{S_0}{RA}\right] + S_0 \frac{A_{41}}{A_{42} + A_{41}}} \qquad (28)$$

Here quenching has been neglected, and we assume a three level model i.e. we disregarded the existence of the 5 $^2P_{1/2}$ level. This non-linear relation between fluorescence and photon flux is typical for three level systems with a non resonant intermediate level. It is illustrated in Figure 14, where the fluorescence signal, corrected for background contributions has been plotted as a function of intensity.

.

Here intensity is calculated by measuring the total beam power with a large area photodiode (BPW34) and dividing this by the square of the waist radius times π. The beam profile is usually assumed to be nearly gaussian with a 0.75 mm waist radius. Whenever necessary a new profile is measured using a 100 μm scanning slit. A typical measurement is given in Figure 15

2.5. Sample results

2.5.1. Optical spectra

Rather than measure, we calculated a number of pressure broadened optical spectra in the impact regime. The calculation of absolute photon cross-sections is not very complicated and has been explained elsewhere [39]. In general the result is:

$$\sigma_i^{FF'}(\nu) = \sigma_i^{FF'}\, L_i(\nu) \qquad (29)$$

Here i specifies a particular isotope, F and F' denote hyperfine quantum numbers of the lower and upper level, ν is the frequency and σ is the photon cross section. The line profile function L is normalized to one. In the impact regime the line profile is a convolution of natural, Doppler and pressure broadening, resulting in a Voigt profile [40]:

$$L_i^{FF'}(\nu) = \frac{2}{\Delta\nu_D}\sqrt{\frac{\ln 2}{\pi}}\,\frac{a}{\pi}\int_{-\infty}^{\infty}\frac{\exp(-y^2)}{a^2 + (\omega - y)^2}\,dy \qquad (30)$$

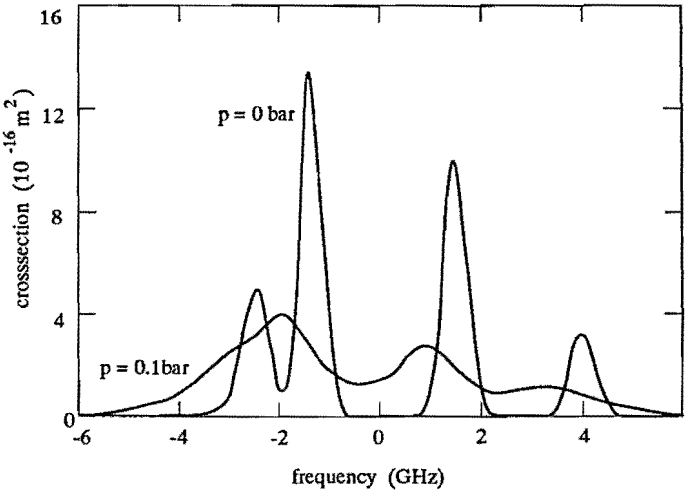

Figure 16 Pressure broadened photon cross section spectrum for naturally abundant rubidium

This graph illustrates the enormous impact on the width and height of the photon cross section peaks of the addition of 100 mbar of krypton.

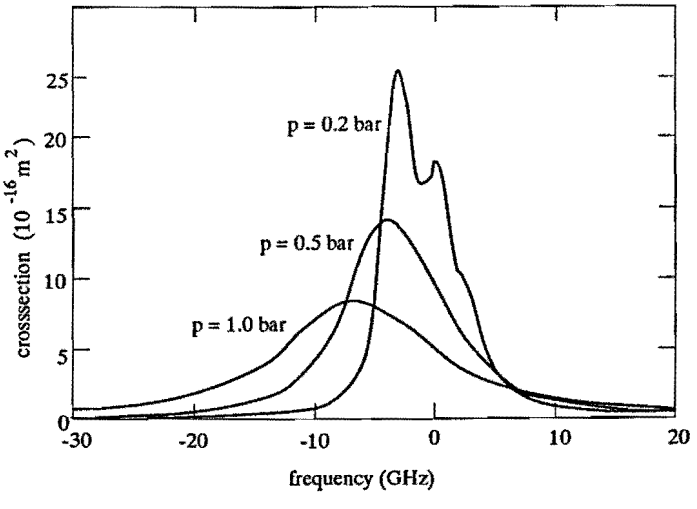

Figure 17 Pressure broadened photon cross section spectrum for naturally abundant rubidium at somewhat higher pressures

As is demonstrated by this graph, upon increasing the krypton pressure, the separate hyperfine and isotope peaks merge into one broad peak. The 14.4 Mhz/mbar pressure broadening makes an identification of the isotopes impossible.

with;

$$a = \frac{\Delta\nu_N + \Delta\nu_P}{\Delta\nu_D}\sqrt{\ln 2} \qquad (31)$$

and;

$$\omega = 2\frac{\nu - \nu_{0i}^{FF'} - \gamma_P}{\Delta\nu_D}\sqrt{\ln 2} \qquad (32)$$

a is the damping ratio as defined by Mitchell and Zemansky [38], ω is the normalized frequency. The remaining symbols are explained as follows: $\Delta\nu_D$ is the Doppler width (FWHM), $\Delta\nu_N$ is the natural width (FWHM) and $\Delta\nu_P$ is the pressure width (FWHM). The pressure shift is γ_P, whereas $\nu_{0i}^{FF'}$ is the line center frequency of line component FF' of isotope i. The Voigt integral in Eq. 30 is equal to the real part of the complex error function [41], this quantity can be approximated by a simple algorithm due to Gautschi [42][43]. Now by adding, at each value of the frequency ν, the contribution of each line component, a spectrum may be obtained. For naturally abundant rubidium (72.165% ^{85}Rb, 27.835% ^{87}Rb) the results are given in Figure 16 and in Figure 17. At low optical densities these spectra closely approximate a measured spectrum since the flux of photons impinging on a fluorescence detector is proportional to:

$$1 - \exp(-\sigma(\nu)nl) \sim \sigma(\nu)nl \qquad (33)$$

where n is the rubidium (atom) density and l the absorption length 'seen' by the detector. Every calculated spectrum has been checked by calculating the integral of it over ν, which must be independant of both broadening and hyperfine structure:

$$\int_0^\infty \sigma(\nu)\,d\nu = \sum_i \sum_{FF'} \int_0^\infty \sigma_i^{FF'}(\nu)\,d\nu = \frac{\lambda_0^2}{8\pi}\frac{2J'+1}{2J+1}\frac{1}{\tau} \qquad (34)$$

Applying this result will help foster confidence in the calculation of the photon cross section. The left hand side of Eq. 34 can be integrated numerically, whereas the right hand side is known from basic atomic data [14]; λ_0 is the line center wavelength (780027 pm for the D_2 line of rubidium), τ is the excited state lifetime (28.5 ns for the $5^2P_{3/2}$ state of rubidium) and J and J' are the fine structure quantum numbers (1/2 and 3/2 respectively for the D_2 line of rubidium).

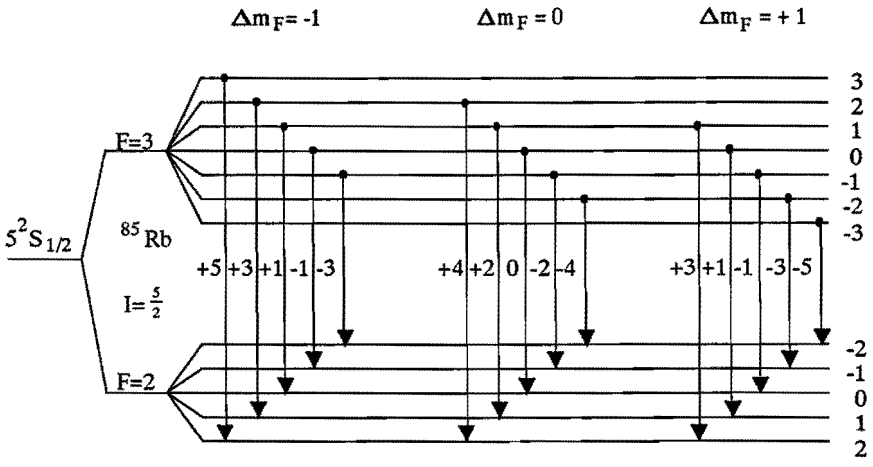

Figure 18 Zeeman splitting of hyperfine splitted ground states in ^{85}Rb

This figure shows the equidistant energy levels of the two groundstates in a weak magnetic field. It is typical for the anomalous Zeeman effect. The numbers written next to the possible transitions indicate the number of Zeeman shifts (14 kHz/μT) for that transition.

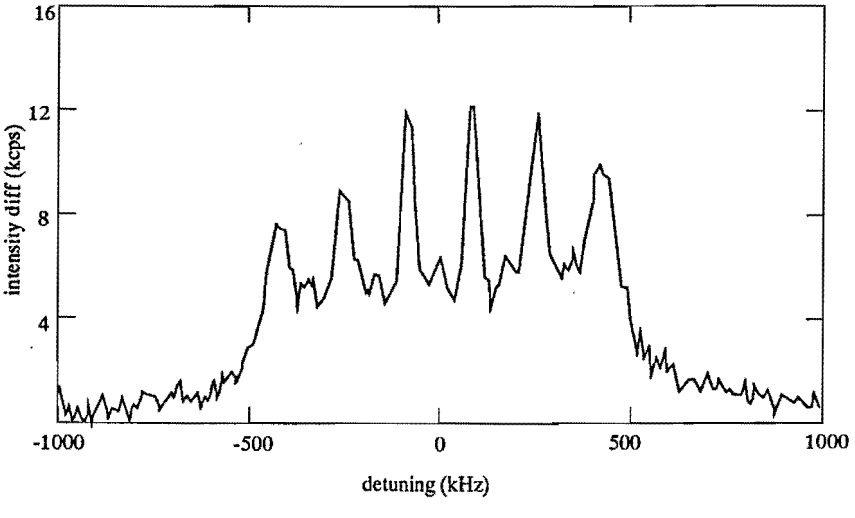

Figure 19 Zeeman spectrum in perpendicular fields

This graph was measured with the two coil-pairs energized such that the earths magnetic field was almost cancelled. The remaining coil pair was energized to provide a quantising field ar right angles with the driving field.

2.5.2. *RF spectra*

Due to the extremely high resolution attainable in double resonance spectroscopy, an otherwise hidden feature becomes visible. The extremely small Zeeman splitting of the hyperfine splitted ground states leads to 2F + 1 sublevels with energy E relative to the unperturbed energy E_0:

$$E - E_0 = g_F \mu_B m_F B_{ext} \qquad (35)$$

with $m_F = -F, -F+1, ..., F-1, F$ the magnetic hyperfine quantum number, μ_B the Bohr magneton and B_{ext} the magnetic induction of an external field. The Landé factor g_F can be calculated from perturbation theory:

$$g_F = g_J\left[\frac{F(F+1) + J(J+1) - I(I+1)}{2F(F+1)}\right] - g_I \frac{m_e}{m_p}\left[\frac{F(F+1) + I(I+1) - J(J+1)}{2F(F+1)}\right] \qquad (36)$$

Since the electron to proton mass ration m_e/m_p is small the second term can be neglected safely. The 'J' Landé factor g_J in Eq. 36 is:

$$g_J = 1 + \frac{J(J+1) + S(S+1) - L(L+1)}{2J(J+1)} \qquad (37)$$

The microwave transition frequencies are thus shifted acoording to:

$$\nu - \nu_0 = (g_{F'} m_{F'} - g_F m_F)\frac{\mu_B B}{h} \qquad (38)$$

The frequency shifts can be calculated and the result, for ^{85}Rb, is given in Figure 18.

It turns out that, disregarding any possible selection rules, 11 equally separated Zeeman lines can be observed. In practice this is exactly what one sees; in the earth's magnetic field (B = 40 μT) the angle between the driving field (B_{RF}) vector of the microwave radiation and the quantising field (B_{QF}) vector of earth's magnetic field is neither 0^o nor 90^o. Thus there is no selection rule effective:

$$\Delta m_F = 0 \quad \text{if } B_{RF} \text{ parallel to } B_{QF} \qquad (39)$$

$$\Delta m_F = \pm 1 \text{ if } B_{RF} \text{ perpendicular to } B_{QF} \qquad (40)$$

By manipulating the currents in three mutually perpendicular Helmholtz like coil-pairs, it is possible to choose the orientation and the strength of the quantising field at will. This is illustrated in Figure 19 and in Figure 20 where the fluorescence signal is plotted as a function of applied microwave frequency. In Figure 19 six peaks are manifest in accordance with the selection rule $\Delta m_F = 1$ valid for perpendicular fields.

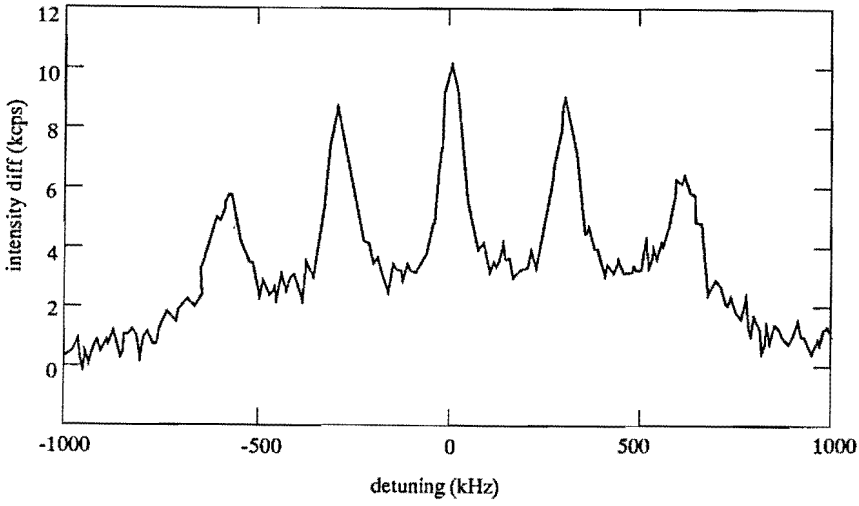

Figure 20 Zeeman spectrum in parallel fields

This plot is essentially the same as the preceding one. However, here the coils were energized such as to make the driving and quantising fields align.

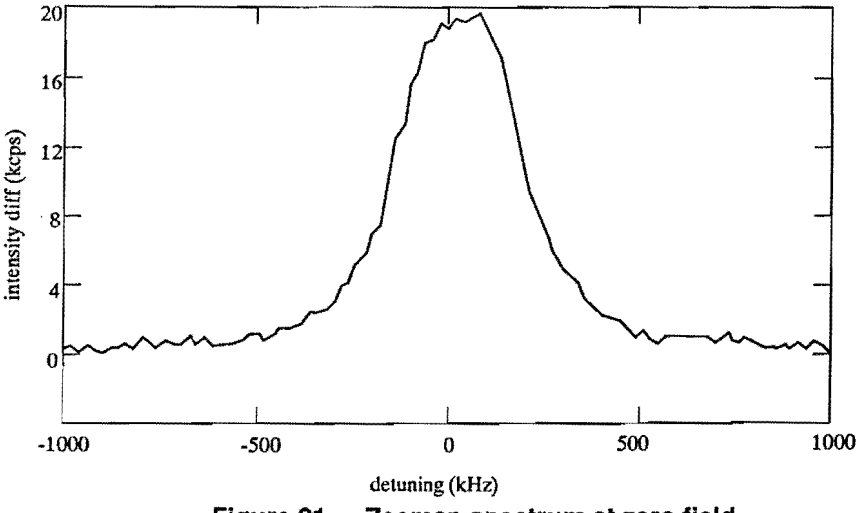

Figure 21 Zeeman spectrum at zero field

This graph shows the extend to which it was possible to nullify the local earth's magnetic field. Complete cancellation would have produced a peak with a width equal to the Doppler witdh (about 50 kHz). The peak width here, being about six times as large, indicates that a residual, unresolved Zeeman splitting is still present.

In Figure 20 five peaks signal the activity of the $\Delta m_F = 0$ selection rule as it should for parallel fields. The relative intensity of the Zeeman components can be calculated through the use of Wigner d-functions [44], which describe the purely geometric mapping of level densities quantized along the magnetic field upon level densities quantized along the driving field axis. These intensities, however, are of no concern to us, since working from the known strength and orientation of the magnetic field which follows from Figure 19 or Figure 20, the magnetic field can be nullified. This is most easily done for parallel fields as we have a two dimensional problem then.

The result of nullifying the field is shown in Figure 21 where the resulting magnetic field from the three coil pairs is given a value, equal to but opposing the local earth's magnetic field. The individual Zeeman components are not resolved in this graph, but the peak is much broader than the individual Zeeman peaks, due to a mismatch in the field compensation.

In order to assess the possibility of obtaining double resonance signals at higher buffer gas pressures, we calculated the peak width and (relative) peak height as a function of buffer gas pressure. Again, the calculation can be decomposed in the determination of a line shape function and the calculation of a (relative) line strength.

2.5.3. *Microwave lineshape*

The microwave absorption lineshape is more complicated than the optical line shape of paragraph 2.5.1. As was first demonstrated by Dicke [45] a considerable reduction of the Doppler width may occur due to 'motional narrowing'. A complete derivation of the line shape in the framework of the impact theory was given by Sobelman [46]. The result is:

$$L(\nu) = \frac{1}{\pi}\frac{e^{\alpha}}{\beta}\,\mathrm{Re}(\alpha - \mu/\beta\,\gamma(\mu/\beta,\alpha)) \qquad (41)$$

where;

$$\mu = i\,2\pi(\nu-\nu_0) + (\sigma'-i\,\sigma'')N\nu_r + \frac{(2\pi\nu_0)^2}{c^2}D \qquad (42)$$

$$\alpha = \frac{(2\pi\nu_0)^2}{c^2}\frac{D}{\beta} \qquad (43)$$

$$\beta = \frac{RT}{M_{Rb}D} \qquad (44)$$

and where γ is the incomplete gamma function. It can be shown that the line shape function of Eq. 41 is normalized to one as it should. The meaning of the many synbols in Eq. 41 is given in Table 8 , where appropriate representative numerical values have been compiled as well.

Table 8 Microwave absorption line shape

Symbol	Name	Unit	Value	Note or formula	Reference
ν_o	Hyperfine frequency	MHz	3035	^{85}Rb	[47]
ν_o	Hyperfine frequency	MHz	6894	^{87}Rb	[47]
N	Gas density	m^{-3}		$N = p/kT$	
v_r	mean relative speed	$m\ s^{-1}$	386	$v_r=\sqrt{\frac{8}{\pi}RT\frac{M_{Rb}+M_{Kr}}{M_{Rb}M_{Kr}}}$	
c	speed of light in vacuum	$km\ s^{-1}$	299792		[48]
D	Diffusion constant	m^2s^{-1}	$1.3\ 10^{-5}$	^{85}Rb in Ar	[36]
R	Gas constant	$Jmol^{-1}\ K^{-1}$	8.314		[48]
M_{Rb}	Molecular weight of rubidium	g	85.4678	Naturally abundant	[49]
M_{Kr}	Molecular weight of krypton	g	83.80	Naturally abundant	[49]
σ''	Line shift collision integral	m^2		$\sigma''=2\pi\int_0^\infty(1-\cos\eta(\rho))\rho d\rho$	[46]
σ'	Line broadening collision integral	m^2		$\sigma'=2\pi\int_0^\infty\sin\eta(\rho)\rho d\rho$	[46]
Λ_{11}	Diffusion length	m		$\Lambda_{11}=\frac{1}{\sqrt{\left[\frac{j0.1}{R}\right]^2+\left[\frac{\pi}{H}\right]^2}}$	[50]

The impact theory collision integrals σ' and σ'' describe the broadening and shift of the spectrum line due to phase shifts imposed on the colliding radiator. If we assume an attractive r^{-6} potential (Van der Waals), Sobelman [46] shows that the integrals can be reworked into a frequency shift parameter Δ and into a broadening parameter Γ:

$$2\pi \Delta = N v_r \sigma'' \tag{45}$$

$$2\pi \Gamma = 2 N v_r \sigma' + 2 \frac{\omega_o^2}{c^2} D \tag{46}$$

Since the frequency shift with increasing pressure has been measured very accurately (because of the obvious applications in atomic clocks) a value for the cross sections σ' and σ'' may be obtained by application of Eq. 45 and of Eq. 46. The final result of this paragraph is an illustration of the effect predicted by Dicke. It follows from Eq. 46 that the variation of width of the absorption line with buffer gas pressure is:

$$2\pi \Gamma = 2 v_r \sigma' N_o \frac{p}{p^o} + 2 \frac{\omega_o^2}{c^2} D_o \frac{p^o}{p} \tag{47}$$

which is illustrated in Figure 22. The value of the constants used in Eq. 47 has been listed in Table 8. The decreasing linewidth with increasing pressure is known as 'Dicke narrowing'.

2.5.4. *Influence on the polarization*

In paragraph 2.2. , Eq. 2 and Eq. 3 the groundstate polarization P was introduced and defined as:

$$P = \frac{n_2 - n_1}{n_2 + n_1} \tag{48}$$

where n_1 and n_2 are the population densities of the two, hyperfine splitted groundstates. The polarization P determines whether an isotope can be selectively detected in a high pressure buffergas or not. This is due to the fact that the OMDRS method is based upon creating a non-thermal population in the groundstates, i.e. a polarization differing from the thermal value 0.167. If the pressure broadening of the optical pumping lines becomes too large, both groundstates will be pumped and the polarization will not change. In order to quantify this, we have solved a system of rate equations for the population densities of the four levels that are involved (see Figure 2). The polarization can then be calculated as a function of buffergas pressure for various combinations of the intensity of the laser beam and the microwave field. The system of rate equations can be written as:

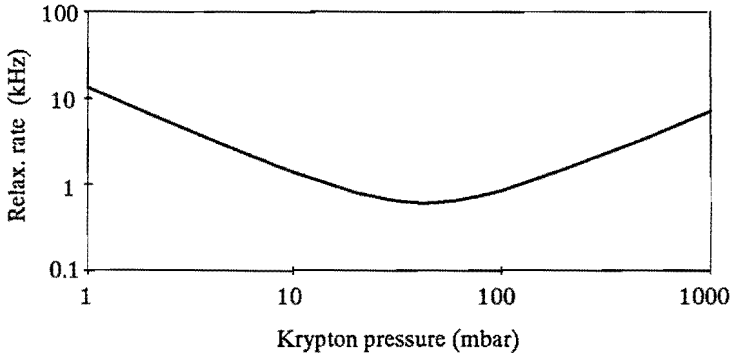

Figure 22 Dicke narrowing of a microwave absorption line

This graph shows the linewidth narrowing that can be obtained by operating a double resonance experiment in a suitable buffergas. The Doppler width is predominant at very low pressures, whereas collision broadening is important at high pressures. In between is a minimum. The minimum exists because the atoms can no longer move freely.

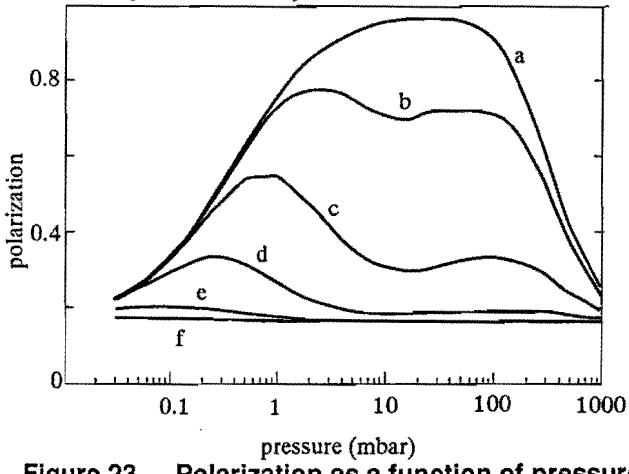

Figure 23 Polarization as a function of pressure

This figure shows the effect of microwave radiation on the polarization P of the hyperfine pumped groundstates at a fixed laser power of 1 mW. The horizontal axis gives the krypton pressure dependence, whereas the parameter is microwave power ranging from 0 mW to 1000 mW in decade steps (a: 0 mW, b: 0.1 mW, c: 1 mW, d: 10 mW, e: 100 mW, f: 1000 mW). The last curve (f) coincides with the thermal polarization (P= 0.167) given by Boltzmann statistics.

$$\frac{d n_1}{dt} = - (B_{14}U + B_{12}u + k_{12})n_1 + (B_{21}u + k_{21})n_2 + A_{31}n_3 + A_{41}n_4, \quad (49)$$

$$\frac{d n_2}{dt} = - (B_{24}U + B_{21}u + k_{21})n_2 + (B_{12}u + k_{12})n_1 + A_{32}n_3 + A_{42}n_4, \quad (50)$$

$$\frac{d n_3}{dt} = k_{43}n_4 - (k_{34} + A_{32} + A_{31})n_3, \quad (51)$$

$$\frac{d n_4}{dt} = B_{14}Un_1 + (B_{24}Un_2 - (A_{41} + A_{42} + k_{43})n_4 + k_{34}n_3. \quad (52)$$

The system allows for the pumping of both ground states through the radiation density U of the laser beam. Diffusion and collisional coupling are incorporated in the k coefficients. This is allowed because of the boundary condition. Spontanous decay is described by the Einstein A coefficients and absorption is described by the Einstein B coefficients. Both quenching and induced decay of the P states can be neglected. By using the familiar relations between the Einstein coefficients it is possible to show that we need to calculate only two of them:

$$B_{14}U = \sigma_0 \, i_L \, \mathrm{Re}\{ w(\omega_L + \imath \, a)\} \quad (53)$$

$$B_{12}u = \frac{1}{3} \frac{i_{RF}}{\Gamma} \frac{\omega_{RF}}{hc}$$

$$\mu_0 \mu_B^2 g_J^2 (2F'+1)^2 \begin{Bmatrix} J & F & I \\ F' & J & 1 \end{Bmatrix}^2 J(J+1)(2J+1) \quad (54)$$

$$\frac{e^{\alpha}}{\beta} \mathrm{Re}\{\alpha - \mu/\beta \, \gamma(\mu/\beta, \alpha)\}$$

where proper use has been made of earlier definitions of the laser and microwave line shape in Eq. 30 and in Eq. 41 respectively. The intensity of the laser and microwave fields have been expressed as i_L and i_{RF} respectively in terms of a photon flux.

In addition, we need an equation for the collisional coupling:

$$k_{12} = \frac{g_1}{\Lambda_{11}^2} D_o \frac{p^o}{p} + \sigma'' \, v_r \, N_o \frac{p}{p^o} \quad (55)$$

where an explanation of the symbols is given in Table 8.

The result of the calculation for the isotope ^{85}Rb only, is presented in Figure 23. The polarization was calculated for a laser beam power of 1 mW and a waist radius as given by Figure 15. Microwave powers are in the range 0.1 mW upto 1000 mW as indicated. It is clear from this figure that the increase

of microwave power has a pronounced effect on the polarization at intermediate pressures. At the low end of the pressure range diffusion prevents too large polarizations . At the high end of the pressure range pressure broadening of the optical transition causes a substantial decrease in the polarization due to the simultanous pumping of both groundstates. Nevertheless even at 1000 mbar there is still a difference between the polarization with and without microwave irradiation. Thus even at 1000 mbar the isotope ^{85}Rb can be detected selectively.

2.6. Concluding remarks

In retrospect we can say that, although OMDRS will probably be able to detect small amounts (10^{14} m^{-3}) rubidium isotopes in krypton gas, the very large reaction rate of rubidium with impurities has prevented experimental verification. Isotope selectivity was clearly demonstrated by the proven large resolving power of OMDRS.
It must be noted that the chemical state of the rubidium isotopes is of no importance at all for the production of gas generators as they are used in medical imaging. Indeed the rubidium-81 isotope is extracted from the target by flushing it with water. For the proposed detection method, however it is essential that the rubidium isotopes are present in their native, metallic and highly reactive, state.

Some of the features of the current experimental set-up are open to improvement:

1 Much higher baking temperatures and hence a cleaner system could be obtained if we were to drop the multi-isotope capability of the current experiment. Higher baking temperatures, however are only possible by removing all PTFE isolated transmission line components. Using an atmospheric microwave horn-antenna instead to irradiate the rubidium atoms would also give the required double resonance signals but over a very restricted frequency range. Thus we would need one horn per isotope to be detected.

2 Lower background signals could be obtained if we were to drop the capability of the present set-up to simulate a decaying proton-induced plasma by running a (pulsed) discharge. The amount of scattering of the laser beam could be reduced drastically then because the beam need not be aligned on the axis of a long, narrow tube.

3 Higher buffergas pressures could be tolerated if we were to bring the rubidium source very close to the observation region. If we were to drop the discharge tube and the microwave transmission line, we could reduce the distance between the observation region and the rubidium source to almost zero resulting in higher rubidium densities even at high buffer gas pressures.

4 A detection efficiency of almost 1 could be obtained if we were to give up optical detection in favour of ion detection. This would require a

second laser to ionize the rubidium isotopes that are resonantly excited by the precisely tuned diode laser. For this purpose an argon laser tuned to the 488 nm line could be used. It would also require a suitable ion detector. A proportional counter might be used, as the pressure range of our experiments is covered by the operating range of proportional counters. In effect this would mean that the OMDRS method would be a variation of *Resonance Ionization Spectroscopy* (RIS) [6] rather than a variation of *Saturated Optical Non-Resonant Emission Spectroscopy* (SONRES) [7].

REFERENCES

[1] N. Bloembergen: *Rev. Mod. Phys.* (1982) **54**, 685 - 696.

[2] A.L. Schawlow: *Rev. Mod. Phys.* (1982) **54**, 697 - 707.

[3] W. Demtroeder: *Laser Spectroscopy*, 2nd(ed.), Springer Verlag, Berlin (1982).

[4] J.D. Winefordner *et al.*: *Trace Analysis Spectroscopic Methods for Elements*, John Wiley, New York (1976).

[5] A.L. Robinson: *Science* (1978) **199**, 1191 - 1193.

[6] G.S. Hurst, M.G. Payne, S.D. Kramer and J.P. Young: *Rev. Mod. Phys.* (1979) **51**, 767 - 819.

[7] J.A. Gelbwachs, C.F. Klein and J.E. Wessel: *Appl. Phys. Lett.* (1977) **30**, 489 - 491.

[8] G.S. Hurst, M.H. Nayfeh and J.P. Young: *Phys. Rev. A* (1977) **15**, 2283 - 2291.

[9] E. Arimondo, M. Inguscio and P. Violino: "Experimental determinations of the hyperfine structure in the alkali atoms," *Rev. Mod. Phys.* (1977) **49**, 31 - 71.

[10] G.P. Barwood, P. Gill and W.R.C. Rowley: "Frequency measurements on optically narrowed Rb-stabilized laser diodes at 780 nm and 795 nm," *Appl. Phys. B* (1991) **53**, 142 - 147.

[11] G. Faure: *The principles of isotope geology*, John Wiley, New York (1977).

[12] J.J.L. Mulders: *Int. J. Appl. Radiat. Isot.* (1984) **35**, 475 - 480.

[13] P. Jacquinot and R. Klapisch: *Rep. Prog. Phys.* (1979) **42**, 774 - 831.

[14] A.A. Radzig and B.M. Smirnov: *Reference data on atoms, ions and molecules*, Springer Verlag, Berlin (1986).

[15] J.J.L. Mulders: "An experimental investigation of proton-induced phenomena in krypton," *Ph.D. Thesis, Eindhoven University of Technology*, Eindhoven, The Netherlands **1985**.

[16] H.T. Duong *et al.*: *J. Physique* (1986) **47**, 1903 - 1908.

[17] E.J.D. Vredenbregt, R.J.F. van Gerwen, W. Boom and H.C.W. Beyerinck: *Rev. Sci. Instr. (to be published).*

[18] M.P.I. Manders: *J. Chem. Phys.* (1988) **89**, 4777 - 4798.

[19] C.E. Wieman and L. Hollberg: "Using diode lasers for atomic physics," *Rev. Sci. Instr.* (1991) **62**, 1 - 20.

[20] T.M. Shay and Y.C. Chang: *Opt. Eng.* (1990) **20**, 681 - 683.

[21] J.J.L. Mulders, P.A.M. Steeman, A.H. Kemper and L.W.G. Steenhuysen: *Opt. Laser Technol.* (1985) **17**, 193 - 196.

[22] H.S. Ue, C.H. Oh, S.H. Yang and N.S. Chang: *Rev. Sci. Instr.* (1990) **61**, 2478 - 2480.

[23] D. Letalick and I. Renkorn: *Rev. Sci. Instr.* (1987) **58**, 765 - 767.

[24] H.C.W. Beyerinck and N.F. Verster: *Vacuum* (1973) **23**, 133.

[25] F.WAelbroeck, J. Winter and P.Wienhold: *J. Vac. Sci. Technol. A* (1984) **2**, 1521 - 1536.

[26] H.F. Dylla: *J. Vac. Sci. Technol. A* (1988) **6**, 1276 - 1287.

[27] A.D. le Grand and E.F. Greene: *J. Vac. Sci. Technol. A* (1983) **1**, 1556 - 1557.

[28] J.H. Voskamp, F.C. van Nijmweegen and A.J. van der Wal: "Data-acquisitie met PHYDAS," *Electronica/Databus* (1988) **23**.

[29] J.H. Voskamp, F.C. van Nijmweegen and A.J. van der Wal: "Besturing van experimenten," *Electronica/Databus* (1988) **24**.

[30] J.H. Voskamp, F.C. van Nijmweegen and A.J. van der Wal: "PHYDAS, een integraal systeem voor data-acquisitie en besturing van fysische experimenten," *Nederlands Tijdschrift voor Natuurkunde A* (1983) **55**.

[31] F.A. Franz: *Phys. Rev.* (1965) **139**, A603 - A611.

[32] R.J. McNeal: *J. Chem. Phys.* (1962) **37**, 2726 - 2727.

[33] R.J. McNeal: *J. Chem. Phys.* (1964) **40**, 1089 - 1098.

[34] J.H. Arnold: "Studies in diffusion: III, unsteady-state vaporization and absorption," *Trans. A.I.Ch.E.* (1944) **40**, 361 - 378.

[35] P.V. Danckwerts: "Absorption by simultaneous diffusion and chemical reaction into particles of various shapes and into falling drops," *Trans. Faraday Soc.* (1951) **47**, 1014 - 1023.

[36] J. Vanier, J.F. Simard and J.S. Boulanger: *Phys. Rev. A* (1974) **9**, 1031 - 1040.

[37] E.R.T. Kerstel: *Chem. Phys.* (1988) **121**, 211 - 235.

[38] A.C.G. Mitchell and M.W. Zemansky: *Resonance radiation and excited atoms*, Cambridge UP, Cambridge (1971).

[39] A.M. van der Spek, J.J.L. Mulders and L.W.G. Steenhuysen: "Vapor pressure of rubidium between 250 and 298 K determined by combined fluorescence and absorption measurements," *J. Opt. Soc. Am. B* (1988) **5**, 1478 - 1483.

[40] B.H. Armstrong: "Spectrum line profiles: The Voigt function," *J. Quant. Spectrosc. Radiat. Transfer* (1967) **7**, 61 - 87.

[41] M. Abramowitz and I.A. Stegun: *Handbook of mathematical functions*, Dover , New York (1970).

[42] W. Gautschi: "Efficient computation of the complex error function," *SIAM J. Numer. Anal.* (1970) **7**, 187 - 198.

[43] W. Gautschi: "Algorithm 363 Complex error function," *Com. ACM* (1969) **12**, 635.

[44] A. Messiah: *Quantum mechanics*, North Holland Physics Publishing, Amsterdam (1986).

[45] R.H. Dicke: *Phys. Rev.*(1956) **123**, 45 - 46.

[46] I.I. Sobelman: *Introduction to the theory of atomic spectra.*Pergamon Press, Oxford (1972).

[47] G.H. Fuller: *J. Phys. Chem. Ref. Data* (1976) **5**, 835 - 1092.

[48] E.R. Cohen and P. Giacomo: "Symbols, units nomenclature and fundamental constants in physics," *Physica A* (1987) **146**, 1 - 68.

[49] N.E. Holden and R.L. Martin: "Atomic weights of the elements 1981," *Pure & Appl. Chem.* (1983) **55**, 1101 - 1118.

[50] E.W. MacDaniel: "Collision Phenomena in Ionized Gases," John Wiley & Sons inc, New York (1964).

AN OPTICAL DETERMINATION OF THE HEAT OF FORMATION OF RUBIDIUM

3.0. Abstract

The heat of formation of rubidium vapour is a thermodynamic key value whose magnitude cannot be inferred from theory alone. The experimental determination of the heat of formation of rubidium is usually done by measuring the vapour pressure of rubidium by the boiling point method. The limitations of this classical approach are explained and an alternative, optical method of measuring vapour pressures is proposed. It will be shown that an optical method based upon laser induced fluorescence is capable of measuring absolute values of the rubidium vapour pressure to high precision. Thanks to the low temperatures at which such measurements must be carried out the resulting data analysis does not use corrections which are obligatory in high temperature boiling point data. The result of our work is an average heat of formation of rubidium vapour at 0 K of 82.3 kJ/mol with a standard deviation of 0.8 kJ/mol. The large standard deviation is due to an unexplained increase of the heat of formation with temperature. Such a trend should not occur according to the third law of thermodynamics. The trend indicates that our thermostat should be redesigned in order to remove temperature and density gradients which were identified as the most probable cause of the observed trend.

3.1. Introduction

Key values for thermodynamics, such as heats of formation, determine the quality and reliability of a whole body of thermodynamic data. For this reason these key values deserve the continuing attention of both reviewers and experimentalists. Indeed, several organisations around the world publish reviews of thermodynamic data in the form of tables purely derived from the recommended key values. Two of the best known are CODATA key values for thermodynamics [1] and JANAF thermochemical tables [2]. Limiting ourselves to the alkali metals, a third reference work is the "Handbook of thermodynamic and transport properties of alkali metals" [3]. (These three will be referred to as CODATA, JANAF and IUPAC). Prime objectives of this work were:

1. To take data points at low temperatures where the rubidium vapour is monatomic and ideal.
2. To prepare the atomic ensemble in a state with exactly known partition function.
3. To prevent the inadvertent reaction of rubidium atoms with buffer gases commonly used in high temperature work.

The method used is a modification of the well known Laser Induced Fluorescence (LIF) technique which allows absolute measurements of very low atomic densities. This method has been applied to sodium as early as

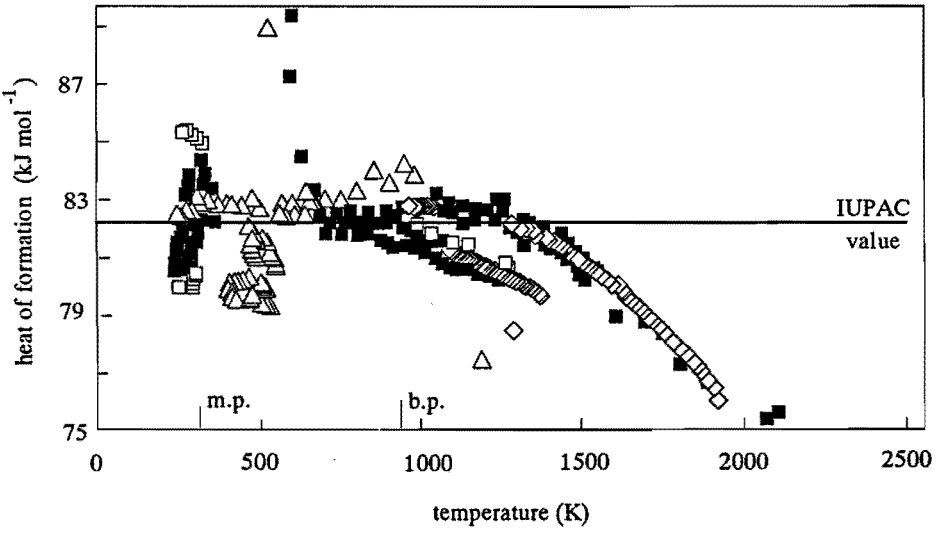

Figure 1 Heat of formation of rubidium

The symbols in this graph refer to individual data points as reported by the original authors. Over 1000 data points, from more than 20 original publications are included in this graph. Lack of different symbols prevents the unambiguous identification of data, instead the graph should be seen as an indication of the degree of scatter and the possible systematic errors in the measured heat of formation of rubidium.

1974 by Fairbank et. al. [4]. In our opinion the three objectives mentioned, when met successfully, mean a significant advantage over the high temperature boiling point data of typically 25 years ago. This is illustrated in Figure 1 where the heat of formation of rubidium vapour has been plotted as a function of temperature. This graph was calculated from a third law evaluation of original data points. Where appropriate a virial correction was applied as has been detailed by Hultgren [5]. This graph immediately shows three flaws: (1); the scarcity of data below the normal boiling point of rubidium, (2); the scatter in the experimental data of several researchers and (3); the general trend with temperature which is forbidden by theory. Even the data selected by CODATA, JANAF and IUPAC show these shortcomings, but no explanation is given for the decreasing trend with temperature of the data. Few of the original researchers have performed a third law evaluation of their data, and of them who did, only Bhise and Bonilla [6] have noted the decreasing trend in their data and attributed it to a slightly too high value for the liquid state heat capacity. This brings up an additional advantage of low temperature data: If the heat of formation of rubidium is calculated from vapour pressure data taken at temperatures below the melting point, no liquid state heat capacities need be used. Contrary to liquid state heat capacities, heat capacities of the crystal rubidium have been measured accurately [7][8][9][10][11]. Moreover crystal heat capacities can be and have been analyzed in terms of the Debye theory [12]. Therefore crystal heat capacities are more reliable than liquid state heat capacities. The more so since the liquid state heat capacities at constant pressure $C_{p,l}$ must be calculated from only 17 data points obtained by Aladyco and Pchelllin [13] in the temperature range 328 - 1038 K; the calculation involves the liquid state density as explained by Fink and Leibowitz [14].

We present new results for the heat of formation of rubidium vapour, using only low temperature data obtained by optical methods. Thereby we circumvent some of the more common difficulties encountered in high temperature (mainly boiling point) experiments. The difficulties of an optical method will be discussed extensively in paragraph 3. Results are presented in paragraph 4, both a third law evaluation and a second law evaluation of the data has been done. We start, however, with a review of some thermodynamics in paragraph 2.

3.2. Thermodynamics

Naturally abundant rubidium consists of two isotopes, ^{85}Rb and ^{87}Rb. The isotopic composition of naturally abundant rubidium is taken as the recommended value from the 1981 IUPAC review [15]. Individual isotope masses have been taken from the 1983 atomic mass evaluation [16]. Both the isotopic composition and the individual isotope masses enter the calculation of the heat of vaporization of rubidium from measured vapour pressures. The calculation is not new and has been done by a number of (textbook) authors [17]. Therefore no details shall be given here. For a

Table 1 Heat capacities and Gibbs energy functions for rubidium below the melting temperature

T [K]	C_p [Jmol^{-1}K^{-1}]	$-\frac{G^o-H^o(0)}{T}$ [Jmol^{-1}K^{-1}] a)	T [K]	C_p [Jmol^{-1}K^{-1}]	$-\frac{G^o-H^o(0)}{T}$ [Jmol^{-1}K^{-1}] a)	CODATA value [1] [Jmol^{-1}K^{-1}]
5	1.570	0.156 (0.001)	140	26.38	33.795	
10	6.910	0.879 (0.05)	150	26.59	35.304	
15	12.18	2.218 (0.01)	160	26.84	36.736	
20	16.24	3.990	170	26.95	38.098	
25	18.79	5.756	180	27.13	39.396	
30	20.51	7.619	190	27.48	40.638	
35	21.58	9.413 (0.003)	200	27.52	41.828	41.952
40	22.40	11.152	210	27.67	42.970	
45	22.91	12.814	220	27.84	44.067	
50	22.37	14.399	230	28.13	45.125	
55	23.80	15.901	240	28.38	46.146	
60	24.12	17.329	250	28.74	47.132	
70	24.59	20.013	260	29.06	48.086	
80	24.98	22.421	270	29.45	49.011	
90	25.37	24.686	280	29.88	49.909	
100	25.55	26.759	290	30.39	50.782	
110	25.70	28.696	300	32.75	51.632	51.817
120	25.91	30.502				
130	26.13	32.198	298.15	30.89	51.476	51.662

a) The value between brackets is the rounding error given by the algorithm of Gill and Miller.

crystalline solid mixture of rubidium in its natural abundant composition the (differential) Gibbs free energy function is:

$$-\left[\frac{G^o - H^o(T_r)}{T}\right]_{cr} = \int_0^T \frac{C_p(t)}{t}\,dt - \frac{1}{T}\int_0^T C_p(t)\,dt$$

$$+\frac{H^o(T_r) - H^o(0)}{T} + S(0) + R\sum_i x_i \ln x_i \qquad (1)$$

In this formula (and in all other formulas) we adhere to IUPAP recommendations regarding notation [18]. The last term is the Gibbs mixing energy (x_i = 0.27835, the relative abundance of ^{87}Rb [15]). Common reference temperatures T_r are 0 K and 298.15 K (25 ^{o}C). Apart from the mixing energy and the entropy constant S(0), this function has been tabulated extensively by CODATA, IUPAC and JANAF. Since we are primarily interested in temperatures below the melting point of rubidium these tables hardly suffice: only 4 or 5 entries are listed at temperatures below 312.47 K (= the melting temperature). Therefore we have constructed our own table using only the first three terms of Eq. 1. As is well known both the entropy constant and the mixing energy are not important as they are common terms in the solid phase and vapour phase formulas. The result of our calculation is given in Table 1. We have used the aforementioned heat capacity measurements [7][8][9][10][11][12], placing equal weights on every data point, but disregarding the older data of Dauphinee, Martin and Preston-Thomas [9] and of McCollum and Silsbee [11], which are believed to be unreliable [8]. The integration of the (unequally spaced) heat capacity data was done with an algorithm published by Gill and Miller [19]. Given the differences in the heat capacities between our table and e.g. the CODATA table the agreement is satisfactory. Whenever necessary we have used the international table calorie (= 4.1868 J) to convert data quoted in calories to Joules, and we used an atomic weight of rubidium of 85.48 equal to the value of Filby and Martin [8], but in disagreement with the recommended value 85.4678 [20] presently in use.

In the case of rubidium the entropy constant can be written as a weighted average over nuclear spin degrees of freedom:

$$S^o(0) = \sum_i x_i \ln(2I_i + 1) \qquad (2)$$

where I_i is the isotope's nuclear spin (I = 5/2 for ^{85}Rb; I = 3/2 for ^{87}Rb). All other possible contributions to the entropy constant are explicitly neglected.

The vapour phase Gibbs free energy function can be calculated from

statistical mechanics. We need not bother about the presence of other species since our measurement will prove to be insensitive to them. Therefore we calculate the Gibbs function for a mixture of (monatomic) ^{85}Rb and ^{87}Rb in the gas phase at pressure p^o:

$$-\left[\frac{G^o-H^o(T_r)}{T}\right]_{vap} = S^o - \frac{5}{2}R\left[1+\frac{T_r}{T}+\ln\frac{T}{T_1}\right]$$

$$+ R\sum_i\left[\frac{3}{2}x_i\ln A_i - x_i\ln x_i + x_i\ln Q_i\right] - RT\ln\frac{p}{p^o} \qquad (3)$$

Here x_i denotes the relative abundance of each isotope i, A_i is the relative atomic weight, $T_1 = 1$ K, $p^o = 100$ kPa and S^o is the Sackur-Tetrode (absolute entropy) constant ($S^o/R = -1.151693$ for $p^o = 100$ kPa) [18]. The electronic contribution to the Gibbs function is $\ln Q_i$ with:

$$Q_i = (2F_i + 1) + (2F'_i + 1)\, e^{-\Delta E/kT} \qquad (4)$$

Here ΔE is the groundstate hyperfine splitting (3035 MHz for ^{85}Rb, 6894 MHz for ^{87}Rb) which is negligible at temperatures above 100 K. The exponential, therefore, is equal to 1 and Eq. 4 simplifies to:

$$Q_i = \sum_{F_i}(2F_i + 1) = (2I_i + 1)\,(2J + 1) \qquad (5)$$

This simplification is a consequence of the Russell-Saunders coupling scheme for the nuclear- and electronic spin ($F_i = I_i + J$, where I_i is the nuclear spin of isotope i, J is the electronic spin and F_i is the total (atomic) spin [21]).

The heat of vaporization of crystalline rubidium, or equivalently the heat of formation of monatomic rubidium vapour at pressure p, $\Delta_f H^o$, is:

$$\Delta_f H^o(Rb,cr,T_r) = H^o(Rb,vap,T_r) - H^o(Rb,cr,T_r)$$

$$= -T\Delta\left[\frac{G^o - H^o(T_r)}{T}\right] - RT\ln\frac{p}{p^o} \qquad (6)$$

where Δ signifies vapour minus crystalline Gibbs energy functions. This relation can be understood by considering the isobaric and isothermal vaporization at p^o followed by an isothermal (de)compression of the crystal and the vapour to pressure p. The contribution to $\Delta_f H^o$ from the expansion of the crystal ($= -V_{crystal}\,(p^o - p)$) has been neglected in Eq. 6. It is clear from

Eq. 1, Eq. 3 and Eq. 6 that both the Gibbs mixing energy and the nuclear degrees of freedom cancel since these terms are common to both the vapour phase and the crystalline phase. Only at temperatures below 100 K the nuclear degrees of freedom must be retained, since at these temperatures the simplification Eq. 5 no longer holds. Equation 6 allows one to plot the vaporization heat versus temperature for each data point taken. The result should not depend on temperature; a test known as the third law test since absolute entropies need be known to evaluate Eq. 6. Usually [17] the isotopic composition is neglected completely by writing:

$$\frac{3}{2} R \sum_i x_i \ln A_i = \frac{3}{2} R \ln\left(\sum x_i A_i \right) = \frac{3}{2} R \ln A_{Rb} \qquad (7)$$

Our method of measurement, however is sensitive to the partial pressure of one isotope only, and we are free in our choice: either ^{85}Rb or ^{87}Rb. Usually the pressure is calculated from the data by inserting the known relative abundance [15]. Alternatively, we may calculate the relative abundances by assuming that the heat of sublimation of rubidium is a weighted average of the sublimation heats of the isotopes:

$$\Delta_f H^o(Rb,cr,T_r) = x\, \Delta_f H^o(^{87}Rb,cr,T_r) + (1 - x)\, \Delta_f H^o(^{85}Rb,cr,T_r) \quad (8)$$

This assumption is mathematically in accordance with the approximation in Eq. 7 and is in accordance with Kopp's law for the additivity of crystal heat capacities.

3.3. Method of measurement

Absolute values of the density of a uniform amount of matter can be calculated from Beer's law when the absorption cross section and length is known and when then absorption can be measured. The use of Beer's law, however, is restricted to those cases where the absorption is measurable but not too large. In 1974 Fairbank, Hänsch and Schawlow (4) used an elegant extension of Beer's law to obtain absolute values of sodium densities in regions otherwise inaccessible. When a laser beam is tuned to an atomic transition with absorption cross section σ and the beam is attenuated over an absorption length L, the measured fluorescence as a function of density (or temperature) from a small observation length l has a maximum at an unique value of the density. The measured fluorescence signal I relative to the photon flux of the beam is:

$$\frac{I}{I_0} = \varepsilon\eta\frac{\Omega}{4\pi} e^{-\sigma N L}(1 - e^{-\sigma N l}) \qquad (9)$$

where ε is the transmission of the optical system, η is the quantum efficiency of the photo multiplier and Ω is the solid acceptance angle of the optics. By

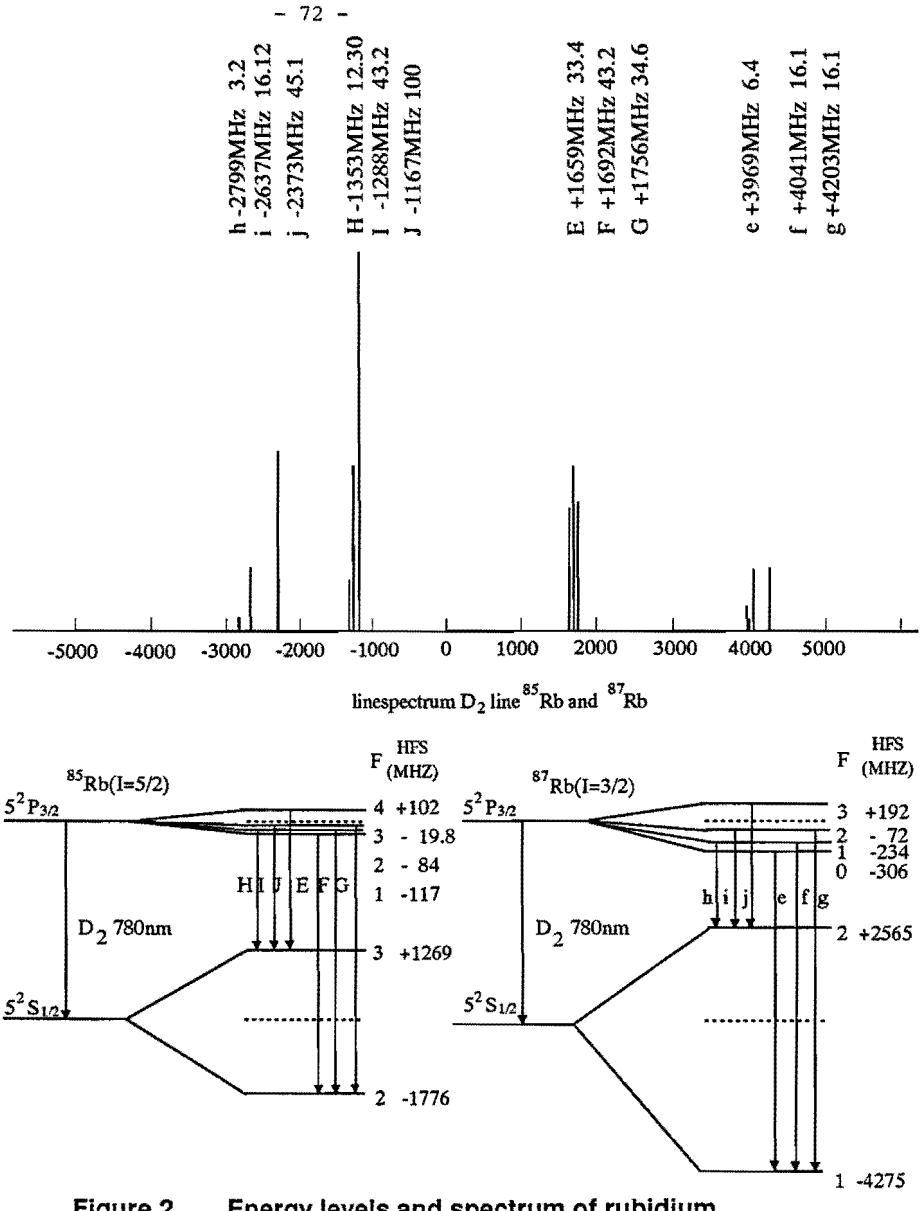

Figure 2 Energy levels and spectrum of rubidium

The energy level diagrams of this figure contain all the allowed transitions. These are given a letter identification corresponding to the letter identification in the upper line spectrum. Only the D_2 line is shown. Of particular importance is the 'EFG' group of lines in this figure, since this group is used for the determination of vapour pressures as is described in the main text. In addition to the line identification, hyperfine quantum numbers, energy level splittings and relative line strengths are given.

differentiating Eq. 9 with respect to the temperature, the maximum is found to be:

$$N_{max} = \frac{1}{\sigma l} \ln(1 + \frac{l}{L}) \qquad (10)$$

Note that this value does not depend on any parameters of the experiment other than the absorption length L and the observation length l. The value N_{max} is thus an absolute value which can be used to calibrate the experiment. Hence at densities where an absorption measurement is no longer possible, the fluorescence can be monitored and it can be related to the absolute value Eq. 10. The peak fluorescence to photon flux ratio:

$$\left[\frac{I}{I_0}\right]_{max} = \varepsilon\eta\frac{\Omega}{4\pi}\left[\frac{L}{l+L}\right]^{L/l}\frac{l}{l+L} \qquad (11)$$

in contrast does not depend on any parameters of the atomic system under observation. Thus the value $(I/I_0)_{max}$ is an apparatus constant which can be maximized independently.

3.3.1. *Calculation of the cross section*

The photon cross section can be calculated as a function of wavelength and temperature. This is shown in an other paper [22] and we do not want to repeat it here. Instead we shall use a much simpler approach based upon a simple integral relationship.

Consider a group of isolated but unresolved lines all originating from the same groundstate like the 'EFG' group in Figure 2. These lines belong to the ^{85}Rb atom and originate from the lower groundstate. The hyperfine splitting of the upper level is masked by the Doppler broadening. Thus in ordinary Doppler-limited spectroscopy the three lines appear as one single peak. The area under the peak is constant, independent of the peak shape and given by:

$$\int_0^\infty \sigma F_i(\nu)\, d\nu = \frac{1}{8\pi}\frac{2J'+1}{2J+1}\lambda_0^2\frac{2F_i+1}{(2I_i+1)(2J+1)}\frac{x_i}{\tau} \qquad (12)$$

This formula is a simple extension from the more common formula given by e.g. Mitchell and Zemansky [23]. In Eq. 12 J and J' are the groundstate and excited state total spin quantum number, λ_0 is the line centre wavelength, F_i is the hyperfine quantum number, I_i is the nuclear spin, x_i the relative abundance of isotope i and τ the excited state lifetime. The expression given in Eq. 12 can simply be summed over all possible values of F_i by invoking the sum rule in Eq. 4 and Eq. 5. A further summation over i will then give the classical formula for the integrated photon cross-section.

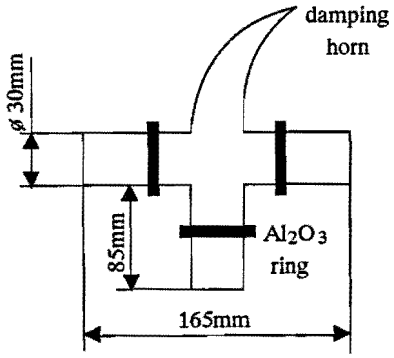

Figure 3 Geometry of fluorescence cell

This top view of the fluorescence cell shows its main features. The cell is made of 4 mm thick DURAN glass. Aluminium oxide rings are used in each leg of the cell to break the light (leak) guide from entrance window to observation window through the wall of the cell. The damping horn provides a 'dark' background for the photomultiplier. The entrance-, exit- and observation window are made of standard quality flat glass set to right angles with the axis of the cell. The use of optically flat windows glued to the cell body was prevented by the necessary baking. Also the glue was known to react with high temperature rubidium vapour.

Table 2 Absorption and observation lengths

Quantity	Symbol	Value	Unit
Photocathode diameter	d	1	mm
Magnification	M	0.25	
Absorption length	L	183	mm
Observation length	l	4	mm

Absorption and fluorescence lines are very nearly gaussian when observed with a narrow bandwidth laser, the full width at half maximum being the Doppler width:

$$\Delta\nu_D = \lambda_0^{-1}\sqrt{\frac{8RT}{M_i}\ln 2} \qquad (13)$$

By integration of a gaussian peakshape with a width (FWHM) given by Eq. 13 we find for the peak value $\sigma_0(\nu_0)$:

$$\sigma F_i(\nu_0) = \frac{1}{8\pi}\sqrt{\frac{M_i}{2\pi RT}}\lambda_0^3\frac{2F+1}{(2I_i+1)(2J+1)}\frac{2J'+1}{2J+1}\frac{x_i}{\tau} \qquad (14)$$

Again the correction for the relative abundance and for the distribution of atoms over their groundstates is found. Of course Eq. 14 is only approximately true because the hyperfine shifts for the unresolved lines are not exactly the same. The differences between pairs of hyperfine shifts, however, are very small when compared to the Doppler width. Thus Eq. 14 is a very good approximation.

3.4. Experimental

The experiment itself is conceptually very simple, it involves only a series of measurements of the beam intensity and of the fluorescence as a function of cell temperature. In order to obtain high accuracies, however, several points become critical e.g. the cell temperature, the laser's frequency stability; statistical errors in counting low level fluorescence and the inadvertent possibility of non-equilibrium conditions. These points will be discussed in detail.

3.4.1. Calculation of the lengths l and L

The absorption length L may be calculated from the fluorescence cell geometry in Figure 3. The observation length l follows from the demagnification of the collection lens and from the diameter of the photocathode of the photomultiplier. The results are given in Table 2.

3.4.2. Temperature measurement and control

The fluorescence cell of Figure 3 is made of glass (DURAN 8330), evacuated and baked at 400 C for 24 hours before about 1 g of rubidium is distilled into it. The cell is then sealed off and ready for use. In a first series of experiments the cell was painted black and installed in the cryostat. In a second series we sought to saturate the glass wall with rubidium by repeatedly heating the cell to 100 C and let it cool. Next the cell was wrapped in braided copperwire leaving only the entrance, exit and fluorescence windows open. The copperwire was connected to the heat sink of the cryostat. See Figure 4 for details.

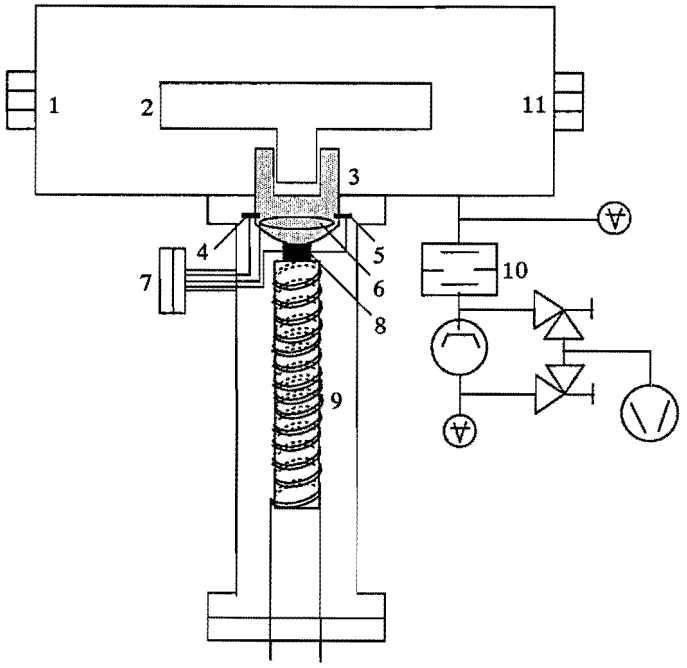

Figure 4 Experimental set-up

This side view shows the large vacuum housing used for mounting the fluorescence cell (not shown) and its associated heat shield and thermo-statted oil bath. The pumping system and vacuum meters have been added schematically. The photomultiplier, the collection lens and the long pass RG 9 filter are inserted in the large vacuum housing sideways where the vacuum seal is made on the lens using 'O'-rings. Main elements are numbered as follows: 1; Entrance window. 2; Heat shield. 3; Main oil-bath. 4; K-type thermocouple used for temperature control. 5; Platinum resistor (Pt-100) used for temperature measurement. 6; Thermocoax heating wire soldered in copper oil-bath. 7; Electrical feedthrough carrying flange. 8; Heat resistance. 9; Cooled copper bar. 10; Pumping system consists of LN_2 baffled diffusion pump and a mechanical two stage roughing pump. 11; Exit window for laser beam.

The temperature of the heatsink was measured with a class B platinum resistance thermometer operated under the conditions where an absolute accuracy (repeatability) of 0.3 K is guaranteed (DIN 43760; IEC 751). The temperature stability of the cryostat, however, was much better: we estimated a stability of 0.04 K based upon recorded error voltages from the temperature controller. This controller uses a K type thermocouple to sense the heatsink temperature and it will raise or lower the current in a thermocoax heating wire as required. The heatsink is cooled by either liquid nitrogen or by a mixture of 60% water and 40% 1,2 ethane-diol flowing through a tube. The heatsink is enclosed in an evacuated chamber which is pumped down to 10^{-6} mbar.

3.4.3. Laser system

A versatile laser system has been developed, details of which are given in an internal report. Thus only the laser's frequency stabilisation will be discussed here, while the other parts are described briefly. A cheap and easy to use diode laser (SHARP LT022) forms the heart of our laser system, see Figure 5 for the mode chart of this diode laser. It is mounted in a copper heatsink and temperature regulated to within 1 mK, which is not enough to eliminate temperature drifts (30 MHz/mK). At a temperature of 8 ^{o}C and an injection current of 80 mA single mode operation at a wavelength of 780027 pm is then obtained. The laser emits about 4 mW of optical power at this temperature and injection current. Part of the laser beam is split-off and guided through an absorption cell. The absorption cell is similar in design to the fluorescence cell, but it is always at room temperature. The absorption cell is used to lock the laser frequency to the centre of an absorption peak. In the first series of experiments this was done by direct modulation of the injection current with a sinusoidal signal. The resulting frequency changes were 'detected' by the rubidium atoms in the absorption cell. A large-area silicon photodiode (BPW34) converted the optical signal to an electrical signal which was filtered and amplified by a synchronous amplifier (Brookdeal 9503SC). The output of this lock-in amplifier could be inverted easily and this inverted signal was used to drive a PI controller. The controller in turn regulated the injection current and thereby the laser's frequency (3 GHz/mA). This type of feedback offers excellent stability and the small offset from the exact peak location resulting from the simultaneous power modulation(0,25 mW/mA) is negligible.

However, direct modulation is not very flexible. Specifically, scattered laser photons cannot be discriminated from fluorescence photons. Were this background constant this would not present a difficulty but since the background signal depends upon the laser beam power, which is altered by the frequency stabilisation loop, the background is not constant. Therefore, in the second series of experiments, the laser frequency was brought under computer control. This enabled us to measure the background on both sides of the absorption peak for each data point (fluorescence vs. cell temperature) taken. The mean background signal was then subtracted from the fluorescence cell. Since the top of our Doppler broadened absorption line is

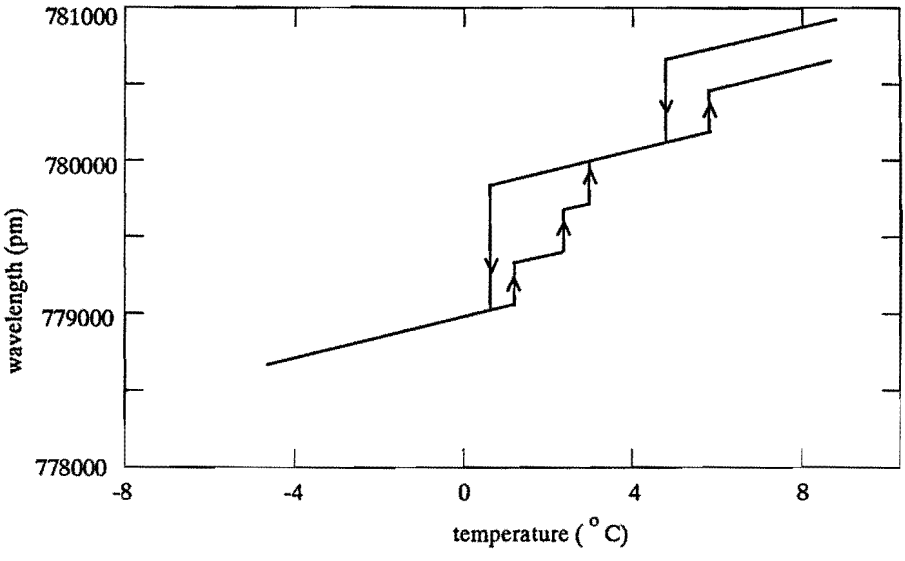

Figure 5 Mode chart of diode laser

Shown are the main cavity modes of the diode laser and their hysteresis loops. This graph consists of over 1600 individual measurements made using a 'wavemeter', with a resolution of 1 pm. The graph does not show all possible modes of this particular laser; a mode hop usually occurs during the unavoidable overshoot when the temperature of the diode laser is changed. In taking data for this graph we used the smallest possible temperature change allowed by our controller. Nevertheless two mode hops larger than 0.3 nm (the cavity mode spacing) and two 'blind' areas can be seen in this mode chart.

comparatively flat, the laser's frequency stability is not critical. More specifically, the peak cross section Eq. 14 is constant to within 1 or 2% over the 50 MHz bandwidth of the laser. The absolute frequency stability (drift) of the laser is of the same order of magnitude as the bandwidth as may be inferred from Figure 6.

These histograms give the number of times that a certain correction of say 50 MHz was necessary to retune the laser frequency to the top of the absorption peak.

3.4.4. Thermodynamic equilibrium and statistics of low level fluorescence

Even if thermal equilibrium of the heat sink could be established with certainty this would not imply the thermodynamic equilibrium of the rubidium vapour with its solid crystalline state. Worse still, there is no direct experimental evidence available about the thermodynamic equilibrium which the heat-sink, fluorescence cell and rubidium solid plus vapour should have attained at a certain instant. Therefore thermodynamic "equilibrium" is said to have been attained when the fluorescence signal from the cell divided by the photon flux becomes constant. This ratio is measured by a pair of scalers gated by a common time base. The scalers are interfaced through a PHYBUS to the measurement computer. The computer is programmed to average the measured ratios and to test the equalness of the means and variances by standard t- and F-tests [24]. The level of significance of the tests is usually 5%, and the sample taken is usually 120 ratios. Whenever the t- and F-test are passed, final sampling is started and the final average is calculated from a series of 10 samples each usually 120 ratios large. In addition the distribution function of the ratios taken is calculated by binning the data. With a sample of 120 ratios the chosen number of bins (70) is far from optimal but it still suffices to test whether the distribution is normal or not. This is tested using a χ^2 test on all 70 bins and on the complete series of samples. The level of significance of the χ^2 test is usually set to 50%. Figure 7 shows an example of a distribution obtained in measuring resonance fluorescence. This distribution is close to normal, others show large drifts with respect to the moment when the t- and F-test were simultaneously satisfied. This moment (and the mean and variance at this moment) is taken as a reference point for the χ^2 test. Hence after a complete series of measurements has been obtained it is possible to decide whether the data can be accepted or not, specifically it is possible to reject the t- and F-test in retrospect. Since these tests are not distribution free, i.e. they are only valid for data that are distributed normally, such a retrospect test of the normality of the data is obligatory.

We feel that the procedure outlined above reasonably assures the soundness of the data. Only one indeterminacy remains namely the delay time between subsequent t- and F-tests. If this time is too short compared to the relaxation

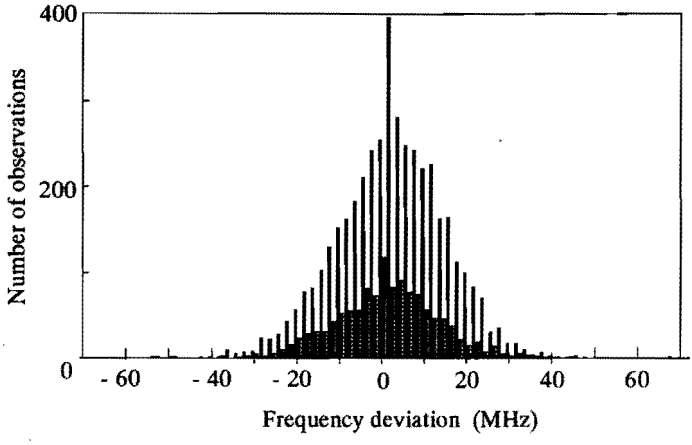

Figure 6 Histogram of frequency deviations for the diode laser

The histogram illustrates the absolute frequency stability of an essentially free running diode laser. Two experiments were run overnight where the laser's injection current was readjusted every minute to retune the frequency to the top of an absorption line in rubidium. The necessary correction was listed, binned in 2 MHz wide bins and serves as a measure of the free-running drift.

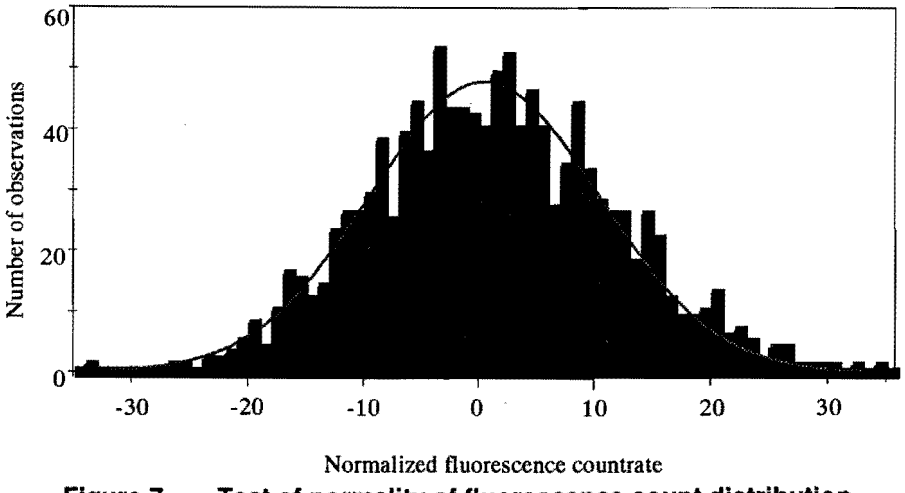

Figure 7 Test of normality of fluorescence count distribution

In this graph the fluorescence counts taken from the photon counter were treated as being distributed normal with mean m and standard deviation σ. Their distribution N(μ,σ) was then mapped on a standard normal distribution with zero mean (μ = 0) and standard deviation 10 (σ = 10). After mapping, the distribution is binned in 70 bins. The result is that the outermost bins in this graph correspond with the 3.5 σ boundaries of the original distribution.

time of the heat sink and fluorescence cell, large drifts during the sampling stage are certain to occur. Therefore we tentatively chose a delay time of 1 minute which is roughly 10% of the thermal relaxation time constant. The final data assessment must still await a third law analysis as has been detailed in section 3.1.

3.5. Results

Results from the first series of three experimental runs with liquid nitrogen cooling of the cryostat and lock-in locking of the laser frequency are presented in Table 4 and in Figure 8 and in Figure 9. It is clear from Figure 9 that the calculated heat of formation $\Delta_f H^o$(Rb,cr,0 K) is not independent of temperature revealing some systematic error unaccounted for. The large difference in third law and second law (Clausius-Clapeyron) heats of formation as shown in Table 3 is also evidence of systematic errors. The cause of this error is not entirely clear. In this respect it is instructive to compare the present results with results obtained in an earlier experiment [22]. These results have been plotted as triangles in Figures 8 and 9. Both method and set-up were comparable to the present method and set-up, but because of the use of the D_1 line and because of the somewhat more limited temperature range of the cryostat no absolute densities could be calculated by application of Eq. 10. A single absorption measurement was used instead. The inaccuracy of this single absolute measurement is reflected in a heat of formation that is too low, consistent with the expected direction of error. Too much absorption has apparently been ascribed to the rubidium atoms in the absorption cell hence too high a vapour pressure was calculated from this measurement.

The present set-up was modified to account for this shortcoming and indeed absolute densities could be inferred through the use of Eq. 10. This apparently resulted in an average heat of formation in-line with the recommended value as is evident from Table 3. The calculated heat of formation, however, does show a clear increasing trend with temperature, which is reflected in a relatively large standard deviation in the calculated average heat of formation. Note that this trend cannot be explained by a temperature gradient between fluorescence cell and temperature sensor. If such a gradient were present during heating or cooling and subsequent sequential data gathering, the temperature of the fluorescence maximum would be recorded as either too low or too high, resulting in vapour pressures being too high or too low respectively. Apparently this is not the case, since at the temperature where the fluorescence peaks, according to Eq. 10, (19.3 ^oC) the calculated heat of formation equals 82.3 kJ/mol. While it is true that the exact position of the maximum is difficult to determine, we feel that temperature gradients alone cannot explain the observed trend with temperature that is visible in Figure 9. Temperature gradients may have played a role in the wings of the fluorescence-temperature curve where the sensitivity to temperature errors increases. In the wings of the fluorescence -

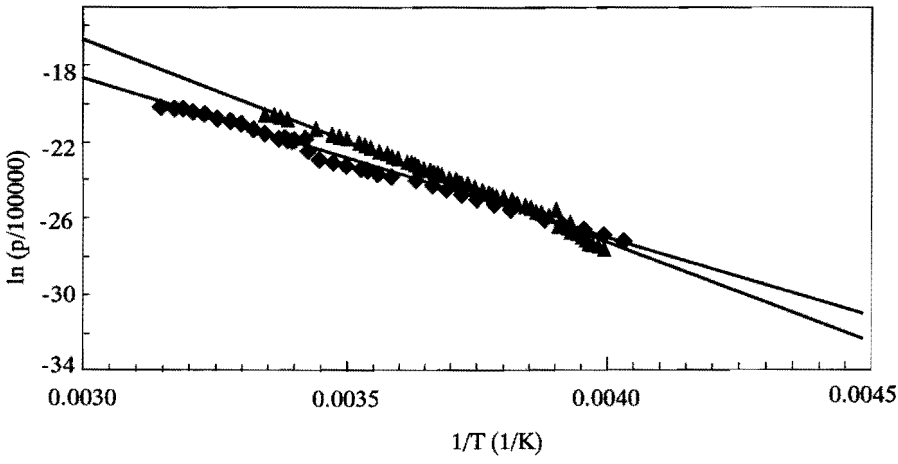

Figure 8 Clapeyron plot of rubidium vapour pressure

According to the Clausius - Clapeyron equation, the logarithm of the vapour pressure plotted against the inverse of temperature should give a straight line provided that the heat of formation can be considered to be constant. This graph shows to what extent the data gathered in this article (diamonds) and the data form an earlier experiment (triangles) conform to the Clausius - Clapeyron theory. The straight lines in this graph are the best fit to the data using the least-squares criterion. The slope of these lines yields the so-called second law heat of formation listed in Table 3.

temperature curve, if there were a lag between measured temperature and equilibrium temperature due to density gradients in the fluorescence cell, the measured data points would reveal densities that are too high on the low temperature side of the maximum and densities that are too low on the high temperature side of the maximum. This then would be consistent with the observed trend with temperature in Figure 9. It is possible to reduce the slope of the trend line through the scattered experimental points in Figure 9 to within experimental error by correcting the measured temperature of an experimental run by less than 10% with respect to the temperature where maximum fluorescence occurs. Such a correction, however is regarded to be of no value at all since it would be lacking a physical explanation and be driven entirely by the known and wanted result.

It is not clear what possibly can be the cause of such a lag or density gradient. In constructing the fluorescence cell and in subsequent handling care was taken to at least cover the interior of the glass cell with a very thin layer of rubidium. Also in the attached reservoir the bulk of the rubidium is kept at the measured temperature so that this reservoir acts as buffer to replenish adsorbed rubidium atoms. Also, wrapping the entire cell in braided copper wire ensures that the glass envelope will closely follow the temperature of the thermo-statted heat sink. Except for the windows there should therefore be no cold (or hot) spots.

In view of the results it is concluded that the thermal behaviour of our set-up is most important. Therefore the following recommendations can be listed:

1 The observation length l should be made as short as possible. According to Eq. 10 this will increase the temperature where maximum fluorescence occurs. Thermal relaxation times can then be shortened by installing more heating power in order to prevent clipping.

2 The use of vacuum as insulating material must be discouraged. Although vacuum does help with respect to reducing the power consumption of the thermo-stat, its effect is actually detrimental. Unwanted temperature gradients can build up much more easily in glass cells encapsulated in vacuum. If the measurement range is shifted to higher temperatures the need for efficiency with respect to power consumption becomes less important because heating power is much more readily available than cooling power.

3 Temperatures must be measured on the glass envelope of the cell itself. Several measurement points must be selected in order to allow for an assessment of possible temperature gradients.

To summarize the results of this work, we note the following; Although the three conditions listed in the introduction have been met, this has not lead to an improved or more reliable determination of the heat of formation of rubidium vapour. In designing the experimental equipment the importance of temperature measurement and the exclusion of temperature gradients and

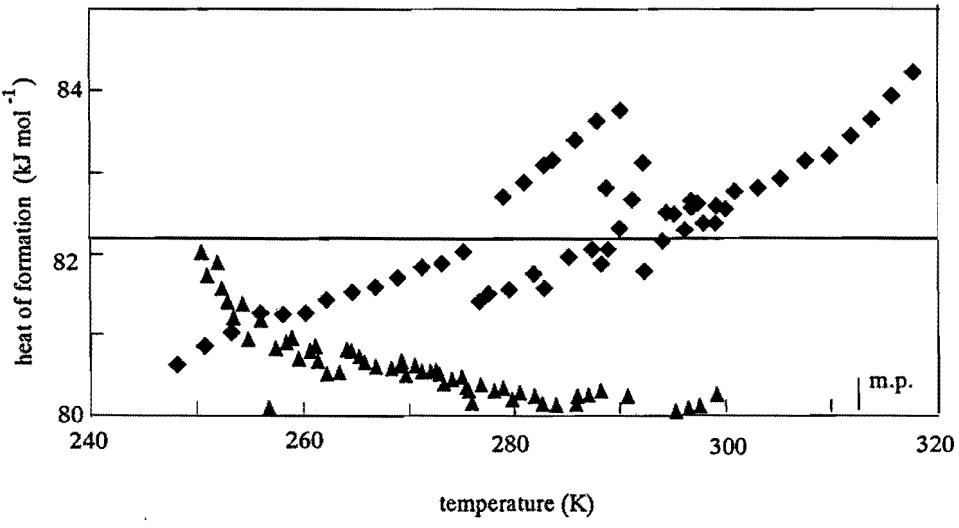

Figure 9 Measured heat of formation of rubidium versus temperature

This figure is essentially an enlarged version of Figure 1. Here only the results of this experiment (diamonds) and that of an earlier experiment (triangles) [22] have been plotted. The trend with temperature in both data sets should not occur according to theory, it is indicative of a systematic error. Note that the data from [22] were corrected to account for the double counting of the nuclear spin degrees of freedom.

Table 3 Summary of experimental results

Source	Heat of formation [kJ mol^{-1}] 3rd law analysis $\Delta_f H^o$(Rb, cr, 0 K)	Heat of formation [kJ mol^{-1}] 2nd law analysis $\Delta_f H^o$(Rb, cr, 0 K)	Reference
This work	82.331 (0.823)	69.423	
Van der Spek et.al.	80.653 (0.493)	87.499	[22]
CODATA	82.2 (0.8)	n.a.	[1]
IUPAC	82.192	n.a.	[3]
JANAF	82.2 (0.4)	n.a.	[2]
Hultgren	82.225 (0.209)	n.a.	[5]

associated density gradients was underestimated. The average heat of formation found (82.3 kJ/mol) is in accordance with other experimental results as is shown in Table 3. The standard deviation of the average (0.8 kJ/mol), however is much too large due to an unexplained trend in the experimental data.

Table 4 Measured density, vapour pressure and heat of formation of rubidium vapour

Temperature [K]	Density [m^{-3}]	Vapour pressure [Pa]	Heat of formation [J mol^{-1}]
248.01	4.28 10^{+13}	1.47 10^{-7}	80630
250.47	5.54 10^{+13}	1.92 10^{-7}	80863
252.84	7.29 10^{+13}	2.54 10^{-7}	81023
255.51	9.75 10^{+13}	3.44 10^{-7}	81230
257.85	1.35 10^{+14}	4.80 10^{-7}	81248
259.93	1.77 10^{+14}	6.35 10^{-7}	81292
262.09	2.25 10^{+14}	8.14 10^{-7}	81420
264.31	2.89 10^{+14}	1.05 10^{-6}	81533
266.52	3.77 10^{+14}	1.39 10^{-6}	81598
268.73	4.81 10^{+14}	1.78 10^{-6}	81703
271.03	6.09 10^{+14}	2.28 10^{-6}	81843
273.00	7.70 10^{+14}	2.90 10^{-6}	81882
275.21	9.57 10^{+14}	3.64 10^{-6}	82020
276.60	1.48 10^{+15}	5.67 10^{-6}	81407
277.34	1.58 10^{+15}	6.03 10^{-6}	81478
278.90	1.13 10^{+15}	4.36 10^{-6}	82681
279.48	1.98 10^{+15}	7.62 10^{-6}	81555
280.90	1.33 10^{+15}	5.17 10^{-6}	82871
281.69	2.37 10^{+15}	9.23 10^{-6}	81743
282.69	1.51 10^{+15}	5.91 10^{-6}	83077
282.90	2.95 10^{+15}	1.15 10^{-5}	81567
283.75	1.68 10^{+15}	6.58 10^{-6}	83131
285.20	3.28 10^{+15}	1.29 10^{-5}	81951

285.80	1.92 10^{+15}	7.57 10^{-6}	83389
287.30	4.01 10^{+15}	1.59 10^{-5}	82048
288.02	2.24 10^{+15}	8.90 10^{-6}	83639
288.30	4.86 10^{+15}	1.93 10^{-5}	81860
288.90	4.83 10^{+15}	1.93 10^{-5}	82038
288.90	3.56 10^{+15}	1.42 10^{-5}	82771
289.93	4.86 10^{+15}	1.95 10^{-5}	82302
290.08	2.71 10^{+15}	1.09 10^{-5}	83749
291.13	4.72 10^{+15}	1.90 10^{-5}	82659
292.11	4.33 10^{+15}	1.75 10^{-5}	83101
292.31	7.68 10^{+15}	3.10 10^{-5}	81754
294.04	7.76 10^{+15}	3.15 10^{-5}	82129
294.60	7.10 10^{+15}	2.89 10^{-5}	82477
295.16	7.47 10^{+15}	3.04 10^{-5}	82481
296.10	8.89 10^{+15}	3.63 10^{-5}	82270
296.85	8.31 10^{+15}	3.40 10^{-5}	82609
296.90	8.57 10^{+15}	3.51 10^{-5}	82541
297.30	8.74 10^{+15}	3.59 10^{-5}	82587
298.04	1.04 10^{+16}	4.28 10^{-5}	82326
298.80	1.10 10^{+16}	4.54 10^{-5}	82358
299.09	1.04 10^{+16}	4.29 10^{-5}	82563
300.06	1.34 10^{+16}	5.55 10^{-5}	82518
300.90	1.33 10^{+16}	5.52 10^{-5}	82755
303.20	1.66 10^{+16}	6.95 10^{-5}	82793
305.20	1.95 10^{+16}	8.21 10^{-5}	82900
307.50	2.26 10^{+16}	9.59 10^{-5}	83111
309.70	2.73 10^{+16}	1.11 10^{-4}	83183
311.80	3.06 10^{+16}	1,32 10^{-4}	83417
313.70	3.34 10^{+16}	1.45 10^{-4}	83646
315.70	3.64 10^{+16}	1.59 10^{-4}	83921
317.60	3.90 10^{+16}	1.71 10^{-4}	84213

REFERENCES

[1] J.D. Cox, D.D. Wagman and V.A. Medvedev: *CODATA Keyvalues for thermodynamics*, Hemisphere Publishing Corporation, New York (1989).

[2] M.W. Chase *et al.*: *J. Phys. Chem. Ref. Data*, Suppl. 1 (1985) 1 - 1856.

[3] R.W. Ohse (ed.): *Handbook of thermodynamic and transport properties of alkali metals*, Blackwell Scientific Publications, Oxford (1985).

[4] W.M. Fairbank, Th. W. Hänsch and A.L. Schawlow: *J. Opt. Soc. Am.* (1975) **65**, 199 - 204.

[5] R. Hultgren *et al.*: *Selected values of the thermodynamic properties of the elements*, American Society for Metals, Metals Park, Ohio (1973).

[6] V.S. Bhise and C.F. Bonilla: *Proc. 6th Symp. Thermophys. Properties (Atlanta)*, ASME, New York (1973) 362.

[7] W.H. Lien and N.E. Phillips: *Phys. Rev.* (1964) **113**, 1370 - 1377.

[8] J.D. Filby and D.L. Martin: *Proc. Roy. Soc. A* (1965) **284**, 83 - 107.

[9] T.M Dauphinee, D.L. Martin and H. Preston-Thomas: *Proc. Roy. Soc. A* (1955) **233**, 214 - 227.

[10] D.L. Martin: *Can. J. Phys.* (1970) **48**, 1327 - 1339.

[11] D.C. McCollum and H.B. Silsbee: *Phys. Rev.* (1962) **127**, 119 - 120.

[12] D.L. Martin: *Phys. Rev.* (1965) **139**, 150 - 160.

[13] I.T. Aldigev and I.M. Pchelhin: *Thermophysical Properties of Alkali metals*, Izdvo Standartoo (1970).

[14] J.K. Fink and L. Leibowitz: *Handbook of thermodynamic and transport properties of alkali metals*, Blackwell Scientific Publications, Oxford (1985) 411 - 434.

[15] N.E. Holden, R.L. Martin and I.L. Barnes: *Pure Appl. Chem.* (1983) **55**, 1119 - 1136.

[16] A.H. Wapstra and G. Audi: *Nucl. Phys. A* (1985) **432**, 1 - 13.

[17] E.A. Guggenheim: *Thermodynamics*, North-Holland Physics Publishing, Amsterdam (1988).

[18] E.R. Cohen and P. Giacomo: "Symbols, units, nomenclature and fundamental constants in physics," *Physica A* (1987) **146**, 1 - 68.

[19] P.E. Gill and G.F. Miller: *Computer J.* (1972) **15**, 80 - 83.

[20] N.E. Holden and R.L. Martin: *Pure Appl. Chem.* (1983) **55**, 1101 - 1118.

[21] I.I. Sobelman: *Introduction to the theory of atomic spectra*, Pergamon Press, Oxford (1972).

[22] A.M. van der Spek and J.J.L. Mulders: *J. Opt. Soc. Am. B* (1988) **5**, 1478 - 1483.

[23] A.C.G. Mitchell and M.W. Zemansky: *Resonance radiation and excited atoms*, Cambridge UP, Cambridge (1971).

[24] M.Roos *et al.*: *Statistical methods in experimental physics*, North - Holland Physics Publishing, Amsterdam (1986).

VAPOUR PRESSURE OF SOLID Au_5Rb FROM EFFUSION EXPERIMENTS

4.0. Abstract

The published phase diagram of the gold - rubidium system was used to prepare the compound Au_5Rb and to evaluate its thermodynamic properties.

The vapour pressure of the solid compound in the temperature range 580 °C - 690 °C was measured using a Knudsen cell and a total collection method. The collected effusate was weighed and inspected for other effusate species than Rb by proton induced X-ray emission. Calculated vapour pressures derived from the calculated free enthalpy of formation of the compound were found to be many orders larger than the measured vapour pressures. This may indicate the existence of congruent, rather than peritectic, melting of the Au_5Rb compound at a temperature higher than the melting point of gold.

4.1. Introduction

Intermetallic compounds of gold with one of the alkali-metals have been the subject of study by a very limited number of researchers. Specifically in the case of the Au-Rb (gold-rubidium) system most of our present knowledge is based entirely upon one single paper [1][2] dating back to 1961. Later reviews of the work reported in the 1961 paper by Pelton [2][3][4][5][6] have revealed some serious discrepancies with measurements reported by other authors. The assessed Au-Rb phase diagram in Figure 1 should therefore be used with caution. Nevertheless this phase diagram was used by the present author as starting point for the work reported in this paper.

The aim of this work was to develop a calibrated source of very low ($< 10^9$ m^{-3}) density rubidium vapour. Although the open literature lists several designs of sources of low vapour pressure, high reactivity gas which are compatible with normal ultra-high vacuum practice [7][8][9] we chose to develop our own source. The principal reason for developing an entirely new source was that our source had to deliver vapour phase rubidium atoms, in contrast to conventional sources which supply a flux of atoms or molecules to be adsorped at a certain surface. Specifically, commercially available alkali metal dispensers [10] were thought to be unsuited as they are known to release relatively large (up to 1 mbar.l/cm) quantities of gas (H_2, CO_2 and CO) [10][11][12] in addition to the desired alkali. Furthermore the fluxes from such dispensers are rather high for our application (several µg/cm/s).

Our source is based upon the thermodynamic equilibrium between vapour phase rubidium atoms and Au_5Rb compound at a certain temperature.

Calibration of this source required the availability of a set of p-T curves for different values of the overall rubidium fraction x. In order to obtain these curves, we have measured the partial (equilibrium) pressure of rubidium for

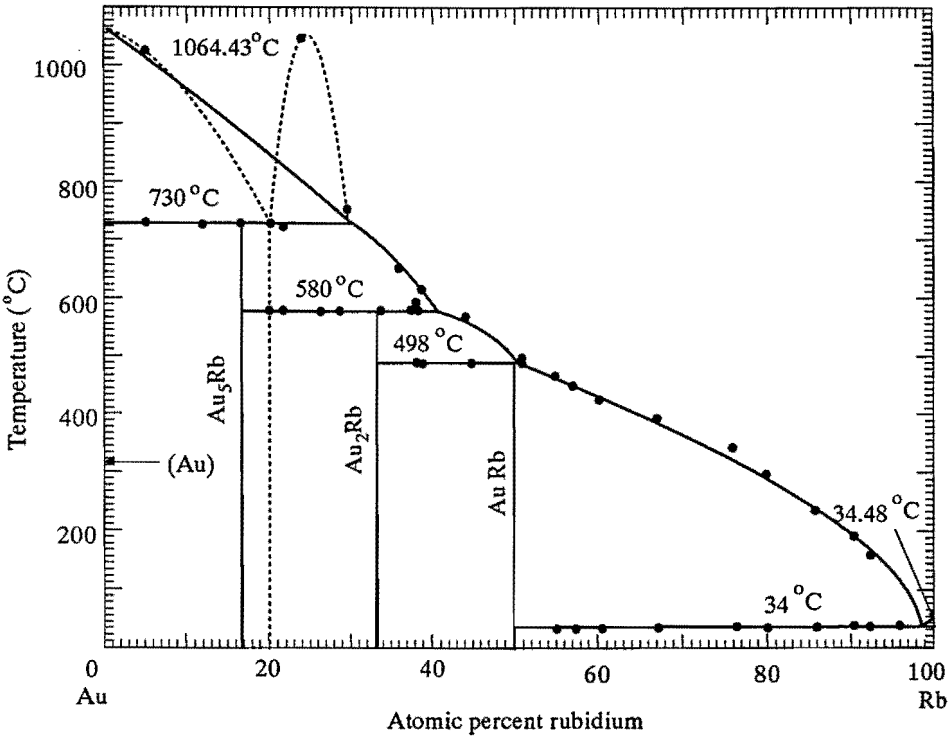

Figure 1 Au-Rb phase diagram

The assessed phase diagram is reproduced here. The data points obtained by Kienast [1] have been inserted and the phase diagram suggested by him has been dashed. The dashed line gives a congruent melting point of the Au_5Rb compound in the vincinity of 1100 °C. Such a congruently melting compound cannot explain the data points at 730 °C and x > 0.16. Moreover the position of the congruent melting point (at x = 0.2) disagrees with the stoechiometric composition of the compound.

three values of x by Knudsen effusion [13]. Analysis of the effusate was done by Particle Induced X-ray Emission analysis (PIXE) [14].

Results are presented in paragraph 4.4. for a temperature range of 600 to 700 °C. Above 730 °C the equilibrium partial pressure of rubidium may be calculated from the Au liquidus slope as will be shown in paragraph 2. Below the invariant temperature the unknown heat of formation of the Au_5Rb compound excludes this possibility. Our measurements, however should allow a calculation of the heat of formation of the Au_5Rb compound.

The experiment itself is described in paragraph 4.3. We had to solve a whole array of problems in order to get reproducible results. Most of the problems proved to be traceable to a limited understanding of the behaviour of the Knudsen cell. Therefore we experimented with three different cell materials and two different seizes of effusion holes. In addition we studied the behaviour of our cell geometry and the influence of cell-vapour interaction by Monte-Carlo simulation.

4.2. Theory

4.2.1. Thermodynamics of the Au_5Rb intermetallic

The partial vapour pressure of rubidium p_{Rb} in equilibirium with Au_5Rb at a certain temperature may be calculated from:

$$\Delta_f G^o(Au_5Rb,sol,T) = \frac{1}{6} RT \ln\left(\frac{pRb}{p^oRb}\right) \qquad (1)$$

where $\Delta_f G^o$ is the Gibbs free enthalpy of formation of the compound, R is the gasconstant and p^oRb is the rubidium vapour pressure at temperature T for pure rubidium. This equation follows from the reaction equilibrium:

$$\frac{5}{6} Au(sol,T) + \frac{1}{6} Rb(liq,T) = \frac{1}{6} Au_5Rb(sol,T) \qquad (2)$$

At the transition temperature where the Au_5Rb compound decomposes (peritectic invariant at 730 °C) the Gibbs free entalpy of formation of Au_5Rb may be obtained from the known Au liquidus. The ideal association model is assumed to be valid in the liquid state. Thus the liquid state is regarded as a regular solution of Au and AuRb 'particles'. As standard state we shall adopt Au(sol) and AuRb(liq), thus G^o(Au,sol) and G^o(AuRb,liq) are set to zero arbitrarily. Referring to the free enthalpy diagram in Figure 2, we have for the liquid state:

$$G^o(Au\text{-}AuRb,liq,T) = (1-x)\, G^o(Au,liq,T) + RT\,(x\ln x + (1-x)\ln(1-x)) + G^{ex} \qquad (3)$$

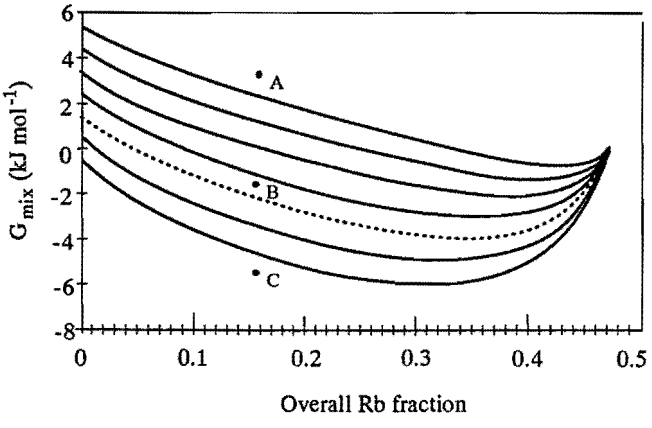

Figure 2 Free enthalpy of formation of the Au-Rb system as calculated from the ideal association model

This graph illustrates the decrease in Gibbs free enthalpy upon mixing gold and rubidium. Reference states are Au(sol) and Au-Rb(liq). Upon mixing the Gibbs free enthalpy decreases due to the Gibbs mixing enthalpy and due to non-ideal effects. Parameter of the curves in this graph is temperature, running from 1100 °C at the lowest curve to 500 °C at the topmost curve in 100 °C intervals. A compound is formed at a particular temperature whenever its free enthalpy of formation is below the liquid mixing curve at that temperature.

Where G^{ex} is the excess free enthalpy given by Pelton [2]:

$$G^{ex} = w\,x(1-x) \qquad (w=7450\ [J\ mol^{-1}]) \qquad (4)$$

Here w is a small regular solution parameter. $G^{o}(Au,liq.T)$ is the liquid state free enthalpy for gold calculated from the heat of fusion of gold $\Delta_f H^{o}$ which itself is assumed to be independent of temperature [15]:

$$G^{o}(Au,liq,T) = \Delta_f H^{o} - \frac{\Delta_f H^{o}}{T_m} T = 13000\ [J\ mol^{-1}] - 9.719\ [J\ mol^{-1}\ K^{-1}]\ T \quad (5)$$

and where T_m is the melting temperature of gold (1064.39 °C). In Eq. 3, x is the mole fraction of rubidium species and (1-x) is the mole fraction of free gold species. These quantities differ from the overall rubidium mole fraction used as abcissa in the phase diagram of Figure 1. This of course is a natural consequence of the association model being used. In addition $\Delta_f G^{o}(Au_5Rb,sol,T)$ has been plotted in Figure 2. Three conceptually different situations may arise:

$$\Delta_f G^{o}(Au_5Rb,sol,T) > G^{o}(Au\text{-}AuRb,liq,T) \qquad (6)$$

$$\Delta_f G^{o}(Au_5Rb,sol,T) = G^{o}(Au\text{-}AuRb,liq,T) \qquad (7)$$

$$\Delta_f G^{o}(Au_5Rb,sol,T) < G^{o}(Au\text{-}AuRb,liq,T) \qquad (8)$$

In each case a 'common tangent' construction [16] leads to the appropriate phase boundary in the phase-diagram (T-x diagram; Figure 1). The gold liquidus may thus be obtained from:

$$\frac{G^{o}(Au\text{-}AuRb,liq,T) - G^{o}(Au,sol,T)}{x_{liq} - x_{(x=0)}} = \left[\frac{dG^{o}(Au\text{-}AuRb,liq,T)}{dx}\right]_{(x=x_{liq})} \quad (9)$$

which leads to:

$$G^{o}(Au,liq,T) + RT\ \ln(1-x) + wx^2 = 0 \qquad (10)$$

This equation holds in those cases where $\Delta_f G^{o}(Au_5Rb,sol,T) > G^{o}(Au\text{-}AuRb,liq,T)$ corresponding with situations of Eq. 6 which have been drawn schematically in Figure 2. As the temperature is lowered the situation of Eq. 7 will occur at T = 1003.15 K (730 °C). Hence at this temperature the Gibbs free enthalpy of formation of Au_5Rb is calculated as:

$\Delta_f G^{o}(Au_5Rb,T=1003.15\ K) =$

$$(1-x)\ G^{o}(Au,liq,T) + RT\ (x\ln x + (1-x)\ln(1-x)) + G^{ex} \quad (11)$$

where x = 1/6. This equation holds in the case where $\Delta_f G^o(Au_5Rb,sol,T) = G^o(Au\text{-}AuRb,liq,T)$ schematically depicted in Figure 2 as the situation of Eq. 7. At lower temperatures still, the situation of Eq. 8 arises where we may write formally:

$$\frac{\Delta_f G^o(Au_5Rb,sol,T)-G^o(Au\text{-}AuRb,liq,T)}{x_o-x_{liq}} = \left[\frac{dG^o(Au\text{-}AuRb,liq,T)}{dx}\right](x=x_{liq}) \quad (12)$$

Given a number of data points for the Au_5Rb liquidus in Figure 1, the Gibbs free enthalpy of formation of the compound Au_5Rb may be calculated as a function of temperature.

In view of the uncertainties in the assessed phase diagram an alternative way of calculating $\Delta_f G^o(Au_5Rb,sol,T)$ is desirable. The more so because this quantity determines the outcome of our experiments to a large extent. While at temperatures above 730 °C vapour pressures of rubidium may be calculated from the liquidus equation Eq. 10 with reasonable accuracy from [17];

$$\frac{p_{Rb}}{p^o_{Rb}} = x \exp\left[(1-x)^2 \frac{w}{RT}\right] \quad (13)$$

caution is to be practised at lower temperatures for several reasons:

1 The peritectic invariant temperature (730 °C) may be wrong by as much as 25 °C [2].

2 The solubility of Au_5Rb in solid gold is thought to be very small and has been set to zero arbitrarily [2].

3 The value of the excess free enthalpy of mixing is based upon a liquidus fit through only 3 data points, the fourth being rejected as spurious [2].

One other method was used to obtain the enthalpy (Helmholtz), not free enthalpy (Gibbs) of formation of the Au_5Rb compound. The method is based upon the semi-empirical model of Miedema [18][19][20] which is capable of predicting the enthalpy of formation of a compound like Au_5Rb from basic atomic data. Thus for the Miedema approach we have:

$$\Delta_f G^o(Au_5Rb,sol,T) = \Delta_f H^o(Au_5Rb,sol,T) \quad (14)$$

where it is assumed that the entropy of formation of the compound is very small. An assumption which is not uncommon in this field [20]. Results of the calculation of $\Delta_f G^o(Au_5Rb,sol,T)$ according to either Eq. 12, Eq. 13 or Eq. 14 for the four temperatures where a data point is available are summarized in Table 1.

4.2.2. Knudsen effusion and Langmuir free evaporation

There are many ways of evaluating the thermodynamice properties of metals and alloys. A review of the more accurate methods is given by Komarek [21]. We chose to use a vapour pressure method because we were primarily interested in the vapour pressures itself. Since the vapour pressures were expected to be very low an effusion type of experiment suggested itself, particularly since we could make use of a very sensitive analysing facility capable of detecting very small amounts of both gold and rubidium separately and quantitatively. If the activities of Au_5Rb were as high as calculated in the preceding paragraph by the 'common tangent' method, a (Knudsen) effusion type of experiment would not be suited to determine the vapour pressure of rubidium. However, we had reason to believe that these activities as calculated from the phase diagram are far too high. Even so Knudsen data are to be supported by auxiliary information because vapour pressures obtained from effusion studies are prone to several types of experimental errors like:

1 Unknown vaporization behaviour.

2 Unknown condensation behaviour.

3 Possible cell-wall vapour interaction.

Since rubidium is a highly reactive metal and because of the complex vapourization behaviour of rubidium from a compound like Au_5Rb the calculation of a vapour pressure from measured effusate masses is not straightforward. We have tried to cope with these difficulties in the following way.

1 Vapourization behaviour

Even for mono-atomic vapours originating from simple mono-atomic crystals a complete picture of vaporization behaviour is not available. Theories are applicable to pure substances only. Thus bulk-diffusion, surface depletion and molecule dissociation, all of which may occur during vaporization of rubidium from Au_5Rb are not taken into account. Therefore we only test the reproducibility of effusate masses and it is assumed that the details of vaporization behaviour are of no concern to us as long as the following set of conditions can be maintained.

a. Effusate masses taken at one temperature vary linearly with effusion time.

b. Effusate masses do not depend on the concentration of rubidium as long as this concentration is between 0 and 16 atomic percent.

c. Different pieces of material must give equivalent results.

d. Effusate masses determined in different experimental runs under the same conditions must be the same.

Table 1 Free enthalpy of formation of the Au_5Rb (gold(5)-rubidium) compound

Temperature	730 C 1003.15 K	730 C 1003.15 K	670 C 943.15 K	630 C 903.15 K	580 C 853.15 K
Overall Rb fraction x	0.167	0.300	0.339	0.337	0.410
Mole fraction Rb x/(1-x) in liquid state	n.a.	0.428	0.512	0.605	0.695
$\Delta_f G^o$ [J mol^{-1}] 'common tangent' Eq. 12	-14 Eq. 11	-809	-445	-456	-411
$\Delta_f G^o$ [J mol^{-1}] 'Miedema model' Eq. 14		-10663	-10663	-10663	-10663
Rubidium Activity $a_{Rb} = p_{Rb}/p^o_{Rb}$ from 'common tangent'	0.99	0.56	0.71	0.69	0.71
from 'Miedema model'	-	0.00047	0.00029	0.0002	0.00012
from Au liquidus Eq. 13	0.30	0.57	0.64	0.71	0.77
Rubidium (pure) vapour pressure p^o_{Rb} [kPa]		136.6	79.2	52.4	29.8
Rubidium (compound) vapour pressure p_{Rb} from Eq. 12 [kPa]		76.3	56.3	36.4	21.1
from Eq. 14 [Pa]		63.6	22.6	10.4	3.61

2 Condensation behaviour.

For vapour species differing in atomic structure from the condensed phase, condensation coefficients may be much smaller than one. This is very unfortunate actually, because if the condensation coefficient were one, possible cell-wall vapour interaction would not influence the total mass effusing [27]. Conversely if there were no wall losses the condensation coefficient can be determined as the ratio of effusate masses from a Langmuir free evaporation run and a Knudsen effusion run taken at otherwise similar conditions. We have done exactly this but for a cell where the wall reflection coefficient β is made equal to one minus the condensation coefficient by gold-plating the entire cell:

$$\beta = 1 - \alpha \qquad (15)$$

The condensation coefficient then follows by comparing the measured mass ratio with Monte-Carlo simulations.

3 Wall-losses.

Adsorption of vapour on the wall of the effusion cell may, when the condensation coefficient is not unity, drastically reduce the amount of material effusing. However it has been shown [22] that the influence of wall losses can be approximately corrected for if the effusate mass distribution is known. In our case the rubidium mass distribution on the sample can be measured with a scanning proton micro probe.These measurements,however have not been done as yet. This leaves all experimental results to be reported in paragraph 4 in some doubt. The possibility of wall losses can never be ruled out until the vaporization behaviour of rubidium throughout the interior of the cell is known. In order to cope with this omission we have adopted the following procedure:

1 All the measured rubidium masses are recalculated in terms of vapour pressures p_{eq} by application of the Motzfeldt formula [23]:

$$p_{eq} = \left(1 + C_a \frac{a}{A} \left[\frac{1}{\alpha} + \frac{1}{C_A} - 2 \right] \right) \frac{m}{F C_a a t} \sqrt{\frac{2\pi RT}{M_{Rb}}} \qquad (16)$$

where it is assumed that the condensation coefficient α takes the value determined in above mentioned experiments with gold-plated effusion cells. The other symbols in Eq. 16 are explained as follows; m is the effused rubidium mass in time t at temperature T, F is a viewing factor necessary to correct for the presence of a collimator shield. C_a, a, C_A and A are, respectively the Clausing factor for the effusion hole, the effusion hole area and the Clausing factor and area of the cell cross sectional diameter. R and M_{Rb} are the gas constant and the rubidium molar mass respectively.

2 Monte-Carlo simulations are used exclusively to determine the influence

of non-ideal cell behaviour and/or non-unity condensation coefficients.

In a series of six papers, Ward et. al. [24][25][26][27][28][29] have studied the behaviour of Knudsen cells by comparing Monte-Carlo simulations with experiments. Although their cell geometry differs from ours, their general conclusions remain valid;

a A channel orifice is a better choice than a knife-edge orifice for experiments where the evaluation of the pressure does not require a strict cosine distribution of the effusate.

b The geometry of the set-up should be such that the collector 'sees' only the sample material on the bottom of the Knudsen cell. This then ensures that only the sample flux is analyzed and not the flux from the cell wall.

c If the absorption coefficient of vapour on the cell wall is close to unity the return flux to the sample will almost equal the steady-state sample emission flux. Hence the condensation coefficient will not influence cell emission.

In the gold-plated Knudsen cell all three observations a,b, and c were implemented. The observation c is automatically fulfilled since the condensation coefficient α is known to be very small leading to an absorption coefficient $1-\beta$ close to unity.

4.3. Experimental

4.3.1. Preparation of the compound

The gold rubidium compounds were prepared form pure rubidium (Merck 12314) and pure gold obtained from Philips Research Laboratories. The purity of the raw materials was left unchecked. A small piece of gold was weighed and put into a ceramic crucible. Liquid rubidium was added to the crucible in amounts to make up for a certain concentration rubidium by weight. The pipetting and weighing was carried out in an argon glove box to prevent the oxidation of the rubidium. After weighing and checking, the crucible was sealed in a molybdenum bomb by argon arc welding and the bomb was removed from the glove box. Table 2 lists the actual weighing data on the bombs as prepared. In order to prevent oxidation of the molybdenum, the bombs were sealed in evacuated glass envelopes The tubular envelope could then be heated in a tube oven (Hereaus).

Initially the bombs were heated to 1100 ^{o}C, well above the melting point of gold, and they were kept at this temperature for at least one hour before slow cooling to 800 ^{o}C commenced. The bombs were held at 800 ^{o}C for at least one day. Upon further cooling to 600 ^{o}C the compound Au_5Rb was formed and allowed to anneal during a week at 600 ^{o}C.

Next the bombs were opened and its contents inspected both visually and microscopically. No mettallographic analysis was carried out however, since

the present authors lack the necessary experience in this field. In one case the gold had not been melted completely possibly indicating a temperature error in the stove controller. Effusion experiments with this sample were done on small pieces cut from the gold plate. in all cases the gold had lost its brilliant shine. the color of the compound was black or grey. Under the microscope small dots of brilliant free gold could still be seen in the grey areas. Apart from the color observation this procedure of preparation is comparable to the procedure of Raub and Compton [30]. We feel that the present procedure, although by no means optimal, is satisfactory.

4.3.2. Construction of the effusion cells

The effusion cells used in this work were flat thick walled cylinders with a thin lid, not unlike a small pill-box. The cell as whole could be inserted in a copper heater as outlined in Figure 3. The copper heater contained both the thermocoax heating wire and the K-type thermocouple. This thermocouple was used for measurement and control of the cell temperature. We employed an Eurotherm 815S controller. Temperatures are accurate to within 1 ^{o}C absolute, although the thermocouple itself is accurate only to within IEC tolerances (0.4 % from 375 ^{o}C to 1000 ^{o}C). Large temperature gradients in the cell are unlikely both due to the small size and to the enclosure in a copper heater. At the highest temperatures used in this work (< 700 ^{o}C) where the cell was glowing with a dull red color, the lid and the effusion hole may have been cooler by a few degrees, but this is considered to be a minor effect. The effusion cells were manufactured from either molybdenum, gold-plated copper or carbon. The lid was made of the same material as the cell itself. Effusion holes were drilled into the 0.3 mm thick lid. The geometry of the effusion hole was determined by measuring two perpendicular diameters with a microscope equipped with a double translation stage. Diameters were read directly from a measuring clock (Mitutoyo 2052 E 10, accuracy according to DIN 878) attached to the xy-stage. An area of 0.0314 mm^2 was found. with a standard deviation of 0.0002 mm^2.

4.3.3. Samplle preparation and validation.

All the effusion runs were done in a vacuum bell-jar (Balzers BA 510 Automatic) at a vacuum of 10^{-6} torr or better. Effusion cell and collimator were mounted rigidly on top of each other. The samples could be rotated above the effusion hole one after the other by placing them on the sample carriage. We used polycarbonate filters (Nuclepore [31]) as collector material. The filters were spotwelded between two 35 mm slide sized aluminum plates in which a 20 mm diameter hole had been punched. Polycarbonate was chosen as collector material because of its mechanical strength, its ease of use, its low contaminination, and its commercial availability. We had no specific reason to expect 100 % sticking of rubidium to the chosen collector material. Therefore three tests were carried out to test the possible loss of effusate during sample handling after venting of the bell-jar.

Table 2 Bomb weighing data

Bomb No:	Gold mass [g]	Rubidium mass [g]	Weight percent Rb	Atomic percent Rb
1	1.98	0.02	1.00	2.27
2	1.94	0.06	3.00	6.65
3	1.84	0.16	8.00	16.7

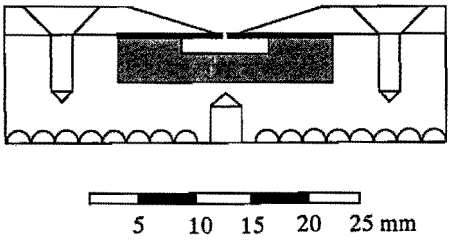

Figure 3 Outline drawing of the Knudsen cell and its heater

The drawing shows the actual cell inserted in its copper heater.The cell lid is pressed firmly against the cell body by the copper ring mounted on the heater body by 8 screws. The copper heater is heated from below with a thermocoax wire. Temperature sensing is done with a K - type thermocouple (not shown) inserted through the heater body so that its tip is pressed against the cell body.The heater body is fixed to the its support with one screw in the middle of its downward facing side.

a. In one case three samples were remeasured after an interval of approximately six months. The results differed by no more than 10 %.

b. Two stacked samples were measured separately. While the sample which had been exposed to the cell flux showed normal behaviour, we were unable to obtain a signal from the other. thus no measurable amount of rubidium atoms traverse the collector material either through the filtration holes or otherwise.

c. An exposed sample and a blank were pressed firmly against each other directly following the venting of the bell-jar. the two samples were held together up to the moment of mounting them in the analysis chamber. Separate analysis showed that the blank sample had remained blank, demonstrating that rubidium collected on the polycarbonate does not come of easily.

While it is true that collected rubidium atoms may be lost upon subsequent venting, we feel that this is unlikely. In case of any doubt, analysis of the upward side of the collimator shield (the side facing the collector) should then be conclusive. If the collected rubidium atoms do not stick to the polycarbonate, then the upward side of the collimator should be contaminated with them. Such a test, however, was not performed by the present authors.

4.3.4. PIXE analysis and calibration

Analysis of the collected effusate masses were done with the PIXE elemental analysis facility available at the cyclotron laboratory. This facility has been described, in sufficient detail, elsewhere [32].

We calibrated the PIXE set-up for rubidium with samples prepared from a dilution series of RbCl (Merck 7615) in distilled water coloured with a very small amount of Rhodamine B dissolved in ethanol. The dilution series was prepared gravimetrically. Atomic weights of the elements were taken from the 1981 IUPAC review [33]. The molecular weight of RbCl was calculated as the sum of the atomic weights of the constituents. The micro-pipet used for dispensing one droplet on the sample was calibrated gravimetrically using the measured density of the solvent.

This calibration procedure should give an approximately linear relation between the normalized peak area of the rubidium K peak (cnts/μC) and the total rubidium mass (ng) seen by the proton beam. Peak areas are extracted from a measured spectrum by fitting the spectrum with a number of possibly partly overlapping Gaussian peaks representing the X-ray transitions of the elements superposed on a linear background. The fitting uses the non-linear least squares method due to Marquardt employing a global stop criterion based upon a χ^2 test.

Great care was taken to ensure a homogeneous beam of larger radius than

Table 3 Calibration of PIXE with RbCl dilution series

Charge [µC]	K peak area [cnts]	Standard deviation [cnts]	Mass Rb on target [ng]
11	8185	39	1914
10	1317	16	383
10	520	10	191
20	593	8	95.7
50	396	7	24
50	209	6	5.75
30	55	11	2.87
30	360	9	0.72

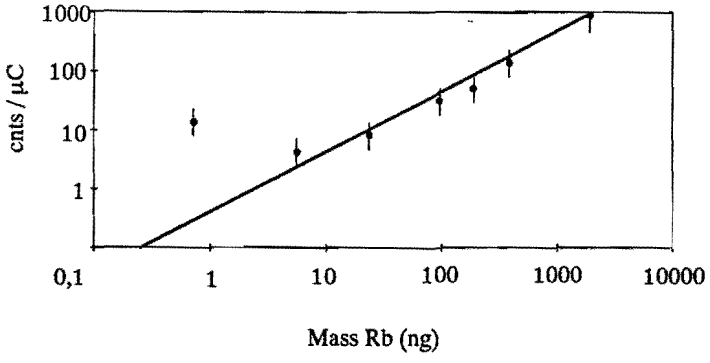

Figure 4 Calibration of PIXE with a dilution series

The calibration points in this graph were obtained by measuring the peak area (in counts) of the rubidium K peak after irradiation with a low current beam for about half an hour. The rubidium mass on the target material (ME44 paper) is known. A known volume of a solution containing water, alcohol, methyl red and RbCl was dispensed on the paper target. The solution is prepared gravimetrically.

the radius of the sample spot on the target. Only if this is the case can the number of counts detected be related to the total mass on the sample without knowledge of the mass distribution on the sample [14]. A diffusor foil was used to homogenize the proton beam. The result of the calibration is shown in Figure 4. Input data is given in Table 3.

Figure 4 immediately shows that the point at 0.7 ng Rb must be spurious. This point was disregarded when fitting the data points to a straight line through the origin. The result of the least squares analysis is presented in an equation relating the K peak area to the rubidium mass present on the sample:

$$\text{Mass Rb [ng]} = (2.56 \pm 0.01) \frac{\text{K peak area [cnts]}}{\text{Accumulated charge [}\mu\text{C]}} \qquad (17)$$

This relation was used in all further work to evaluate effused masses from the Knudsen or the Langmuir cells. A number of differences between the calibration samples and the effusate samples may, however, influence the calibration constant in Eq. 17.

1 The calibration samples are made of filtration paper (ME44) enclosed in commercially available 35 mm slide holders. The effusate samples are, as was described earlier, made of polycarbonate (Nuclepore) enclosed in aluminum holders. Thus both the thickness, the microstructure and the material of the samples and their supports differs. However, since both sample materials are thin and of low contamination the influence on the calibration constant is probably negligible. Contamination of the support does slightly raise the background but this was never a problem.

2 The analysis of the calibration samples was always done while a diffusor foil homogenized the proton beam. In order to speed up the analysis the diffusor foil was not used when analyzing effusate samples with very low rubidium masses on it. The much higher beam current presented no problem for the polycarbonate collector material, but the calibration constant must now differ from the one used in Eq. 17. Samples with a very low rubidium content, however only occurred when a molybdenum effusion cell was used.

3 Whereas the colouring of the solvent used to dissolve the RbCl allowed for a visual check upon the alignment of the center of the proton beam with the center of the coloured sample spot on the paper, such a check could not be performed with the effusate samples. A misalignment with a corresponding change in the calibration constant is a real possibility. To prevent this the geometry of the effusion set-up, the collimator diameter in particular, was chosen such that small misalignments do not shift the border of the effusate carrying area out of the proton beam.

4 Due to the different use of calibration and effusate samples, handling and storage differed markedly. Most important and with easily observed influence is the spot welding of the polycarbonate between aluminum

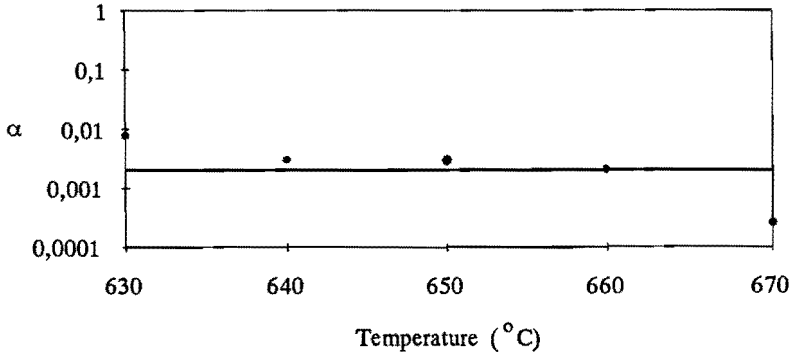

Figure 5 Condensation coefficient of gold(5)-rubidium

The condensation coefficient is the ratio of the molecular flux leaving a surface (reflection and evaporation) and the flux arriving at a surface. For pure ideal substances the condensation coefficient equals 1, indicating complete sticking of all molecules impinging on a surface. For surfaces differing in composition from the gas phase molecules the condensation coefficient may be much smaller than one. This is illustrated in this graph.

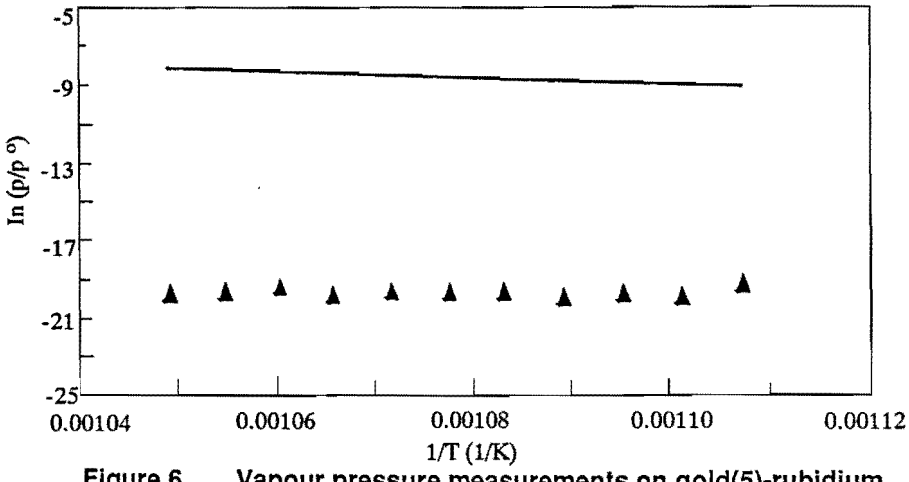

Figure 6 Vapour pressure measurements on gold(5)-rubidium

Here the measured vapour pressures (triangles) are compared with calculations (squares) using the Miedema model for the heat of formation of Au_5Rb. Calculated values of the vapour pressure using phase diagram data would be even larger than the calculation from the Miedema model.

holders. Minor contamination with zinc, iron and copper is always observed on blank spot welded samples and the contamination is almost certainly due to the spot welding process. Contamination adds background to the rubidium K peak but is not harmful otherwise. Only at very low rubidium concentration does the extra background present a problem.

Since the purpose of this paper is not to attain the highest precision, lest this were possible using a material like gold(5)-rubidium, we feel that the calibration given is satisfactory.

4.4. Results

4.4.1. Determination of the condensation coefficient

The condenstation coefficient α was calculated from the measured mass ratios of two series of experiments one employing a Knudsen cell and one using free evaporation in a Langmuir cell. In both cases gold-plated copper cells were used. The result of these series is a condensation coefficient of 0.002 with a standard deviation of 0.001, this is illustrated in Figure 5 where the temperature of the cell was used as an ordinate to illustrate the sensitivity of the condensation coefficient with temperature. Theoretically there should be no such influence.

As expected the condensation coefficient is very small and roughly constant over the temperature range used. The small condensation coefficient indicates that wall absorption of vapour in the Knudsen cell will drastically reduce the amount of effusate even if the wall absorption coefficient is very small. Because of this it was decided to try a carbon effusion cell instead of a molybdenum cell or a gold-plated copper cell. The much larger signals obtained when using a carbon cell indicated that the wall losses in a carbon cell were even lower than the wall losses in a gold-plated copper cell. The carbon cell was then used in all further work and we had to conclude that all data obtained from the molybdenum cell are unreliable.

4.4.2. Vapour pressure measurements

Vapour pressures were calculated from data obtained with effusion samples from the second bomb at an overall rubidium mole fraction of 6.65%. The carbon Knudsen cell was used exclusively. Only a limited data set could be obtained in the allocated cyclotron beamtime. Generally speaking one effusion run of seven samples (differing in cell temperature) plus a blank sample could be analyzed in one day, not counting the time required for setting up the required homogeneous proton beam at a current of roughly 30 nA.

Results of the vapour pressure measurements in Figure 6 (triangles) are presented in the Clausius - Clapeyron format which should yield a straight line between the logarithm of the normalized vapour pressure and the inverse of absolute temperature.

In Figure 6 the calculated vapour pressures based upon activities obtained from the Miedema model have been included (rectangles) for comparison. Two features show up immediately:

1 There is a wide gap between the calculations and the measurements.

2 Whereas the calculations do indeed show the expected linear decrease with increasing inverse temperature, the measured data are roughly constant.

Neither of these two features has a direct explanation in terms of systematic errors introduced somewhere in the experimental work. This forced us to reconsider all the steps taken from preparation of the compound up to analyzing the effusate with PIXE. A major mismatch between calculations and experiments could have been caused by:

1 A phase diagram that does, contrary to the phase diagram of Figure 1, show a congruent melting point of Au_5Rb near 1100 ^{o}C. This possibility cannot be ruled out since there exists only one extensive study of the phase diagram of the gold-rubidium system and the one study that exists [1] did indeed show such a congruent melting point. In the 1986 review of this phase diagram by Pelton [2] the phase diagram of Figure 1 was proposed because of some inconsistencies in the work of Kienast and Verma [1]. Pelton also reviewed the other systems of gold and one alkali metal [3] [4] [5] [6] and in the similar systems gold-sodium and gold-kalium a congruent melting point of the gold(5)-alkali compound does indeed occur.

   If then, there exists such a congruent melting point near 1100 ^{o}C, then the preparation of the compound as it was intended will have failed. In that case the comparison with theory breaks down completely because the sample material is undefined but almost entirely gold with perhaps tiny traces of probably oxidixed rubidium.

2 The rubidium effusate does not stick to the polycarbonate used as collector material. If this were true then indeed the analyses would reveal a rubidium mass that is much too low. We had no reason to expect 100% sticking, but there is also no reason to expect virtually no sticking at all. In this respect it must be noted that the quantities rubidium that we are dealing with are small. Also changes in the chemical form of rubidium after it was collected on the polycarbonate do not influence the analyses since PIXE is sensitive to inner shell electron transitions which are hardly, if at all, affected by chemical bonds.

3 Severe surface depletion causes an appreciable decrease of the amount of rubidium that is able to vaporize readily from the surface. Although this is a real possibility the flatness of the data does not support such a hypothesis.
   Theoretically the enthalpy of formation for rubidium mono vacancies in a gold matrix may be calculated from the ratio of the molar volumes of rubidium and gold raised to the power 5/6. This procedure is validated in

the same manner as the Miedema model itself [20]. Taking 14.65 cm^2 for the surface of one mole of rubidium (mono)vacancies, 4.70 cm^2 for the surface of one mole of gold (mono)vacancies and a value of 100 kJ/mol for the enthalpy of formation of gold monovacancies in a gold matrix, we find a value of 414 kJ/mol for the enthalpy of formation of rubidium (mono)vacancies in a gold matrix. This value is high enough to prevent diffusion of rubidium to the surface at temperatures below the peritectic temperature.

4 The Miedema model is known to yield values for the enthalpy of formation of alloys with an alkali as one of the constituents that are numerically too small. The difference between the calculated and the experimental values for the heat of formation can be as large as 30 kJ/mol for compounds rich in the alkali. This must be compared with a difference between the measured and calculated vapour pressures which can be expressed as a heat of formation difference of 25 kJ/mol.

5 During the effusion runs, the surface of the material may have become contaminated with water promoting the formation of rubidium oxides, hydrides and hydroxides. Formation enthalpies for the rubidium oxides are about 100 kJ/mol [20]. This value is large enough to prevent decomposition of the oxides at the temperatures where we operated our Knudsen cell. Thus the observation of measurable quantities of rubidium itself contradicts the contamination hypothesis. Moreover the PIXE analysis never revealed the presence of gold on the collector. At our experimental temperatures, the large heat of formation of gold vapour prevents this. By analogy, we may conclude that the formation of any bond between a contaminant and rubidium must have an enthalpy of formation at least a factor of 10 lower than the enthalpy of formation of gold vapour.

4.5. Conclusion

First and foremost should the published phase diagram of Figure 1 be confirmed, preferably by differential thermal analysis [21].
Then some independant means of establishing the condensation coefficient must be applied in order to confirm the value given in this work. Most important is the evaluation of the effusate mass distribution on the collector material which will allow an assessment of the behaviour of the cell material [22]. If the material proves to be a strong absorber then the wall must be made of a more inert material.
In view of the different predictions for the vapour pressures given in Table 1, and because of the enormous difference in the measured and the calculated data we feel that a congruent melting point of Au_5Rb in the vicinity of 1100 ^oC is more likely than was assumed by Pelton in his 1986 review [2] of the original data of Kienast and Verma [1].
In view of the many diffuculties oulined in the preceding paragraph, a straightforward comparison with theory is difficult. Detailed knowledge about

the vapourization and condensation process of rubidium is required before another attempt to compare our data with theory becomes useful.
Analysis of effusate by the PIXE method was shown to be quick and easy. The analysis was shown to be capable of calibration so that low quantities of rubidium could be measured quantitatively.

REFERENCES

[1] G. Kienast and J. Verma: *Z. Anorg. Chem.* (1961) **310**, 143 - 169.

[2] A.D. Pelton: *Bull. Alloy Phase Diagrams* (1986) **7**, 139 - 142.

[3] A.D. Pelton: *Bull. Alloy Phase Diagrams* (1986) **7**, 228 - 231.

[4] A.D. Pelton: *Bull. Alloy Phase Diagrams* (1986) **7**, 136 - 139.

[5] A.D. Pelton: *Bull. Alloy Phase Diagrams* (1986) **7**, 23 - 25.

[6] A.D. Pelton: *Bull. Alloy Phase Diagrams* (1986) **7**, 19 - 23.

[7] N.D. Spencer *et al.*: *J. Vac. Sci. Technol. A* (1983) **1**, 1554 - 1555.

[8] A. Mowbray and R.G. Jones: *J. Vac. Sci. Technol. A* (1989) **7**, 3373 - 3374.

[9] F.C. Henn, M.E. Bussell and C.T. Campbell: *J. Vac. Sci. Technol. A* (1991) **9**, 10 - 13.

[10] "SAES Getters SpA," Via Gallarata 215, 20151 MILANO Italy.

[11] R.G. Jones: "private communication," Department of Chemistry, university of Nottingham, University Park, Nottingham NG7 2RD UK.

[12] "Philips CFT," *private communication*, Eindhoven, The Netherlands.

[13] K. Douglas Carlson: "The Knudsen Effusion Method," *The Characterization of High-Temperature Vapors*, John Wiley, New York (1967) 115 - 130.

[14] S.A.E. Johansson and T.B. Johansson: *Nucl. Instr. Meth.* (1976) **137**, 473 - 516.

[15] M.W. Chase: *Bull. Alloy Phase Diagrams* (1983) **4**, 124.

[16] R. Haase and H. Schoenert: Pergamon Press, Oxford (1969).

[17] E.A. Guggenheim: *Thermodynamics*, North Holland Physics Publishing, Amsterdam (1959).

[18] A.R. Miedema, P.F. de Chatel and F.R. de Boer: *Physica B* (1980) **100**, 1 - 28.

[19] A.R. Miedema, F.R. de Boer and R. Boom: *Physica B* (1981) **103**, 67 - 81.

[20] F.R. de Boer *et al.*: *Cohesion in Metals*, North Holland Physics Publishing, Amsterdam (1986).

[21] K.L. Komarek: "Experimentelle Methoden zur Thermodynamik der Metalle und Legierungen," *Z. Metallkde.* (1973) **64**, 325 - 341 and 406 - 418.

[22] J.W. Ward: *Proc. 3rd Intern. Symp. High Temp. Technol.*, Asilomar, California (1967) 639 - 646.

[23] K. Motzfeldt: *J. Phys. Chem.* (1955) **59**, 139.

[24] J.W. Ward, R.N.R. Mulford and M. Kahn: "Study of some of the Parameters affecting Knudsen effusion I," *J.Chem.Phys.* (1967) **47**, 1710 - 1717.

[25] J.W. Ward, R.N.R. Mulford and R.L. Bivens: "A Monte Carlo computer analysis of parameters deduced from experiment," *J.Chem.Phys.* (1967) **47**, 1718 - 1723.

[26] J.W. Ward: "The vapor pressure of gold," *J.Chem.Phys.* (1967) **47**, 4030 = 4034.

[27] J.W. Ward and M.V. Fraser: "Monte-Carlo calculations of effusion probabilities and flux gradients for Knudsen cells," *J.Chem.Phys.* (1968) **49**, 3743 - 3750.

[28] J.W. Ward: "Free path considerations in small Knudsen cells," (1968) **49**, 5129 - 5132.

[29] J.W. Ward: "Monte-Carlo analyses of channel orifices," *J.Chem.Phys* (1969) **50**, 1877 - 1882.

[30] C.J. Raub and V.B. Compton: *Z. Anorg. Allg. Chem.* (1964) **332**, 5 - 11.

[31] G.P. Crawford *et al.*: "Characterization of the cylindrical cavities of Anopore and Nuclepore membranes," *J. Chem. Phys.* (1992) **96**, 7788.

[32] H.P.M. Kivits: "Particle Induced X-ray Emission for quantitative trace-element analysis using the Eindhoven cyclotron," *Ph.D. Thesis Eindhoven University of Technology*, Eindhoven, The Netherlands (1980).

[33] N.E. Holden and R.L. Martin: "Atomic weights of the elements 1981," *Pure & Appl. Chem.* (1983) **7**, 1101 - 1118.

SUMMARY

This thesis describes a spectroscopic method to detect, with high sensitivity and extremely high resolving power rubidium isotopes in high pressure krypton gas.The method can be used to investigatethe production process of rubidium radio-isotopes via (p,xn) reactions in a krypton gas target.

Although rubidium-81 is produced routinely by irradiation of a gastarget filled with krypton-81 with 26 MeV protons, little is known about the details of the production process. A technique able to supply time- and position dependent information about the density of rubidium isotopes during or shortly after the irradiation is what is called for. Based upon known yield data. a rubidium density of 10^{14} m^{-3} is estimated directly following a short proton pulse. After the pulse the density will decay exponentially due to chemical reactions between rubidium and residual impurities in the krypton gas. In order to detect these very low densities spectroscopically, use is made of the very strond D-resonance lines of the rubidium atom. Laser induced fluorescence allows the detection of densities substantially lower than 10^{14} m^{-3}, but in high pressure krypton gas isotope selectivity is lost. Isotope selectivity can be retained by combining the strong optical transition with the weak microwave transition between the hyperfine splitted groundstates. These microwave transitions, in contrast to the optical transitions, are hardly affected by pressure broadening. This double resonance method has been shown to be capable of detecting densities on the order of 10^{14} m^{-3} with a resolution of about 50 kHz, more than enough to allow for separate detection of isotopes. Batch experiments in high pressure krypton gas were shown to be unable to simulate the production environment of rubidium isotopes due to excessive chemical decay of rubidium.

Verification of the densities as produced by double resonance detection is of paramount importance both because absolute measurements remain diffucult to carry out and because rubidium densities are not accurately known. In order to allow for absolute measurements, a lot of attention has been paid to a self-calibrating technique. Absorption and fluorescence are to compete in such a way that a maximum is produced in the measured fluorescence as a function of density. This maximum can then be shown to be related to a uniquely determined density, independent of difficult to determine apparatus constants. This technique was applied to naturally abundant rubidium in an evacuated glass cell, where the density can be controlled by setting the temperature. The resulting absolute densities were checked with a thermodynamic method. This allowed the determination of the heat of formation of rubidium vapour (82.3 ± 0.8) kJ mol^{-1} which is in accordance with literature values.

A rubidium vapour source that is easy to use, accurate and

reproducible could be used to check optical density measurements. An effort to develop such a source based upon the gold(5) - rubidium intermetallic compound was undertaken. The rubidium partial vapour pressure of this compound was determined as a function of temperature by Knudsen evaporation. The evaporated rubidium was collected on a substrate and this was subsequently analyzed by PIXE. Using the rubidium effusate masses, as determined with PIXE, allowed a determination of the vapour pressure. The resulting vapour pressures were many orders of magnitude lower than one would calculate from gross thermodynamic calculations. Although the gold(5) - rubidium compound appears to be a reproducible source of rubidium vopour, further research is needed in order to explain the large difference between experiment and theory.

SAMENVATTING

Dit proefschrift beschrijft een spectroscopische methode om met grote gevoeligheid en extreem hoog oplossend vermogen rubidium-isotopen te detecteren in hoge-druk-krypton-gas. De methode kan worden ingezet bij het onderzoek van het produktieproces van rubidium radio-isotopen via (p,xn) reacties met krypton.

Alhoewel de produktie van rubidium-81 als routine wordt uitgevoerd door bestraling van een met krypton-81 gevuld gastarget met 26 MeV protonen, is er weinig bekend over de details van het produktieproces. Een methode die tijd- en plaatsafhankelijke informatie kan leveren over de dichtheid van rubidium, tijdens of kort na de bestraling, zou uitkomst kunnen bieden. Op basis van bekende opbrengstgegevens van rubidium-isotopen kan geschat worden dat de rubidiumdichtheid direct na een korte protonen-puls ongeveer 10^{14} m^{-3} zal bedragen. Na de puls zal de dichtheid exponentieel met de tijd afnemen ten gevolge van chemische reacties tussen rubidium en onzuiverheden in het krypton-gas.
Om deze lage dichtheden spectroscopisch te kunnen detecteren wordt gebruik gemaakt van de sterke D-resonantielijnen van het rubidium-atoom. Met behulp van laser geïnduceerde fluorescentie is het mogelijk dichtheden van 10^{14} m^{-3} en lager te meten, maar in hogedruk-kryptongas gaat de isotoopselectiviteit daarbij verloren. Isotoop-selectiviteit kan men behouden door de sterke optische overgang te combineren met de zwakke microgolf-overgang tussen de hyperfijn gesplitste grondtoestanden. Deze micogolf-overgangen vertonen, in tegenstelling tot de optische overgangen, nauwelijks drukverbreding. De aldus verkregen dubbel-resonantiemethode is in staat gebleken dichtheden van 10^{14} m^{-3} te meten met een resolutie van ca. 50 kHz, ruim voldoende om isotopen selectief waar te nemen. Bulk-experimenten in hogedruk-kryptongas bleken echter niet geschikt om de produktie-omstandigheden na te bootsen omdat het chemisch verval van rubidium te zeer overheerst.

Verificatie van de met dubbelresonantie gemeten dichtheden is van groot belang; enerzijds omdat absolute metingen niet goed mogelijk zijn, anderzijds omdat de rubidiumdichtheid in een gastarget niet nauwkeurig bekend is.
Om absolute metingen mogelijk te maken is veel aandacht besteed aan een zelfcalibrerende methode. Hierbij werken absorptie en fluorescentie elkaar in die zin tegen dat een maximum ontstaat in de gemeten fluorescentie als functie van de dichtheid. Dit maximum ligt bij een uniek bepaalde waarde van de dichtheid en deze waarde van de dichtheid is onafhankelijk van moeilijk te bepalen apparaatconstanten. Deze methode is toegepast op natuurlijk rubidium in een geëvacueerde glazen cel waarin de dichtheid door middel van de temperatuur kan worden geregeld. De resulterende, absolute dichtheden zijn met een

thermodynamische methode op hun consistentie onderzocht. De daarbij gevonden waarde van de vormingswarmte van rubidiumdamp, (82.3 ± 0.8) kJ mol^{-1}, stemt goed overeen met literatuurgegevens.

Om over een bron van rubidium-damp te kunnen beschikken die nauwkeurig is en reproduceerbaar werkt, is een poging gedaan een dergelijke bron te ontwikkelen op basis van de Au_5Rb intermetallische verbinding. Van deze verbinding is de rubidium-partieeldruk bepaald als functie van de temperatuur met behulp van een Knudsen-effusie-methode. Het evaporerende rubidium werd hierbij opgevangen met een drager en deze werd vervolgens met behulp van PIXE geanalyseerd. Uit de met PIXE bepaalde rubidium-effusaatmassa kan vervolgens de dampdruk worden afgeleid. Het blijkt dat de gevonden waarden vele orden lager zijn dan men op grond van thermodynamische beschouwingen zou verwachten. Hoewel de Au_5Rb bron reproduceerbaar blijkt te werken, is nog veel onderzoek nodig om het geconstateerde verschil tussen theorie en experiment te verklaren.

DANKBETUIGING

Zeer veel mensen hebben mij geholpen tijdens de voorbereiding van dit proefschrift. Allen wil ik op deze plaats voor hun hulp van harte bedanken.

Een aantal mensen verdient het echter met name genoemd te worden voor hun bijzondere bijdrage aan het tot stand komen van dit proefschrift.

A.H. Kemper;	voor zijn niet aflatende hulp bij allerhande experimentele problemen.
H. Heller;	voor zijn hulp bij het ontwerp en de bouw van het vacuumsysteem.
M.H.M. Knoben;	voor zijn suggestie om een microgolf transmissielijn te gebruiken en voor de metingen daaraan.
P.H.A. Mutsaers;	voor zijn hulp bij het opzetten en uitvoeren van de PIXE metingen.
A.G.M. Janssen;	voor zijn bijdragen op het gebied van de isotopen productie.
M.C.K. Gruyters;	voor het verzorgen van de vele figuren.
J. Damsma;	voor het vele typewerk aan een eerste versie van dit proefschrift.

LEVENSLOOP

6 april 1961	Geboren te Apeldoorn
29 mei 1979	Diploma Atheneum
	St.-Jan's college te Hoensbroek
10 september 1986	Diploma Technische Natuurkunde
	Technische Hogeschool Eindhoven
27 augustus 1986	Wetenschappelijk assistent
	Vakgroep Deeltjesfysica,
	Faculteit Technische Natuurkunde
	Technische Universiteit Eindhoven
1 september 1991	Associate Research Physicist
	Shell Research, Rijswijk (KSEPL)

STELLINGEN

behorende bij het proefschrift

Isotopically selective detection of rubidium in krypton

Alexander Michaël van der Spek

Eindhoven, 8 december 1992

I

De opvatting van Ward [1] en van Ward, Mulford en Kahn [2], dat de dampdruk bepaald met behulp van Knudsen-effusie-experimenten geen precies definieerbare grootheid is, omdat de door oppervlakte-spannings-effecten bepaalde geometrie van het materiaal een rol speelt, is onjuist. De invloed van oppervlakte-spanning op de dampdruk van een materiaal is immers goed te beschrijven in een thermodynamisch kader.

II

Het feit dat de ICSU/CODATA Task Group on Key Values for Thermodynamics [3] twintig jaar nodig gehad heeft voordat een eindrapport kon worden uitgebracht, toont aan dat in het aangehaalde werk vaak resultaten zijn opgenomen die, bij gebrek aan een uniforme presentatie wijze, niet zonder meer konden worden overgenomen.

III

Interferometrische weglengtemeting met behulp van een diodelaser maakt in-situ correctie voor de langzaam variërende brekingsindex van de atmosfeer mogelijk door de temperatuur en de injectiestroom van de diodelaser zo te sturen dat de golflengte ter plekke van de meting gemiddeld constant is. Dit principe, door Höfler, Molnar, Schröder en Kulmus [4] in praktijk gebracht, betekent dat meetnauwkeurigheden die voorheen enkel in laboratorium-omstandigheden gerealiseerd konden worden ook in de industriële praktijk realiseerbaar zijn.

IV

De golflengte van een helium-neon-laser, waarvan de frequentie gestabiliseerd is met een jodium-cel, hangt mede af van de vervuilingsgraad van die cel. Deze vervuilingsgraad is op zeer eenvoudige wijze te meten. Een Stern-Volmer experiment blijkt een uitstekend middel om de vervuilingsgraad van jodium-cellen te kwantificeren [5]. Het is daarom zeer aan te bevelen om deze jodium-cellen jaarlijks op deze wijze op de aanwezigheid van eventuele verontreinigingen te controleren.

V

Een resonantielamp zoals ontwikkeld door Bell, Bloom en Lynch [6] is in sommige gevallen als lichtbron in fluorescentiemetingen te verkiezen boven een laser.

VI

Door Yang en Lee [7] [8] is aangetoond dat er een mathematische equivalentie bestaat tussen een Ising-model in een magnetisch veld en een roostergas. Dit suggereert dat ook voor een Ising-model in een magnetisch veld een overgangswarmte bestaat die ingevolge de derde hoofdwet van de thermodynamica niet zal afhangen van de temperatuur.

VII

De formules voor de berekening van de absolute entropie en de vrije energie van een ideaal mono-atomair-gas zoals opgenomen in de JANAF tabellen [9] zijn dimensioneel en numeriek niet correct. Evenmin zijn ze in overeenstemming met de, recentere, aanbevelingen van de IUPAP [10] betreffende de notatie en de numerieke waarde van de Sackur-Tetrode absolute-entropie-constante.

VIII

De dagelijkse KNMI voorspelling van temperatuur, luchtdruk, windsnelheid en windrichting is in het algemeen zeer goed te noemen, als we rekening houden met de verdeling van het aantal meetstations over de aarde. Het ontstaan van bewolking of het optreden van neerslag is echter vele malen moeilijker te voorspellen [11]. Bewolking en neerslag bepalen echter in zo sterke mate de perceptie van 'het weer' dat de voorspellingen van het KNMI, ten onrechte, als notoir onbetrouwbaar te boek staan.

IX

Voor het genereren van toevalsgetallen bestaan anno 1992 algoritmen die theoretisch goed gefundeerd zijn, die een hele reeks statistische toetsen met succes doorstaan en die ook in de zin van de spectrale test als voldoende te kwalificeren zijn [12]. Desondanks blijft het gebruik van oude algoritmen waarvan de resultaten aantoonbaar slecht zijn, een zekere populariteit genieten. Dat dit conservatisme nog niet heeft geleid tot ongelukken is vermoedelijk meer te wijten aan het toeval dan aan de algemeen veronderstelde ongevoeligheid van fysische problemen voor de statistische eigenschappen van simulaties.

REFERENCES

[1] J.W. Ward: "Study of some of the parameters affecting Knudsen effusion. III The vapor pressure of gold," *J.Chem.Phys.* (1967) **47**, 4030 - 4034.

[2] J.W. Ward, R.N.R. Mulford and M. Kahn: "Study of some of the parameters affecting Knudsen effusion. I. Experimental tests of the validity of the cosine law as a function of cell and sample geometrics and materials," *J. Chem. Phys.* (1967) **47**, 1710 - 1717.

[3] J.D. Cox, D.D. Wagman and V.A. Medvedev: *CODATA key values for thermodynamics*, Hemisphere Publishing Corporation, New York (1989).

[4] H. Höfler, J. Molnar, Cl. Schröder and K. Kulmus: "Interferometrische Wegmessung mit automatischer Brechzahlkompensation," *Technisches Messen* (1990) **57**, 346 - 350.

[5] S. Fredin - Picard: "A study of contamination in $^{127}I_2$ cells using laser induced fluorescence," *Metrologia* (1989) **26**, 235 - 244.

[6] W.E. Bell, A.L. Bloom and J. Lynch: "Alkali metal vapor spectral lamps," *Rev. Sci. Instrum.* (1961) **32**, 688 - 692.

[7] C.N. Yang and T.D. Lee: "Statistical theory of equations of state and phase transitions. I. Theory of Condensation," *Phys. Rev.* (1952) **87**, 404 - 409.

[8] C.N. Yang and T.D. Lee: "Statistical theory of equations of state and phase transitions. II. Lattice gas and Ising model," *Phys. Rev.* (1952) **87**, 410 - 419.

[9] M.W. Chase *et al.*: "JANAF Thermochemical tables," *J. Phys. Chem. Ref. Data*, third(ed.) (1985) **14 (Suppl. 1)**, 1 - 1856.

[10] E.R. Cohen and P. Giacomo: "Symbols, units, nomenclature and fundamental constants in physics," *Physica A* (1987) **146**, 1 - 68.

[11] C. Lemcke and S. Kruizinga: "Model output statistics forecasts: Three years of operational experience in the Netherlands," *Monthly Weather Review* (1988) **117**, 1077 - 1090.

[12] P. L'Ecuyer: "Efficient and portable combined random number generators," *Comm. ACM* (1988) **31**, 742 - 749.